POLITECNICO DI MILANO

Facoltà di Ingegneria Industriale

Corso di Laurea Magistrale in
Ingegneria Energetica

EXPERIMENTAL STUDIES AND MODELING OF A HIGH PRESSURE SPRAY SYSTEM FOR AEROSOL DECONTAMINATION

Relatore: Prof. Ing. Lucio Tiziano Araneo
Correlatore: Dott.ssa Ada Barbara Del Corno

Tesi di Laurea di:
Stefano Barbano, matricola 823530

Anno Accademico 2015 – 2016

Table of contenents

Acknowledgments

E’ mio particolare desiderio ringraziare la mia tutor aziendale la Dott.ssa Ada Del Corno per tutto il supporto, la cura e la dedizione dedicatami giornalmente in tutti questi mesi di lavoro.

Ringrazio tutto il personale di RSE con cui ho avuto a che fare in paricolar modo l’Ing. Flavio Parozzi, l’Ing. Andrea Cavallari e il mio vicino di scrivania Ing. Valter Prandoni.

Ringrazio il mio relatore, l’Ing. Lucio Tiziano Araneo per la disponibilità, la rapidità per tutti gli utili consigli e l’esperienza che è riuscito a trasmettermi.

Ringrazio il mio amico e compagno di avventura Marco Turni per tutto il tempo trascorso insieme in RSE e per il sostegno reciproco anche nei momenti che sembravano difficili.

Ringrazio infine tutta la mia famiglia e la mia compagna Sara per tutto il supporto e la sopportazione avuta nei miei confronti durante questo lungo percorso di studi.

Abstract

In case of severe accident in nuclear power plants, fission products could be released under the form of aerosol particulate. The current sprays used as safety systems in Light Water Reactor (LWR) were mainly dimensioned to suppress steam pressurization during design basis loss-of-coolant accidents, to remove molecular iodine from the containment atmosphere and to enhance the gas mixing in case of the presence of hydrogen.

The European PASSAM project is aimed to study the performances of current mitigation systems and to evaluate the possibility of other innovative systems to be implemented in the current and future nuclear power plants.

This work developed at RSE spa has the aim to put in evidence the decontamination performances of the high pressure sprays and to develop a simplified model to predict their aerosol removal rate.

The whole activity has been developed in three parts. The first two are of experimental nature and are aimed to obtain data of both the decontamination performances and characteristics of the high pressure water spray. The last part is to condense theoretical knowledge and experimental data to develop a model that may provide good approximations of the spray behaviour.

Keywords: Spray, Droplet, Particle, Decontamination, Agglomeration

Sommario

In caso di grave incidente nelle centrali nucleari, i prodotti di fissione possono essere rilasciati sotto forma di aerosol. Gli spray attualmente utilizzati come sistemi di sicurezza nelle centrali as acqua leggera (LWR) sono stati principalmente dimensionati per sopprimere la pressurizzazione del vapore durante incidenti base dovuti alla perdita di refrigerante, per rimuovere lo iodio molecolare dall'atmosfera di contenimento e per migliorare la miscelazione dei gas in caso di presenza di idrogeno.

Il progetto europeo PASSAM si propone di studiare le prestazioni degli attuali sistemi di mitigazione e di valutare la possibilità di valutare altri sistemi innovativi da poter usare nelle attuali e future centrali nucleari.

Questo lavoro sviluppato presso RSE spa ha lo scopo di mettere in evidenza le prestazioni di decontaminazione degli spray ad alta pressione e di sviluppare un modello semplificato per prevederne il tasso di rimozione di aerosol.

Tutta l'attività è stata sviluppata in tre parti. Le prime due sono di natura sperimentale e hanno lo scopo di ottenere i dati rigurdanti sia le prestazioni di decontaminazione che le caratteristiche degli spray ad alta pressione. L'ultima parte è quella di condensare le conoscenze teoriche e i dati sperimentali per sviluppare il modello di previsione.

Parole chiave: Spray, Goccia, Particolato, Decontaminazione, Agglomerazione

Extended abstract

Introduction

In case of severe accident in nuclear power plants, fission products can be released under the form of aerosol particulate. The European PASSAM project is aimed to study the performances of current mitigation systems and to evaluate the possibility of other innovative systems to be implemented in the current and future nuclear power plants.
High pressure water spray systems are one of the innovative technologies considered. The aim of this work is to put in evidence their decontamination performances and to develop a model that can predict their aerosol removal rate.

Experimental activity

This work is composed of two different experimental activities. The first one has the aim of evaluate the decontamination performances of the high pressure water spray systems. The second one is a characterization of the spray structure with a non-invasive optical method.
The first activity consisted in monitoring, over time, the aerosol concentration while the spray is operating. It has been performed with an aerosol composed of monodisperse SiO_2 particles with size of 0.5 µm, 1[1] µm and 2µm. For each particle size, tests with different water injection pressures (50, 100 and 130 bar) and different initial particle concentrations (2, 10 and 30 mg/m^3) have been performed.
The spray decontamination process follows a negative exponential trend. If the normalized concentration is considered, every single test is described with a single parameter λ called decontamination coefficient. An increasing value of λ describes a faster process.

$$\frac{C(t)}{C(0)} = e^{-\lambda t}$$

Tests showed that λ is not influenced by the initial particle concentration, as reported in Figure A. Figure B shows that a faster cleaning of the containment atmosphere is obtained with increasing water injection pressure while the decontamination process became slower with decreasing aerosol dimensions as showed in Figure C. This occurs because an increase in the water pressure provides a higher flow rate and droplets of smaller size with increasing velocities. On the other hand, a decrease in the aerosol particle dimension leads to a lower inertia which implies that the particles are more susceptible to the droplets boundary layer and are more likely to be moved apart than to be intercepted by the water droplets.

[1] Measurements with particles of 1 µm were performed in a previous work (Casella 2014)

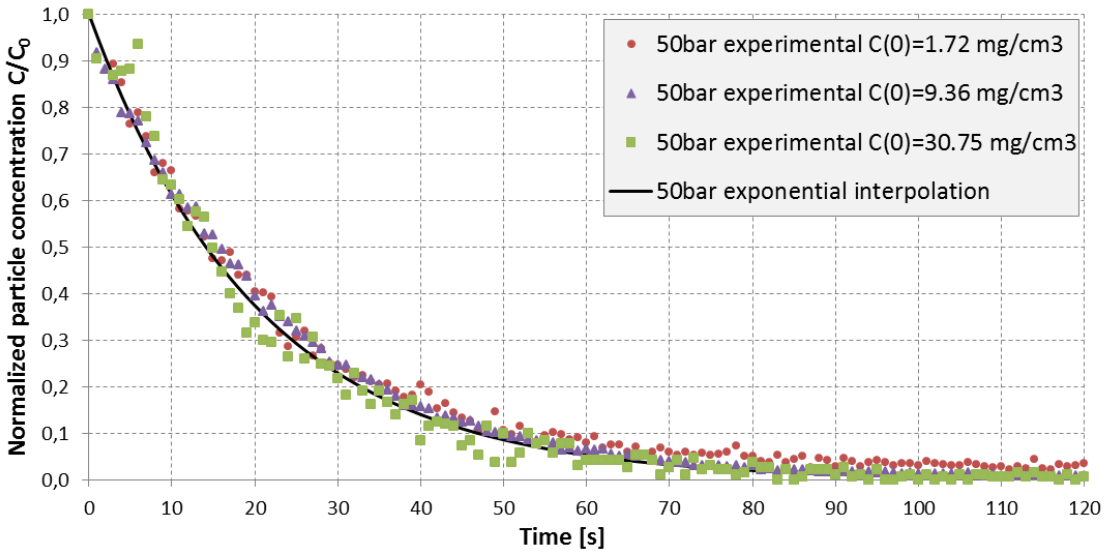

Figure A: influence of the initial particle concentration in the case of a pressure of 50 bar and particle size of 0.5 µm

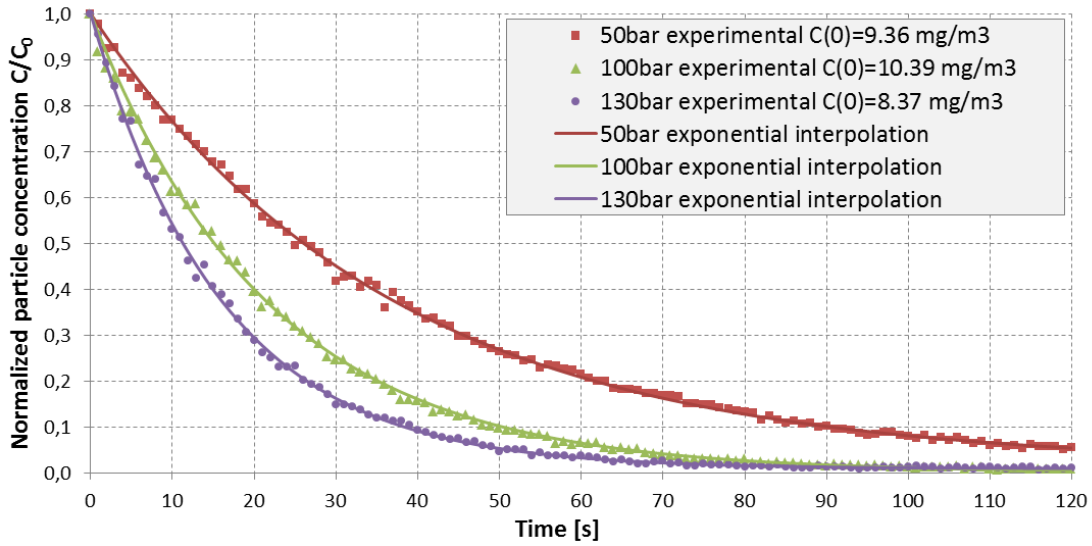

Figure B: decontamination curves with increasing water pressure with 0.5 µm aerosol particle size

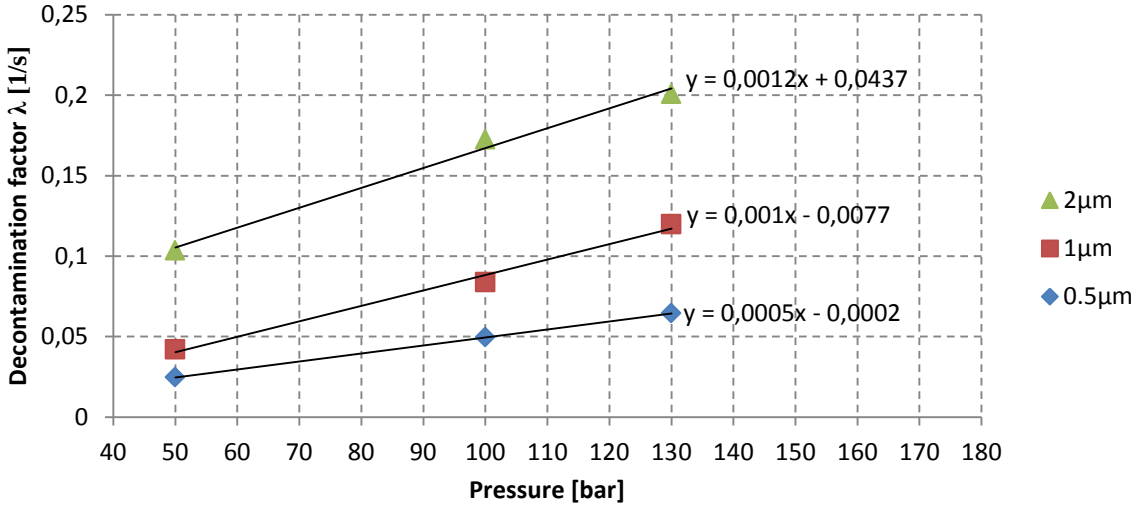

Figure C: decontamination coefficient as function of water injection pressure and aerosol particle size

The second experimental activity has the aim to obtain the size distribution and velocity of the droplets to be used in the model and to validate its output.

To achieve that it is used a non-invasive measurement technique called Phase Doppler Anemometry (PDA) that uses the properties of coherence and polarisation of two crossing laser beams to measure the velocity and the size of the water droplet passing through it.

Measurements are carried out with the spray axis oriented vertically downwards, along 5 cross patterns traversing diametrically the spray, located perpendicular to the spray axis at the axial distance of 50, 100, 250, 500 and 750 millimetres respectively from the injection nozzle. The water pressures used are 50, 80, 100 and 130 bar.

The data collected by the PDA, that refers to single points, are used to calculate the droplet size distribution and velocity of each spray cross-section at each considered axial distance.

Figure D shows the droplet size distribution, obtained from the post processing work, at a distance of 50 millimeters from the nozzle. Figure E shows the velocity obtained for each droplet size class at the same height.

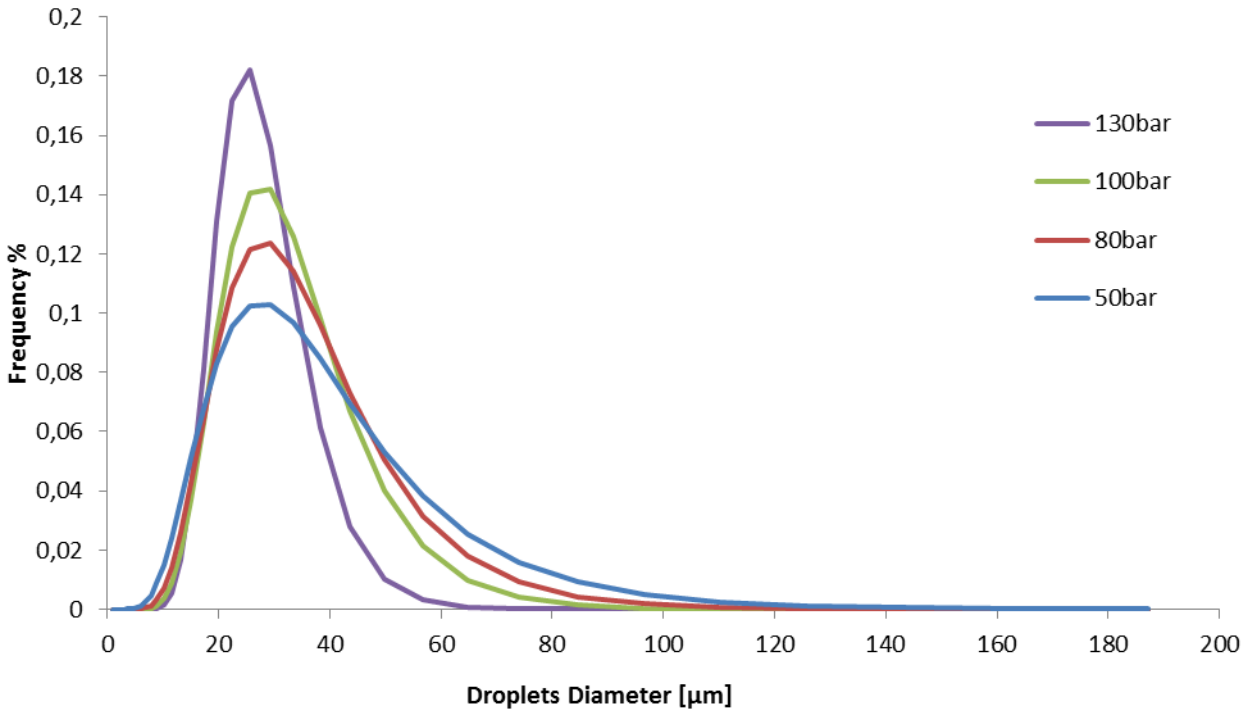

Figure D: droplets spray distribution at 50 mm from the nozzle

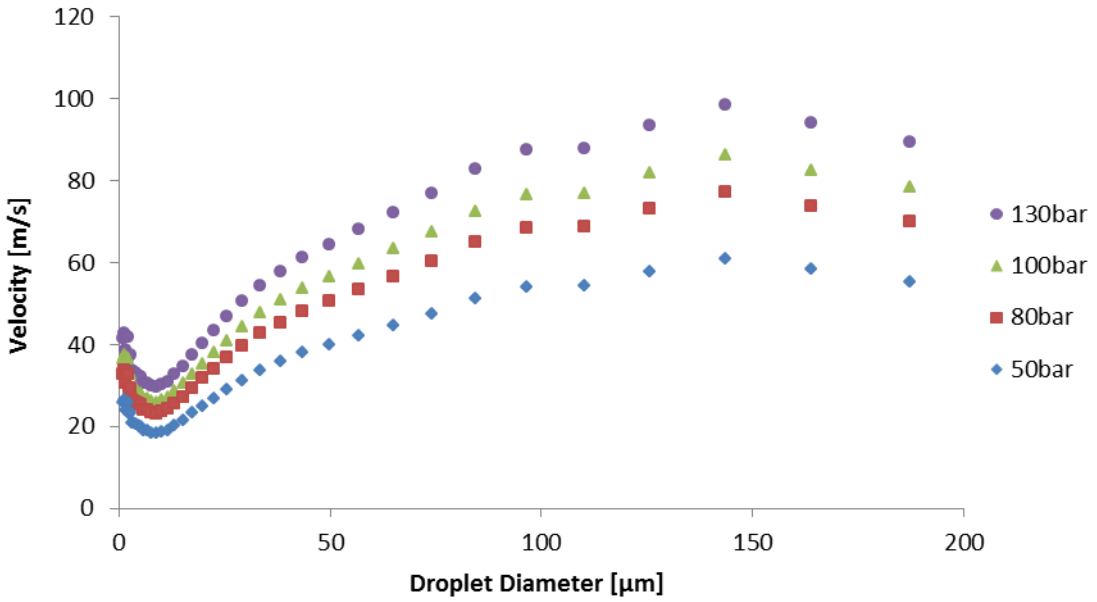

Figure E: velocity of each droplet size class at 50 mm from the nozzle

Modeling activity

The model is based on an Eulerian point of view of the process. The fluidodynamic behaviour of the spray is firstly took into account with an analysis of the air-droplet and droplet-droplet interaction, then the interaction between droplet-particulate will determinate the evolution of the capture process.

The main hypotheses behind this work are:

- Monodirectionality of the spray, the physical properties of the droplets evolve along its axis while being uniformly distributed among the radial coordinate (because in high pressure sprays the cone angle is very narrow and the axial component of the velocity is predominant to the radial one);
- Particulate matters is uniformly distributed in the chamber;
- No evaporation (the air of the chamber become saturated in a few seconds after the spray activation);
- Only gravitational and diffusive mechanism are taken into account for particle agglomeration since phoretic effects are negligible in our configuration (air is atambient temperature and no steam that condenses on the droplet surface);
- No breakup;
- Negligible particulate capture outside the spray;

The parameters that can be modified are:

- Water pressure;
- Nozzle volumetric factor;
- Initial droplets velocity and size distribution;
- Spray cone angle;

- Spray height;
- Air velocity outside the spray;
- Dimension, density and initial concentration of the monodispersed particulate;
- Chamber volume;
- Time and space discretization step;

The model will calculate, for each spatial step, the evolution of the spray characteristics and use them to calculate the efficiency of the decontamination process considering the particulate concentration at the end of each time interval.

Figure F,Figure G andFigure H show the main results of the fluid dynamic of the spray.

The decontamination coefficients provided by the model, summarized in Figure I, show good agreement with the experimental data.

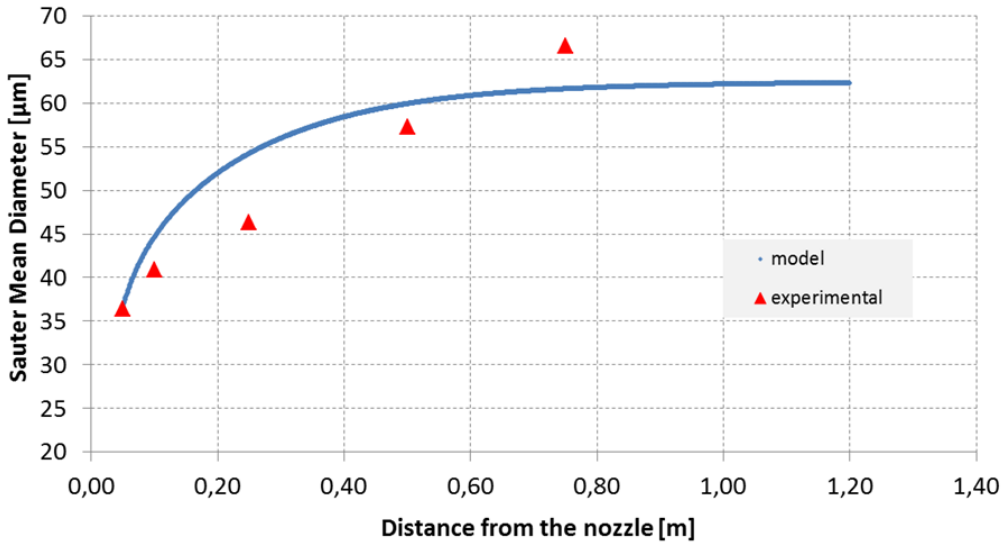

Figure F: spray Sauter mean diameter evolution in the case of a pressure of 100 bar, experimental and model results

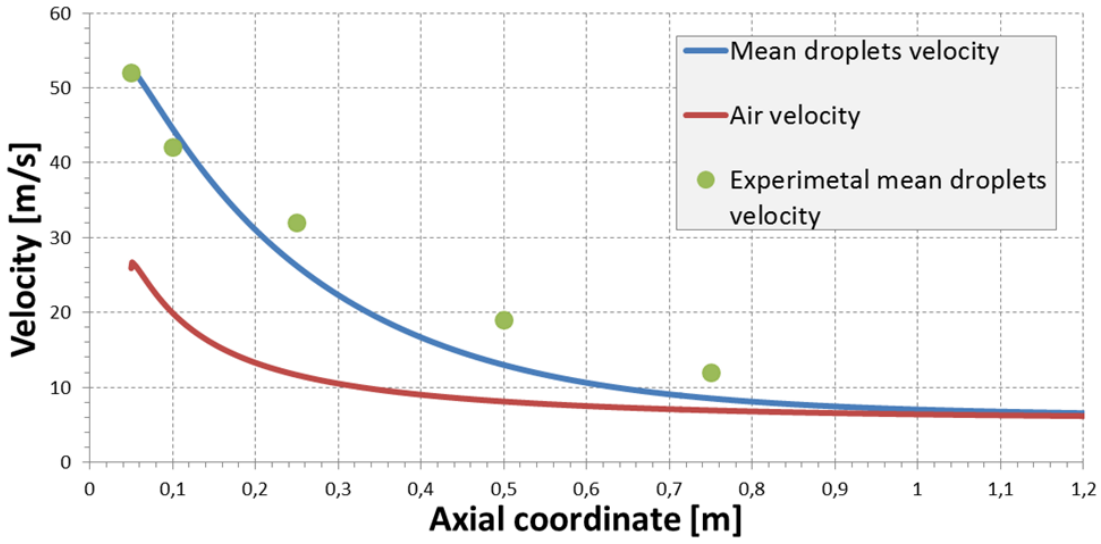

Figure G: evolution of droplets and air mean velocity in the case of a pressure of 100 bar, experimental and model results

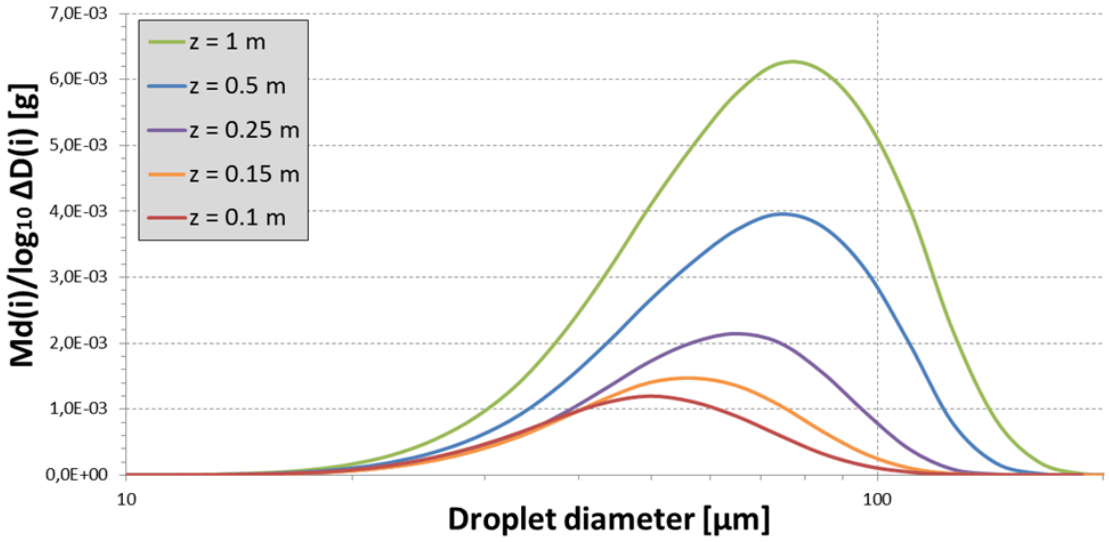

Figure H: droplet mass size distribution at various heights in the case of a pressure of 100 bar, model results

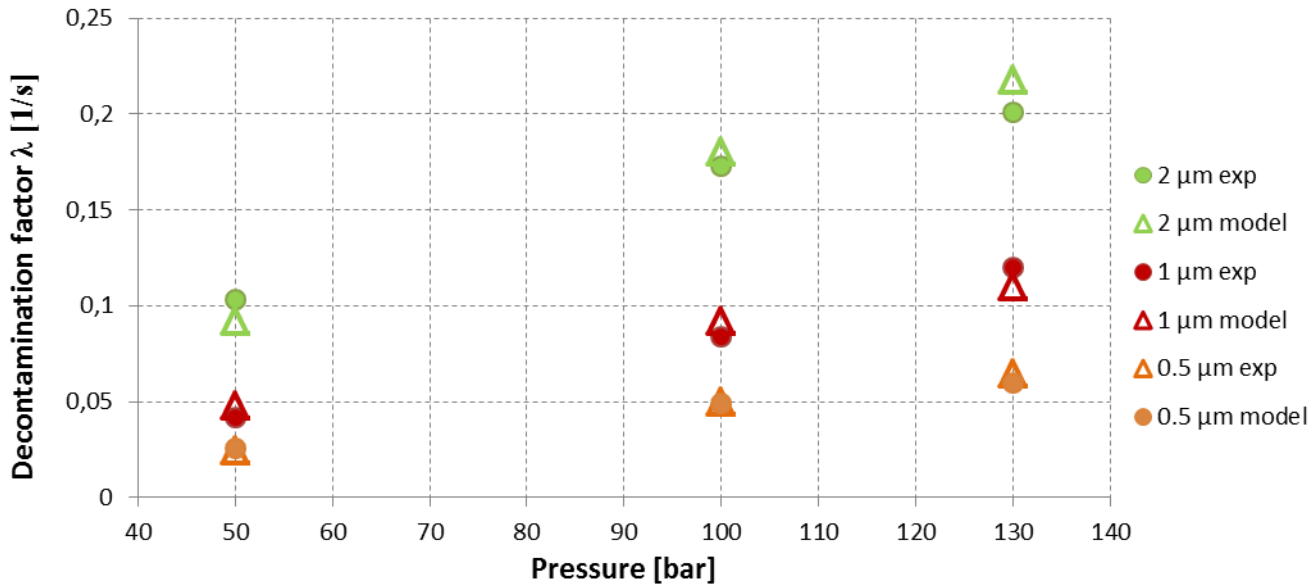

Figure I: decontamination coefficient as function of water pressure and aerosol particle size, experimental and model results

List of figures

List of tables

The PASSAM project

Current Nuclear Power Plants (NPP) are furnished with safeguards based on the Design Basis Accident and some extensions to cope with accidents beyond the design bases.

After the accident at the Fukushima Daiichi nuclear plant, in Europe grew the need to further verify the behavior of the mitigation systems and, above all, to ensure the installation of systems that reduce as much as possible the potential releases in case of severe accident.

In this context the "Passive and Active Systems on Severe Accident source term Mitigation" (PASSAM) project was born in the frame of the 7th framework program of the European Commission and it is mainly of experimental nature (Albiol et al., 2012; Albiol et al., 2013), involving nine partners (six research organizations, two utilities and one university), all with an historical experience on severe accidents bringing together their competencies and their various test facilities:

- Institut de Radioprotection et de Sûreté Nucléaire (IRSN), France;
- Centro de Investigaciones Energeticas Medio Ambientales y Tecnologicas (CIEMAT), Spain;
- Agencia Estatal Consejo Superior de Investigaciones Cientificas (CSIC), Spain;
- Electricité de France (EDF), France;
- Paul Scherrer Institut (PSI), Switzerland;
- Ricerca sul Sistema Energetico - RSE SpA (RSE), Italy;
- Technical Research Centre of Finland (VTT), Finland;
- AREVA NP GmbH (AREVA), Germany;
- University of Lorraine (UniLor), France

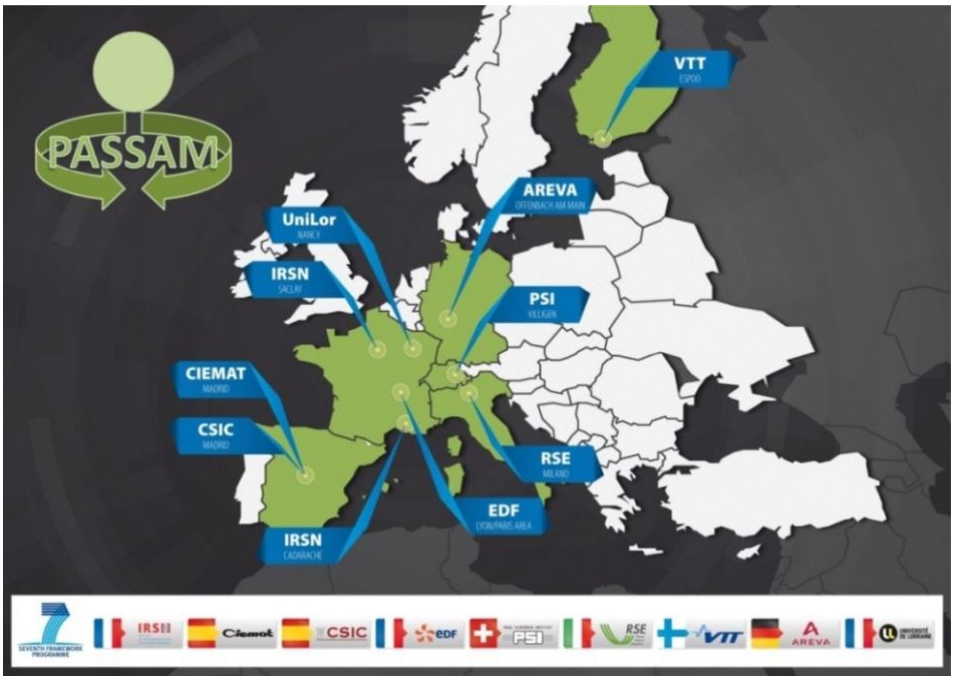

The project have four year duration (2013-2016), is coordinated by IRSN and have a total budget of 5.11 million euros with large amount of work to be performed (395 person.month).

The PASSAM project is of Research and Development nature, aiming at exploring potential enhancement of existing source term mitigation devices and demonstrating the ability of innovative systems to achieve larger source term attenuation. Its outcome will constitute a valuable database which may be strategic for helping the utilities on the decision of implementing and or enhancing mitigation systems on their reactors and for improving severe accident management. The understanding gained from the in-depth analysis of experimental results will make possible to produce simple models and correlations easy to be implemented in accident analysis codes. The use of these codes will allow enhancing the capability of modeling Severe Accident Management scenarios and developing improved guidelines.

To understand the reasons of this project we can observe that in case of a severe accident in a nuclear power plant, among the problems to face, the most critical is to avoid, or strongly limit, the release of fission products in the environment, due to their high radio-toxicity, that can corrupt the aquifers or be dispersed in the air under the form of suspended aerosol.

The PASSAM project is organized into 5 Work Packages (WP), each one on different severe accident aspect

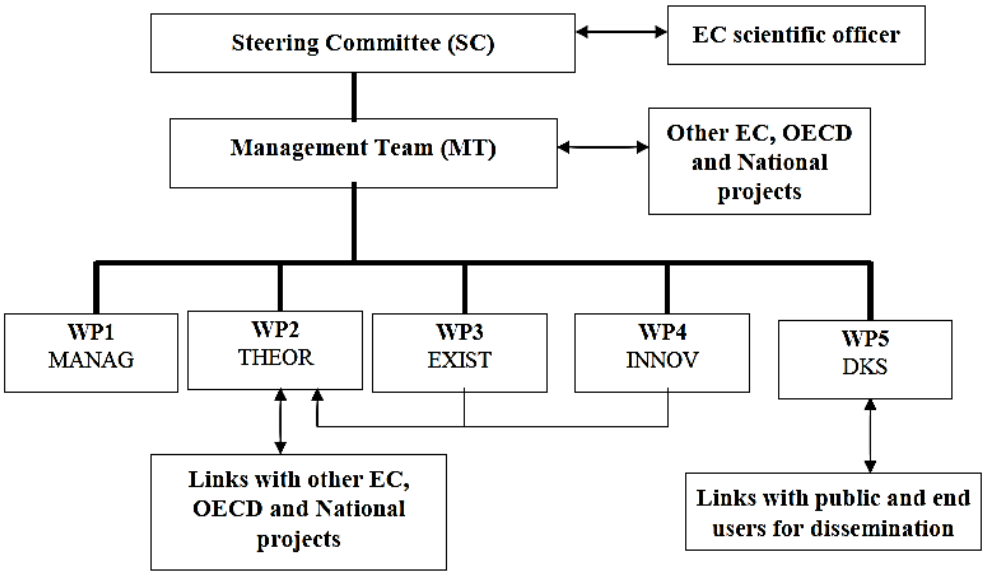

The WP1 (MANAG) regards the project management and IRSN is the leader. In particular, it is responsible of the administrative, financial and quality management aspects and it represents an intermediary with the European Commission and with the necessary decision-making bodies (Steering Committee and Management Team).

The WP2 (THEOR), with leader CIEMAT and participants all PASSAM partners, is divided into two sub work packages: the WP2.1 (SOAR) regarding the state-of-the-art with leader CIEMAT and the WP2.2 (MODEL) regarding the development of simplified models/correlations with leader RSE.

The WP2.1 has the aim to collect in an unique report the current knowledge on the filtration systems used and potentially usable for source term mitigation of severe accidents. In particular, for each type of filtration system the following data are reported: the fluids with which they have been tested, the conditions under which the tests have been carried out, their observed filtration

efficiencies, the understanding of the trapping phenomena, the models and/or the correlations to pre-estimate their filtration efficiencies and, finally, the long term behavior following an accident of the trapped fission products, i.e. if these last remain in the filtration system or there is the possibility that they will be released due to physical and/or chemical phenomena.

In the WP2.2 all partners share and analyze the experimental results produced in the WP3 and WP4, in order to derive simplified models and/or correlations for each type of studied system.

The WP3 (EXIST) regards the experiments on the existing filtration systems and the type of experiments are suggested by the lacks identified in the state-of-the-art report. The leader of this WP is PSI and the participants are IRSN, CIEMAT, PSI, RSE and AREVA NP GmbH. This WP is divided into two sub work packages: the WP3.1 (POOL) on the experimental studies of the pool scrubbing systems with leader PSI and the WP3.2 (SAND) on the experimental studies of the sand bed plus metallic pre-filters with leader IRSN.

The WP3.1 has its starting point in the pool scrubbing efficiency tests performed in the eighties and nineties, with different experimental systems and different aerosol. The available experimental data don't allow a systematic validation of the produced models under accident relevant conditions (temperature, pressure, humidity, gas flow rates, etc.), thus the experimental studies carried out in this WP try to bridge these lacks.

The WP3.2 purpose is an improvement of the experimental studies performed in the late eighties and in the early nineties to test the sand bed filters plus metallic pre-filters that were installed on all French PWRs in operation. Indeed, these mitigation systems need to further tests with molecular iodine and organic iodides confirmed by the state-of-the-art report.

The WP4 (INNOV) concerns experiments on innovative filtration systems. The leader of this WP is VTT and the participants are IRSN, CIEMAT, CSIC, RSE, VTT, AREVA NP GmbH and the University of Lorraine. The partners decided to study five new methods and devices, divided into five corresponding sub work packages, that seem promising for the source term mitigation in severe accident conditions: acoustic agglomerator WP4.1, spray agglomerator WP4.2, electric precipitators WP4.3, improved zeolite and combination of wet WP4.4 and dry filtration systems WP4.5.

The WP4.1 (ACOU), with leader CIEMAT, studies deeply the enhancement of the particle agglomeration by sound waves; in particular, exploiting this agglomeration phenomenon, it causes the enlargement of the particles and with a following capture system will be possible to achieve higher filtration efficiency in the range of 0.1 to 0.3 μm, in which the current systems have a minimum of efficiency.

In WP4.2 (SPRAY), with leader RSE, the purpose is to extend the current studies on traditional spray agglomeration systems, well known already, to non-traditional sprays. Through these last it is possible to exploit the agglomeration obtained, achieving similar advantages as in the acoustic agglomerators.

In WP4.3 (ELEC), with leader VTT, the studies on the electrical filtration systems, already used to reduce many industrial emissions, are expanded to test them in various conditions expected in

this nuclear applications and in various simulated positions in the filtration system to maximize the efficiency.

Through the WP4.4 (ZEOL), with leader IRSN, the partners want to try more efficient zeolite filtration systems for iodine species and possibly for other gases like ruthenium tetroxide, with particular attention at the severe accident conditions.

In the WP4.5 (COMB), with leader AREVA, the combination of wet and dry filters, as well as adsorptive one, are studied to understand the feasibility and the potential benefits.

The last WP, WP5, with leader IRSN and participants all PASSAM partners, is dedicated to the dissemination of knowledge and synthesis.

As shown here the role of RSE is to study in deep the particulate removal system provided by pool scrubbing and sprays (the subject of this thesis work).

1 State of the art of water spray systems for aerosol removal in nuclear power plant

In this section an analysis of the theoretical bases of the process involved in the decontamination carried out by spray system is addressed.
The performance of actual system installed in nuclear power plant is then exposed.

1.1 Decontamination process

The formal differential equation that describes decontamination of an atmosphere by spray droplets is (Powers and Burson, 1993):

$$\frac{dM}{dt} = -\lambda M + \frac{dS}{dt} + \frac{dR}{dt} \qquad 1.1$$

where

M = mass of aerosol suspended in the containment atmosphere
$\frac{dS}{dt}$ = rate at which aerosols are injected into the containment atmosphere
$\frac{dR}{dt}$ = rate at which aerosols are removed from the atmosphere by processes other than those brought on by the sprays
λ = constant rate for aerosol removal by sprays

The rate of aerosol removal from the containment atmosphere by sprays is so much greater than the rates of removal by other processes in the steady state situations of interest here that dR/dt can be neglected. Similarly the agglomeration of aerosol particles can be neglected. Removal rates by sprays are so much larger that the rates of agglomeration that the changes in the aerosol size distribution caused by agglomeration can often be neglected in comparison to the apparent changes in the size distribution brought about by spray removal of particles.
Source rates of aerosols into the containment, dS/dt, are strong function of time. They vary, often dramatically, from accident-to-accident and plant-to-plant. For most purposes, the sources of aerosols to the containment atmosphere would be assumed to be small or zero, typical issue of materials that already has been injected into the containment atmosphere.
The time that a spray of some type must operate to achieve a specified decontamination level is determinate by:

$$DF = exp(+\lambda t) \qquad 1.2$$

where

DF= the ration between the aerosol mass initially in the containment atmosphere and the aerosol mass present after spray operation for a time t

DF is usually called “decontamination factor” and λ “decontamination coefficient”
The time of spray operation required to achieve a specified decontamination factor is given by:

$$t = \frac{ln(DF)}{\lambda} \qquad 1.3$$

The constant rate for aerosol removal, λ, is a critical quantity function of the aerosol particle size distribution, of the characteristics of the spray and of the geometry of the containment; the aim of our work is to provide a simplified model of decontamination by sprays that can be used to estimate the particle removal rate without the necessity of using simulation codes with high computational costs.

1.2 Overview on spray phenomena

In this chapter the spray phenomenology is explored, including its formation, evolution in time and space, and the main mechanisms involved in the particle capture process.

1.2.1 Spray formation

Many different processes are involved in the formation of a generic spray (Lefebvre, 1988). For a spray generated by a non-swirled full hole nozzle the main formation mechanism is break-up.
When a liquid flow if forced by a large pressure difference to flow through the small injector holes with high speed, the liquid jet breaks-up in small droplets, forming a cone shaped spray, because of its high velocity, relative to the surrounding air, and of the turbulence in the jet itself and in the air. This process, called *primary break-up*, is then followed by a *secondary break-up* process, when the aerodynamic interactions between the drops and the air produce a continuous division in droplets of smaller and smaller size.

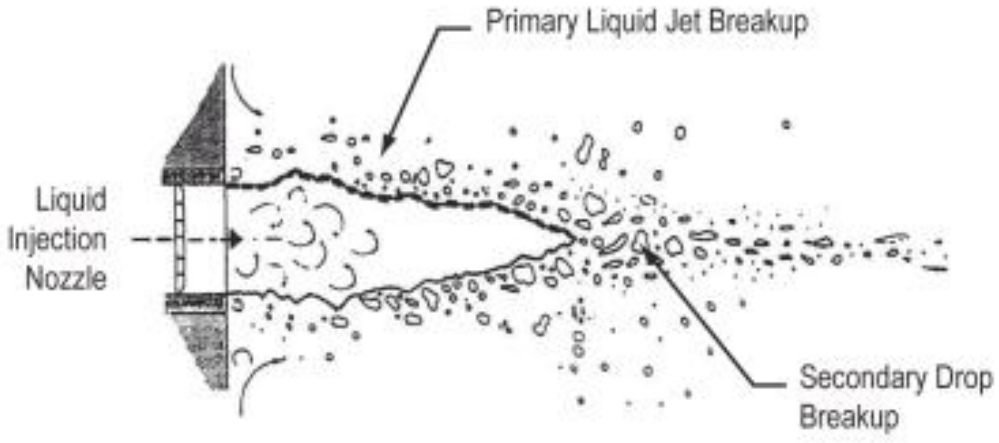

Figure 1: liquid break-up regimes (H.P. Trinh)

The primary break-up takes place close to the nozzle outlet region, prepared by strong turbulent movements inside the nozzle channel often, but not always, producing pressure drops below the vapor tension of the liquid with formation of cavitation bubbles.

At the nozzle outlet, the turbulent movements in the liquid stream and the implosion of the cavitation bubbles generate in the liquid jet unstable surface waves. The interaction between the jet and the air turbulence produces a rapid and selective grow of the surface waves, whose initial characteristics are controlled by what happened inside the nozzle. The surface wave amplification brings the liquid column leaving the nozzle to break-up, at first in ligaments and particles and then in drop cluster and droplets.

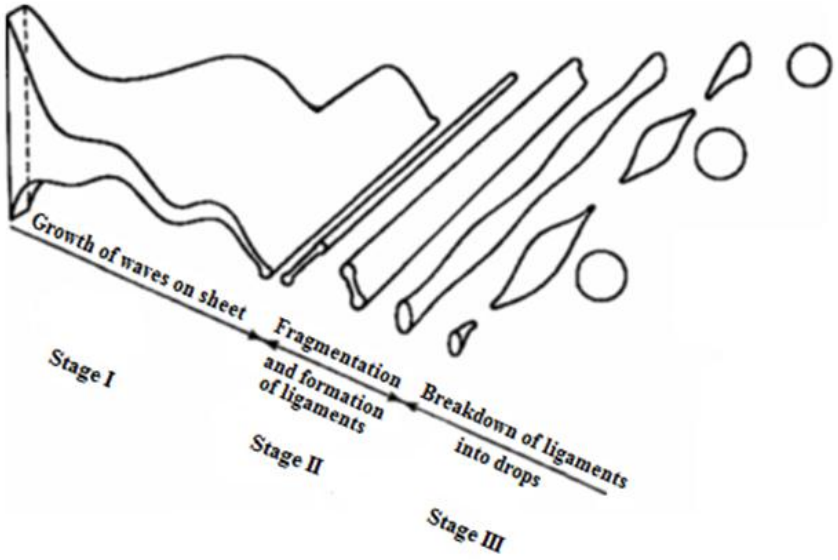

Figure 2: Droplet formation process

Moving away from the nozzle, the air mass entrained within the spray increases and generates turbulent vortexes in which the secondary break-up occur favorite by high values of inertia forces, due to the relative velocity between the air and the single droplet, and contrasted by the liquid surface tension. This dynamic balance of forces is summarized by the Weber number, which compares the relative importance of the previous forces:

$$We = \frac{\rho_l {U_r}^2 D_d}{\sigma_l} \qquad 1.4$$

Where:

- $\rho_l \left[\frac{kg}{m^3}\right]$ is the density of the liquid phase;
- $U_r \left[\frac{m}{s}\right]$ is the relative velocity between the droplet and the air;
- D_d [m] is the droplet diameter;
- $\sigma_l \left[\frac{kg}{s^2}\right]$ is the surface tension of the liquid;

A low Weber number corresponds at higher coalescence force of the liquid surface and a lower propensity to split up in smaller droplets, conversely at high Weber number the inertia forces are dominating and a more intense break-up occur.

The following picture illustrates the correlation between the Weber number and the different kind of break-up mechanism:

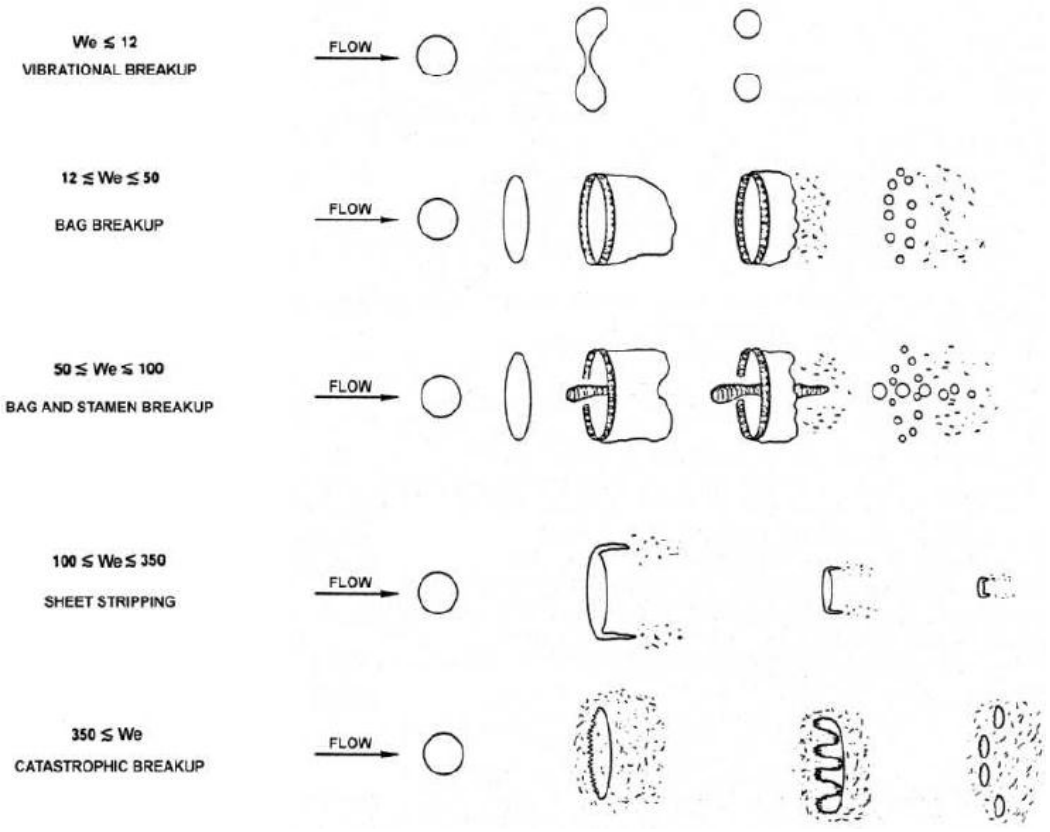

Figure 3: Different break-up mechanism as function of the surface tension (A. Kadocsa, R. Tatschl, G. Kristóf, 2007)

1.2.2 Droplets Size

The droplets generated by the atomizers are not of uniform size. Various distribution functions have been used to fit the experimental data on droplet size distributions, the most used ones are:

- Log-Normal
- Rosin – Rammler
- Nukiyama – Tanasawa

In many mass transfer and flow process it is desirable to work only with average diameters instead of the complete droplet size distribution. The generic mean diameter is defined by:

$$D_{pq} = \left[\frac{\int_0^\infty f(D_d) D_d^p dr}{\int_0^\infty f(D_d) D_d^q dr}\right]^{\frac{1}{p-q}} \qquad 1.5$$

Table 1 shows some of the mean diameters and some field of applications for each. In order to use this means effectively they must be calculated from the drop size distribution equation.

Table 1: Mean Diameters

p	q	p+q (order)	Name and symbol	Field of applications
1	0	1	Number D_{10}	Comparison, Evaporation
2	0	2	Surface area D_{20}	Surface area controlling-e.g, absorption
3	0	3	Volume D_{30}	Volume controlling-e.g., hydrology
3	2	5	Sauter D_{32}	Efficiency studies, mass transfer, reactions

The log-normal distribution is a probability density function that is used in many applications and considers the logarithm of the average value as normally distributed. In this way only positive values are considered. Its expression is:

$$f(D_d) = \frac{1}{\sqrt{2\,\pi\,\sigma^2}}\,\frac{1}{D_d}\,exp\left[-\frac{(ln\,D_d - ln\,\overline{D}_d)^2}{2\,\sigma^2}\right] \qquad 1.6$$

It provides the number of the droplets with a given diameter D_d, where $\overline{D}_d$ is the geometric mean diameter (because in the linear scale the mean value of the distribution turns out to be a geometric mean) and σ^2 is the variance of the log-normal distribution.

Although the real standard deviation is σ, the value $\sigma_g = e^{\sigma}$(geometric standard deviation) is commonly used to make quick comparison, in practice a log-normally distributed spray, with a geometric mean diameter $\overline{D}_d$ will have 68% of the droplets in the range $\left[\overline{D}_d/\sigma_g\,,\overline{D}_d * \sigma_g\right]$

The Rosin – Rammler distribution (Rosin & Rammler,1933) was originally presented for applications to powdered materials. It has been applied by a number of investigators with varying success to droplet systems. This distribution functions is generally given in the form:

$$f(D_d) = \left(\frac{\alpha_R}{r_R^{\alpha_R}}\right)\left(\frac{D_d}{2}\right)^{\alpha_R - 1}\ exp\left[-\left(\frac{D_d}{2\,r_R}\right)^{\alpha_R}\right] \qquad 1.7$$

Where r_R is the droplet radius for which the 63% of the liquid mass is made up of droplets with smaller radii. α_R determines the shape of the distribution and Beck & Watkins found that many distributions were well approximated by $\alpha_R = 2$ (Emekwuru, 2012).

The Nukiyama – Tanasawa distribution (Nukiyama & Tanasawa, 1939) function is defined as:

$$f(D_d) = K_D\, {D_d}^p\, exp\left[-\left(\frac{D_d}{m}\right)^n\right] \quad 1.8$$

Where K_D, m, p and n are adjustable constants that are affected by the conditions of the atomizing system.

Mugele & Evans (1951) made a full confrontation with those distribution and found that the log-normal distribution produce reasonable approximations to both number and volume droplet size distribution functions. The Nukiyama – Tanasawa was found to give a good fit to experimental droplet number size distributions but a poor fit to the volume size distributions. Conversely, the same study found the Rosin – Rammler distribution present a good fit to experimental droplet volume size distribution but a poor fit to number size distribution.

1.2.3 Droplet Shape

Water droplets falling through a gaseous atmosphere do not adopt a tear-drop shape. If big enough the droplets can, as first approximation, be considered to be oblate ellipsoids with semi-major axis a and semi-minor axis b. Pruppacher & Beard (1970) have proposed the correlation for droplet eccentricity for free fall at atmospheric pressure:

$$\frac{1}{E} = \frac{b}{a} = \begin{cases} 1.03 - 0.62 D_d & , 0.1 \leq D_d \leq 0.9\ cm \\ 1 & , D_d < 0.1\ cm \end{cases} \quad 1.9$$

- a b, semi-major and semi-minor axis
- E, eccentricity
- D_d, the diameter of the spherical droplet that would have the same volume of the real droplet

The eccentricity values indicate that only the largest droplets are distorted significantly from the spherical shape, thus the droplets generated by the high pressure spray systems can be assumed as spherical.

1.2.4 Droplet Velocity

The maximum droplets initial velocity can be calculated from an energy balance (Bernoulli equations):

$$z + \frac{p}{\rho/g} + \frac{V^2}{2g} = constant \quad 1.10$$

- z, elevation of the point above a reference plane [m]
- p, pressure [Pa]
- ρ, droplet fluid density [kg/m^3]
- g, acceleration due to gravity [m/s^2]
- V, flow speed [m/s]

$$V = \sqrt{\frac{2p}{\rho}} \qquad 1.11$$

After the initial velocity, the droplet velocity can be calculated with the conservation of momentum, where the axis of the spray is considered perpendicular to the floor:

$$\frac{d}{dt}(mV) = mg - \frac{1}{8}\rho\, C_d\, \pi\, {D_d}^2\, (V - V_a)|V - V_a| \qquad 1.12$$

m is the droplet mass and C_D is the drag coefficient that depends primarily on the Reynolds number:

$$C_D = \begin{cases} \frac{24}{Re}, for\ Re \leq 1 \\ \frac{24\,(0.85 + 0.15\,Re^{0.687})}{Re}, for\ 1 < Re \leq 10^3 \\ 0.44, for\ Re > 10^3 \end{cases} \qquad 1.13$$

After a period of time the droplets reach an equilibrium velocity, called terminal or settling velocity, determined through the condition of balance among weight, buoyancy and fluid friction

$$v_s = \frac{\frac{D_d^2}{2} g(\rho_d - \rho_g)}{9\mu} \qquad 1.14$$

- v_s ,terminal velocity [m/s]
- g , acceleration due to gravity [m/s^2]
- $\rho_d\ \rho_g$, droplet and gas density [kg/m^3]
- μ, dynamic viscosity of the carrier gas [kg/m/s]

Terminal velocities increase with size, consequently the largest droplets will sweep the smallest droplets that they might meet during the fall.

1.2.5 Droplet Trajectory

Before reaching their terminal velocity and a strictly vertical trajectory, the droplets will follow an oblique trajectory calculated with the following equations:

$$\frac{dV_r}{dr} = \frac{-0.75\,\rho_g\,|V|\,C_D\,V_r}{\rho_l\,D_d} \qquad 1.15$$

$$\frac{dV_z}{dz} = \frac{g\,(\rho_l - \rho_g)}{\rho_l} - \frac{0.75\,\rho_g\,|V|\,C_D\,V_z}{\rho_l\,D_d} \qquad 1.16$$

$$\frac{dr}{dt} = V_r \qquad 1.17$$

$$\frac{dz}{dt} = V_z \qquad 1.18$$

- C_D is the drag coefficient;
- r is the radial position relative to the nozzle;
- z is the axial position relative to the nozzle;
- V_r is the radial component of the droplet velocity $\left[\frac{m}{s}\right]$;
- V_z is the axial component of the droplet velocity $\left[\frac{m}{s}\right]$;
- $|V| = \sqrt{V(r)^2 + V(z)^2}$ is the droplet velocity $\left[\frac{m}{s}\right]$;

To solve these equations initial conditions are required.
The spatial condition is the start in the origin of the spray (the nozzle injection with r=z=0).
The velocity initial velocity can be easily calculated with:

$$|V|_{initial} = \frac{\dot{V}}{A_n \, D_c} \qquad 1.19$$

- $\dot{V}$ volumetric flow rate [m^3/s]
- A_n is the nozzle area [m^2]
- D_c is the discharge coefficient with typical value between 0.6 and 1

From this equation it is possible to obtain the radial and axial initial velocity by knowing the opening angle of the spray.

1.2.6 Droplet Agglomeration

Because of drag and the overlap of spray patterns there is relative motion among droplets, this creates the opportunity for droplet collisions that can take place because of differences in their horizontal and vertical velocity components. Simple contact between droplets does not necessarily result in coalescence. The colliding droplets can coalesce, recoil or be disrupted. Spengler and Gokhale (1973) determinate that a criterion for coalescence of water droplets is that the collision energy have to be less than 15 ergs. In a spray this criterion is nearly always respected with the exception of the near nozzle region. Even when the energy criterion is satisfied, the efficiency with which collision of droplets results in coalescence is not unitary.

The meaning of collision efficiency is defined, as shown in the next figure (Lehtinen 1997), as the ratio of the effective collision cross-section to the geometrical collision cross section $\varepsilon = A/B$. If the droplet moving with larger velocity would sweep all droplets that are in its geometrical path, ε would be 1. This is, however, not the case because of the curved streamlines generated by the droplets boundary layer.

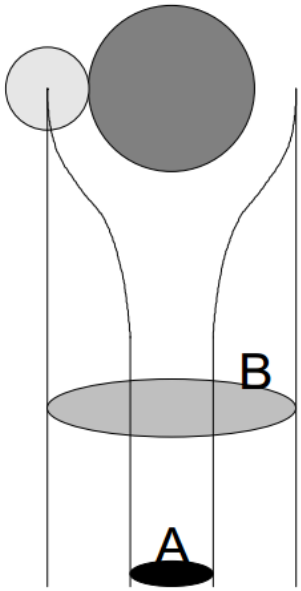

Figure 4: Meaning of collision efficiency, (Lehtinen 1997)

A widely used agglomeration expression is (Powers and Burson, 1993):

$$\varepsilon(i,j) = \frac{k}{\left[1+\frac{R(j)}{R(i)}\right]^2} \quad \text{for} \quad \frac{R(j)}{R(i)} < 1 \qquad 1.20$$

where R(i) and R(j) are the droplet radii of the colliding droplets and k is a multiplicative constant, Powers and Burson assume k = 1, in some other code like ECART it is assumed k=3/2 as it was originary hypnotized by Fuchs (N.A. Fuchs 1964). Experimental data showed up that this expression overestimates the agglomeration efficiency between droplets of similar size, so a series of truncated expression have been used like:

$$\varepsilon(i,j) = \begin{cases} 1 - 8\,\dfrac{R(j)}{R(i)}, & for\ \dfrac{R(j)}{R(i)} < 0.125 \\ 0, & for\ \dfrac{R(j)}{R(i)} \geq 0.125 \end{cases} \qquad 1.21$$

The efficiencies showed in the next figure represent the evolution of the relative efficiency for a 600μm droplet that collide with smaller ones (the diameter of the small droplet is on the horizontal axis) and shows that a truncated expression better fits the experimental data.

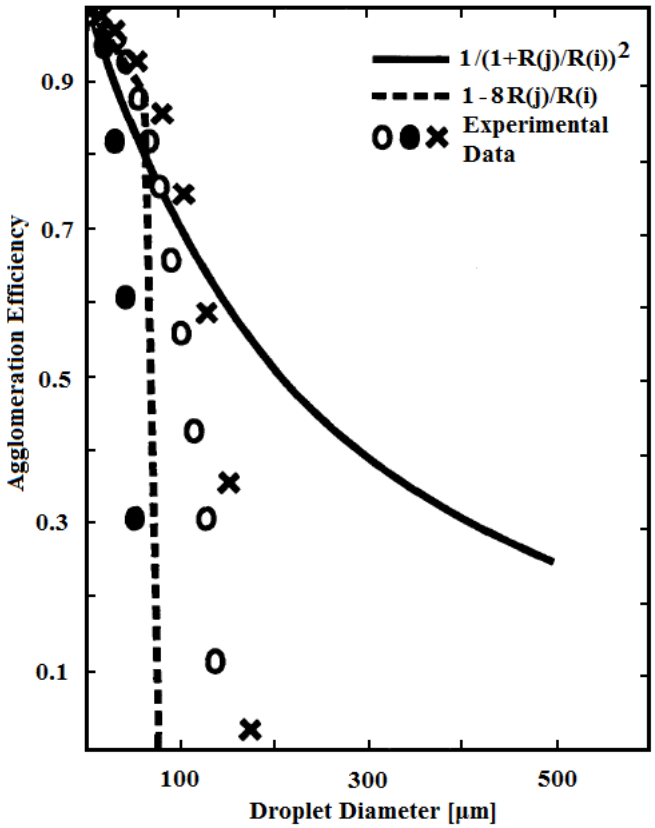

Figure 5: Comparison of different collision efficiency and experimental data of a 600µm droplet (D.Power, S. Burton, 1993)

1.2.7 Droplet-Structure interaction

The droplets, during the fall, will encounter solid structures and interact with them in different ways: they can bounce over the surface, they can spread forming a thin film or they can splash with the formation of smaller droplets.

Baker et al (1988) showed that the different behaviors are a function of the inertia forces and the superficial tension of the falling droplet, so they can be expressed in function of the Weber number. For We < 5 the droplets bounce when they encounter a structure surface. For 5 ≤ We < 65 the droplets spread on the surface forming a film layer. For We ≥ 65 the droplets begin to splash when they hit a surface, while for We ≥ 3000 each droplet, that impacts on a surface, splashes as shown in the next figure:

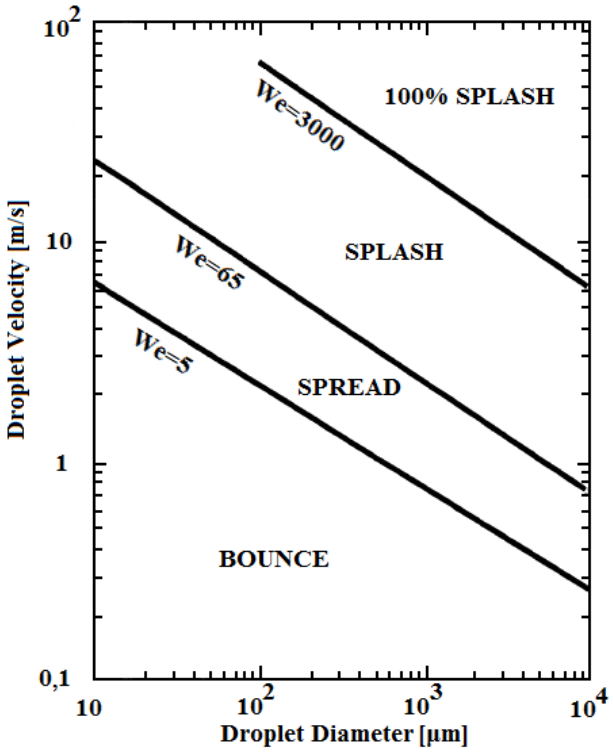

Figure 6: Droplet behaviour after impacting a surface as function of the Weber number (D.Power, S. Burton, 1993)

1.2.8 Particle capture mechanisms

A falling water droplet can interact with suspended particulate with different mechanisms:

- impaction;
- interception;
- diffusion;
- thermophoresis;
- diffusiophoresis.

Thermophoresis and diffusionphoresis are phoretic forces, generated from different gradients in temperature (cold droplet in hot environment) and pressure (condensing vapor around the water generate a flow that tends to push the particles toward the droplet).
In our condition, no steam condensation/vaporization and no difference of temperature between particles and environments occur so the main capture mechanisms for water droplets are impaction, interception and diffusion.

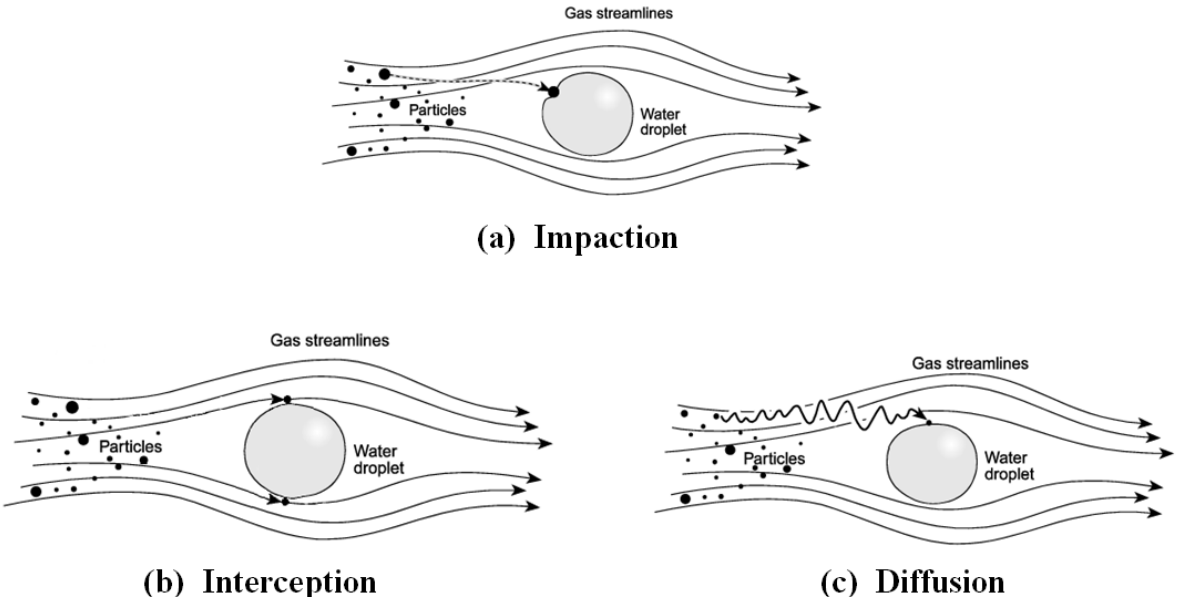

Figure 7: Main particulate capture mechanisms for falling water droplets

Impaction and interception of aerosol particles are affected by the atmosphere hydrodynamics. As a droplet falls through the atmosphere, a flow field develops around the droplet. This flow field will carry along aerosol particles. The flow field will, ideally, carry the aerosols around falling droplets. Some aerosols will, however, be too massive to respond to the sudden accelerations in the gas flow in the vicinity of the falling droplet. Inertia will carry these particles across streamlines of the flow so that the particles impact on the droplet surface. It is assumed here that contact between a droplet and a particle is sufficient to cause capture of the aerosol particle. Surface tension and Van der Waals forces are sufficient to keep the particle in contact with the droplet even if the material that makes up the particle is not soluble in the droplet.

If the centre of mass of an aerosol particle can follow the streamlines of the flow field around a falling droplet, the finite size of the aerosol particle may lead, nevertheless, to contact between the droplet and the particle.

Very small particles are more able to follow the streamlines of the flow field around a droplet and are, therefore, less susceptible to capture by impaction or interception. But, these very small particles respond to the stochastic impulses of collisions with gas molecules. Because these impulses are not perfectly balanced on the time scales of interest during the passage of a droplet, there is an apparent diffusion of aerosol particles that can carry the aerosols across the streamlines of the flow, leading to aerosol contact with the droplet and, consequently, aerosol capture. Convection of the gas can enhance this diffusive flux of particles into the droplet.

The quantitative descriptions of these particle-capture processes presented below are based on analyses for isolated spherical droplets.

Consider a single droplet of diameter $D_d(e)$ falling through the space. After falling a distance X it will sweep a volume of gas of $\frac{\pi}{4}\mathrm{Dd(e)}^2\mathrm{X}$

If the gas contains a concentration of n(i) particles of diameter d_p(i), then in absence of hydrodynamic phenomena, the falling sphere will sweep out $\frac{\pi}{4}\mathrm{Dd(e)}^2\mathrm{X}$ n(i) particles.

A convenient definition of capture efficiency is the ration between the actual number of captured particles and the number captured in the hypothetical situation:

$$\varepsilon\big(Dd(e), dp(i)\big) = \frac{4\Delta N(i)}{\pi Dd(e)^2 X\, n(i)} \qquad 1.22$$

- $\varepsilon\big(\mathrm{Dd(e)}, \mathrm{dp(i)}\big)$= efficiency with which a drop of diameter D_d(e) captures particles of diameter d_p(i)
- $\Delta N(i)$= actual number of particles captured in the fall of a distance X

Hydrodynamic effects cannot be neglected in the analysis of aerosol capture by falling water droplets. The efficiency with which droplets capture aerosol particles depends on the nature of flow around the droplet. Analytic results are, however, available only for the limiting flow regimes of viscous flow (Re→0) an potential flow (Re→∞). The collection efficiency for different flow regime due to impaction are reported in Figure 8 and due to interception in Figura 9 Pemberton (1960) has argued that in view of the substantial size differences between aerosols of interest (diameters less than 10 μm) and droplets of interest (diameters around 100 μm), flow around the droplets is well approximated by potential flow.

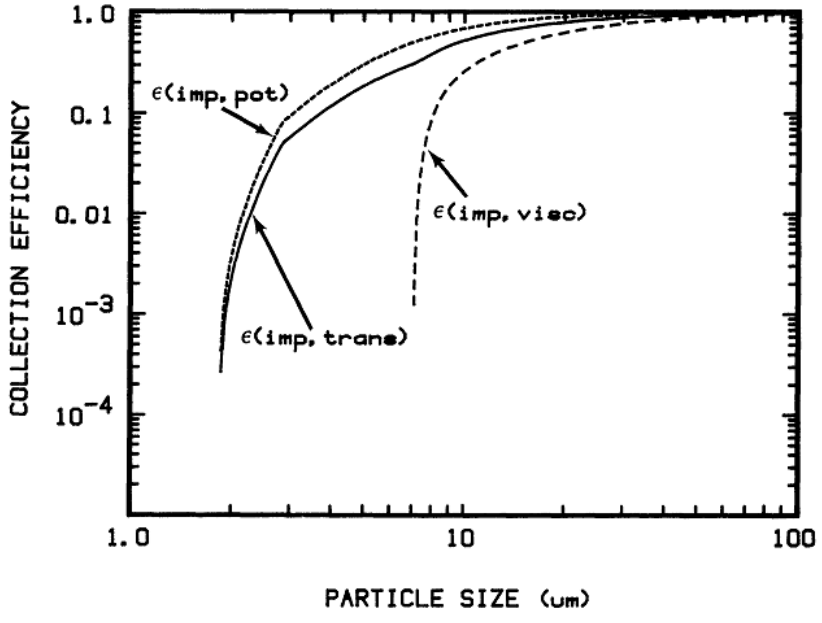

Figure 8: Impaction efficiency, (Powers and Burson, 1993)

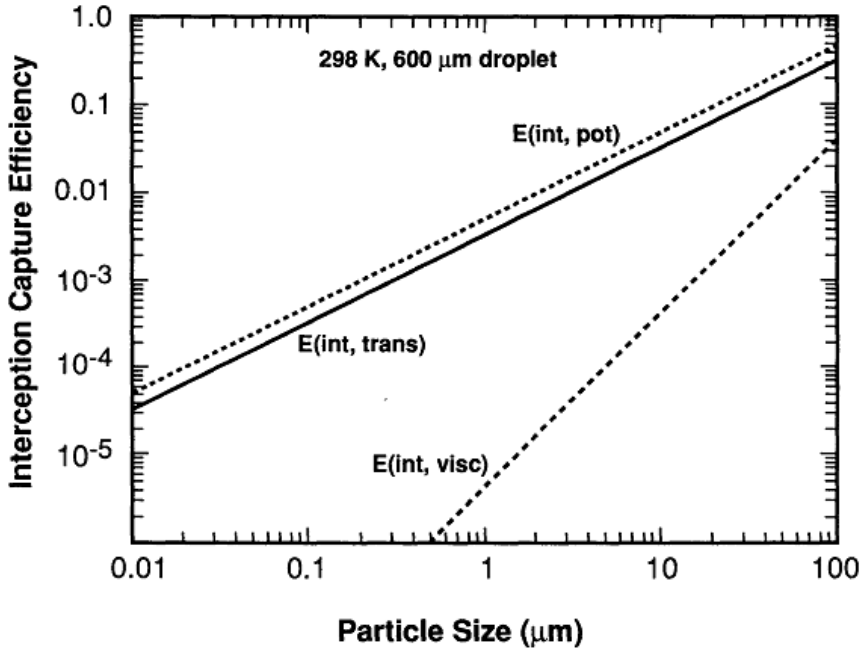

Figura 9: Interception efficiency, (Powers and Burson, 1993)

The discussions of aerosol capture efficiency also show that spray performance will depend very strongly on the size distribution of aerosols in the containment. Both the mean size and the span of the aerosol size distribution will affect the predicted performance of the containment spray. Further, the spray will alter the size distribution because very large and very small particles will be removed more efficiently than the particles near the size of minimum capture efficiency. The effectiveness of the spray will decrease as decontamination progresses. In Figure 10 the overall capture efficiency is reported.

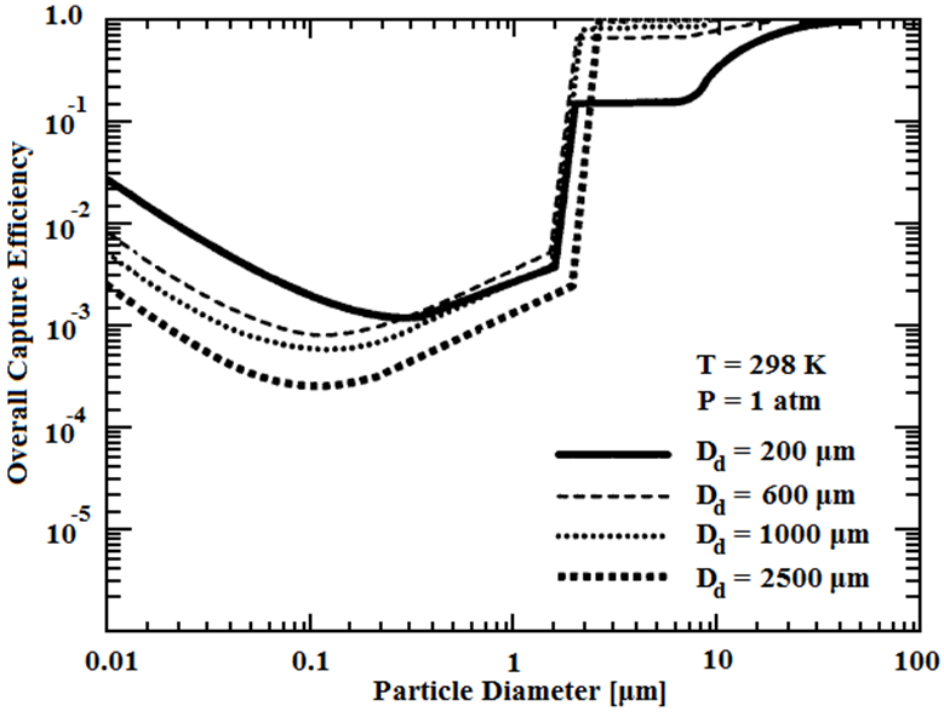

Figure 10: Overall capture efficiency, (Powers and Burson, 1993)

The overall capture efficiency is affected by the atmosphere hydrodynamics, the particle size and the droplet size. The efficiency of impaction increases with increasing the particle size, it affects the particles larger than about 5 μm. The capture by diffusion increases with decreasing the particle size, it becomes important for particles smaller than about 0.1 μm in diameter. Interception affects the particles in the size range from 0.5 μm to 2 μm. The combination of these effects contributes to have, in a high pressure system, the minimum of capture efficiency for particles approximately with a diameter between 0.1 μm and 1 μm.

1.3 Performances of water spray installed in current nuclear power plants

Containment sprays have been used as safety systems in Light Water Reactor (LWD) for many years. These systems have been installed in reactors as part of the systems to suppress steam pressurization during design basis loss-of-coolant accidents. They are intended to supply enormous amounts of water to condense steam quite promptly after a hypothesized rupture of a large pipe in the reactor coolant system. Sprays are also considered as useful clean-up systems of the containment atmosphere because they would be capable of significantly removing particles and molecular iodine from the containment atmosphere and to enhance the gas mixing in case of the presence of hydrogen.

The spray installed in the current nuclear power plants are designed to work with a water pressure of 3 to 9 bar and to produce droplets with diameter in the range of 20-2000 μm and velocities around 10-20 m s^{-1} (Powers and Burson, 1993).

A recent study (Porcheron et. al 2008 and 2010) has provided a clear view on the actual performances of current spray systems with an experimental program called TOSQAN that have the objective to simulate typical thermal hydraulic conditions representative of a severe accident in the reactor containment. Their facility has a volume of 7 m^3 and the spray operates at 5 bar, providing a total water flow rate of $3*10^{-5}$ m3/s with droplet of 143 μm average diameter and velocity in the range of 4-12 m s^{-1} as showed in Figure 11 andFigure 12.

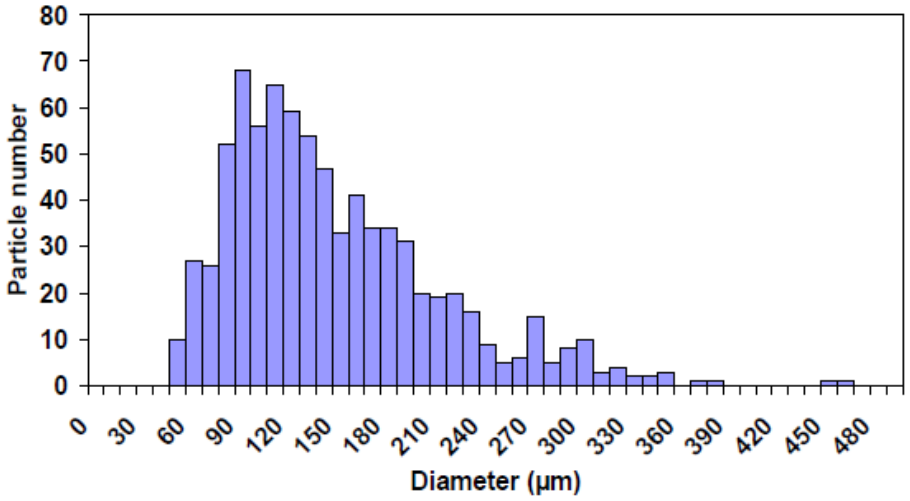

Figure 11: droplet size distribution of TOSQAN experiments, (Porcheron et. al 2008, 2010)

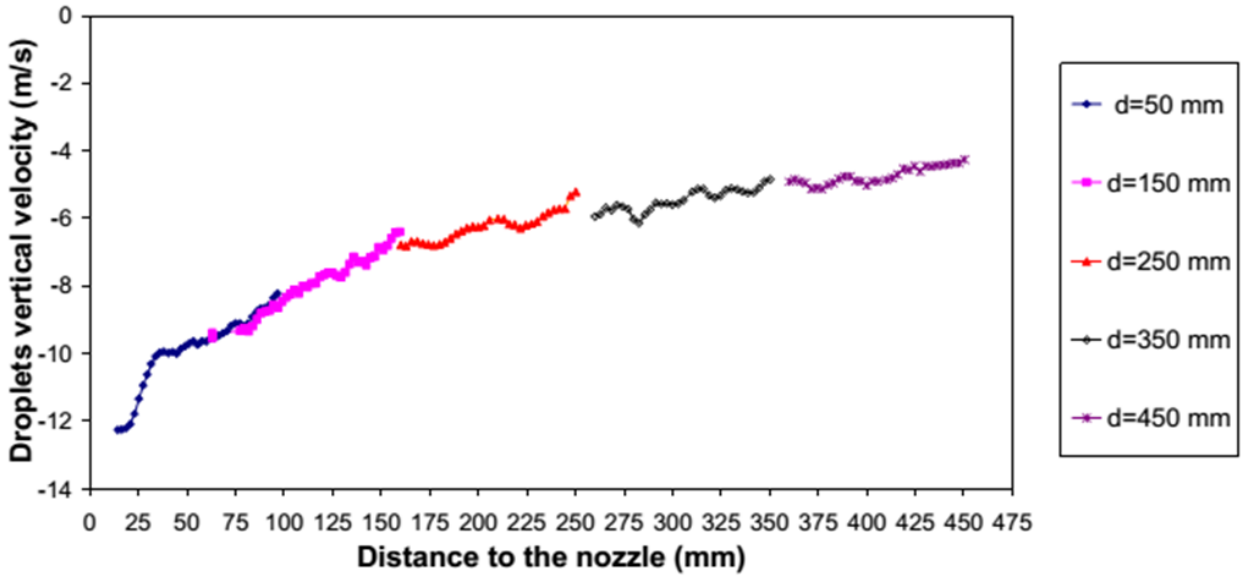

Figure 12: evolution of the droplet velocity of TOSQAN experiments, (Porcheron et. al 2008, 2010)

The aerosol used has an average diameter of 2 µm with a geometrical standard deviation of 1.5. The decontamination curves showed in Figure 13 bring to light that the average half-life time is of the order of several minutes, in particular 500 s in the case of 2 µm aerosol, 900 s for 1 µm and 1200 s for particulate of 0,5 µm diameter.

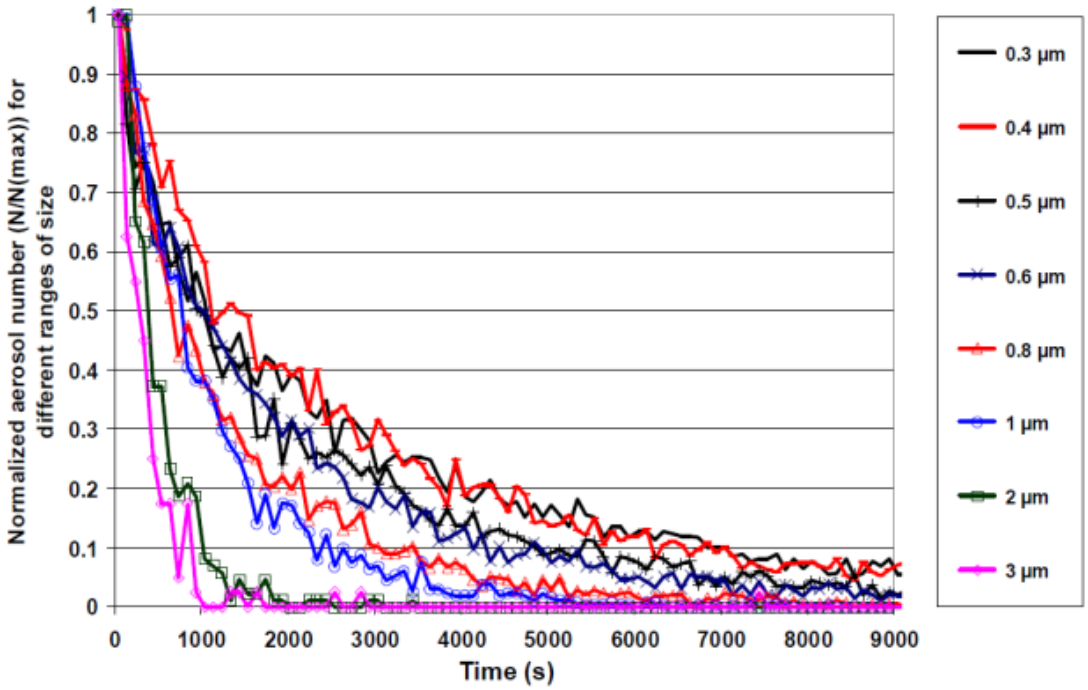

Figure 13: decontamination curves obtained in TOSCANQ experiments, (Porcheron et. al 2008, 2010)

They have stated that the Postma equation (Postma 1978) well approximates the aerosol removal rate of their system $\lambda_{TOSCANQ}$=0.0011 s^{-1}.

$$\lambda = \frac{3}{2}\frac{Q_{volumic} * h}{D_{droplet} * V_{containment}}E \qquad 1.23$$

Where:

- λ is the aerosol removal rate [s^{-1}];
- $Q_{volumic}$ is the volumetric water flow rate [m^3 s^{-1}];
- h is the droplet fall height [m];
- $V_{containment}$ is the total volume of the containment [m^3];
- E is the total collection efficiency;

The total collection efficiency is function of all the different mechanisms of particle capture, as seen in chapter 1.2.8.

$$E = 1 - \left(1 - \varepsilon_{imp}\right)(1 - \varepsilon_{int})\left(1 - \varepsilon_{diph}\right)\left(1 - \varepsilon_{termph}\right) + \varepsilon_{db} \qquad 1.24$$

The formulations used for the main efficiency are:

Inertial impaction, for Stokes number $Stk = \frac{d_p^2 \rho_p v_w}{9\mu_g d_w} \geq 0.2$:

$$\varepsilon_{imp} = \left[\frac{Stk}{Stk + 0.5}\right]^2 \qquad 1.25$$

Interception, for $d_p << d_w$:

$$\varepsilon_{int} = 3\left(\frac{d_p}{d_w}\right) \qquad 1.26$$

Brownian diffusion, function of Reynolds Peclet number, $Pe = \frac{v_w d_w}{Diffusivity\ air-water}$:

$$\varepsilon_{db} = 3.02 Re_w^{\frac{1}{3}} Pe^{-\frac{2}{3}} \qquad 1.27$$

ε_{diph} and ε_{termph} rapresent the contribution due to termophoresis and diffusionphoresis.

The fact that the Postma equation could give reliable results for our test configuration will be evaluated in chapter 5.1.

2 Decontamination measurement

This chapter provides a detailed analysis of the facility, instruments and results of the decontamination measurements with the aim of determining the evolution of the decontamination factor (DF) λ of the powder suppression process with the variation of the main parameters of interest: water pressure, particulate size distribution and concentration.

2.1 SCRUPOS facility

SCRUPOS (SCRUbbing by Pool and Spray) is the experimental facility built-up by RSE to fulfil the PASSAM project assignment on both pool and high pressure spray scrubbing.

Figure 14: the SCRUPOS facility

Figure 15 shows the system diagram, whose main components are:

- A parallelepiped-shaped scrubbing chamber with a height of 1.5m and a basis of 1 x 0.5 metres. The structure is composed of a stainless steel frame and two main windows of tempered glass. Six measurement access points are predisposed on the lateral surface.
- An aerosol injection line where a dust dispenser releases particulate matters to a pressurized air vein in a controlled manner. Air flow mass-rate and pressure are monitored respectively with a thermal mass flow and a piezo-resistive trasducer.

- The water injection line where demineralized water is fed by a high-pressure volumetric pump through the nozzle in the chamber.
- The pickup line where samples of the air with particle suspension are diluted by a Dynamic Dilution System and then analysed by an Optical Particle Sizer Spectrometer (OPS)

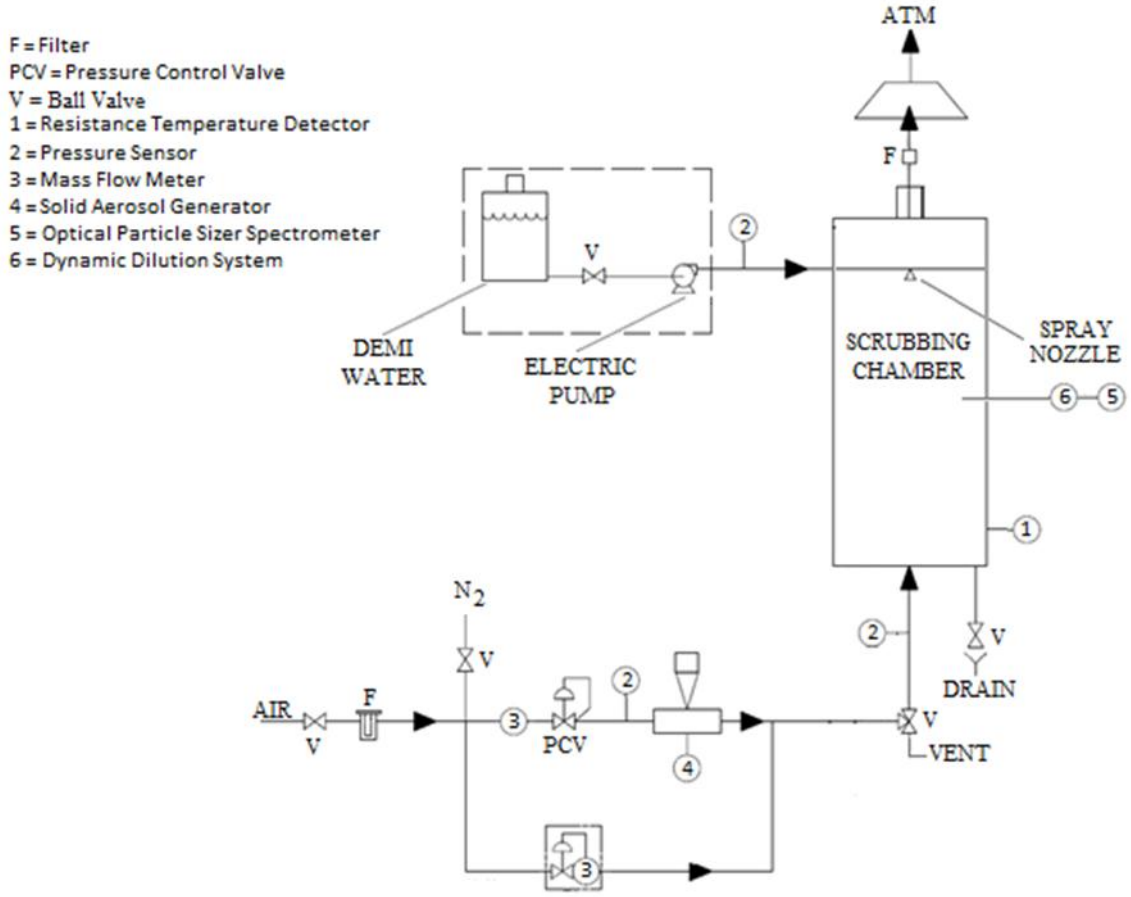

Figure 15: SCRUPOS layout

The air flow is monitored and controlled with a Labview routine while the aerosol analysis were performed with Aerosol Instrument Manager software provided by TSI with the OPS.

2.2 Instrumentation

This chapter provides a short description of the main instrument used and their measurement principles.

2.2.1 Piezo-resistive sensor

The air flow pressure is measured with a piezo-resisitive transducer (PCE-28) made by Aplisens firm.

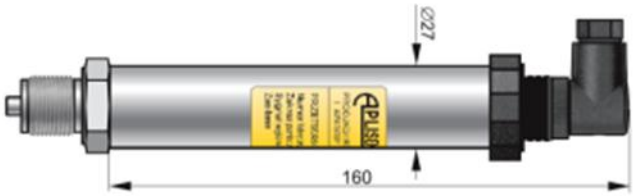

Figure 16: PCE-28 pressure sensor

This sensor can measure the absolute pressure of gases, vapours and liquids in a range comprised between 400 mbar and 80 bar with an accuracy better than $\pm 0.1\%$

The sensor is composed of four resistors connected to a flexible silicon diaphragm that bends under the effect of pressure, in a full Wheatstone bridge configuration, to compensate the effect of temperature. The stress force applied to the resistors produce a variation in the resistivity of the material inducing a voltage drop proportional to the pressure.

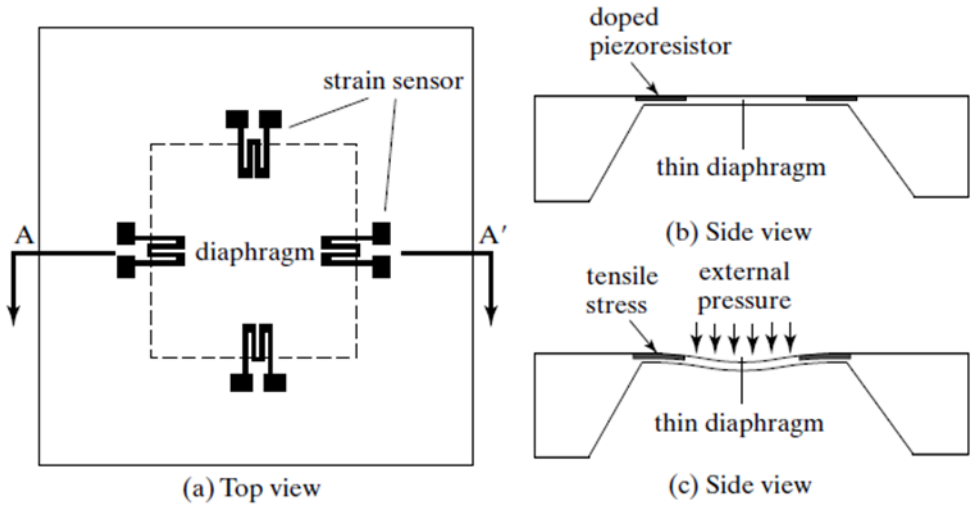

Figure 17: Pressure sensor scheme

2.2.2 Thermal mass flow controller

For both measure and control of the inlet air flow the flow rate controller SLA5853S is used. It provides a wide range of adjustable flow values (100 to 2500 lpm with an accuracy of $\pm 0.2\%$) with a response time lower than three seconds.

Figure 18: SLA5853S thermal mass flow controller

The air flows through the thermal mass flow controller and is separated in two different flows, the first one called flow A is sent to the flow sensor, while the second one called flow B passes through a restrictor.

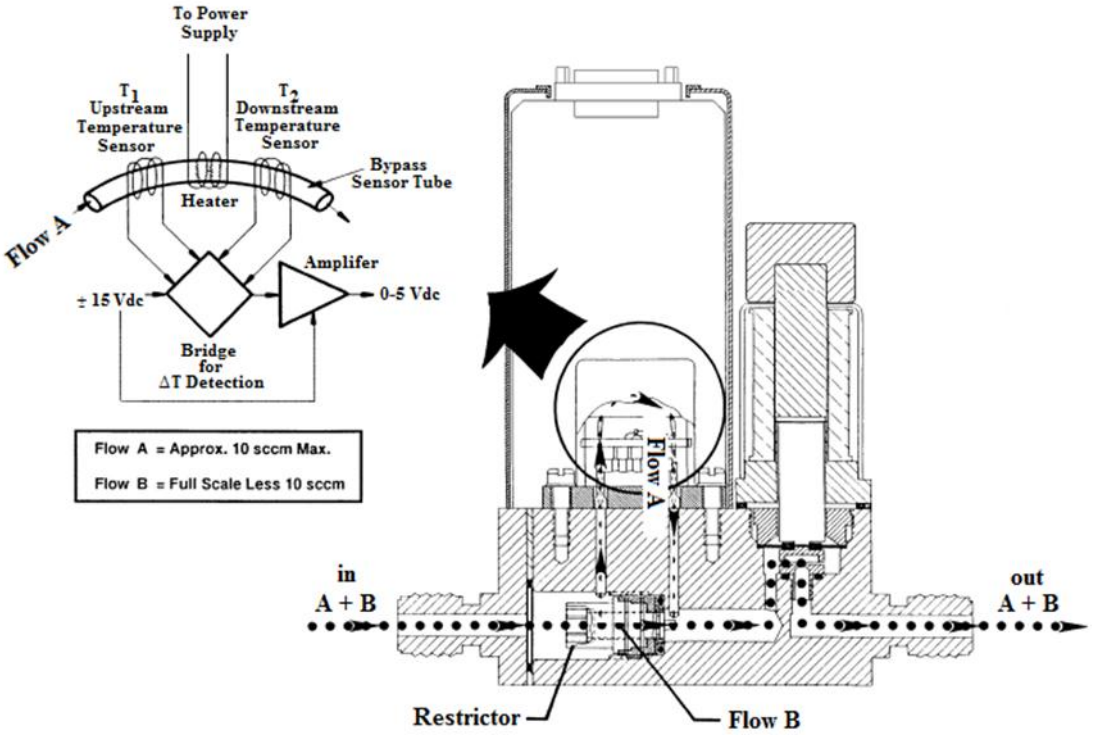

Figure 19: Thermal mass flow controller scheme

The pressure difference across the restrictor, which varies linearly with the total flow rate, forces the gas to flow into the sensor where a controlled heat flow is imposed to the air stream. The temperature increase is proportional to the air flow rate.

$$\Delta T = A \times \dot{Q} \times Cp \times \dot{m} \qquad 2.1$$

- ΔT [K] is the temperature difference;
- A [s^2K^2/kJ^2] is a proportionality constant;
- $\dot{Q}$ [kW] is the heater power;
- Cp [kJ/kg/K] is the specific heat of the gas;
- $\dot{m}$[kg/s] is the mass flow

A bridge circuit and a differential amplifier generate an electrical signal directly proportional to the gas mass flow rate.

2.2.3 Dust dispenser

The dispenser SAG 410 manufactured by TOPAS is used to feed amorphous SiO2 particles to the air flow entering the scrubbing chamber.

Figure 20: SAG 410 dust dispenser

The dispersing unit consists in a special segmental feeding belt with defined constant small volumes. The powder is loaded into the cylinder on top of the dispenser, where a scraper ensures that a uniform amount of dust reaches the feeding belt. The amount of particles injected is controlled by varying the speed of the belt using the control interface. An ejector removes the dust from the belt by suction, the generated shear forces will disperse and de-agglomerate the powder to form an aerosol that is finally mixed with the main air flow.

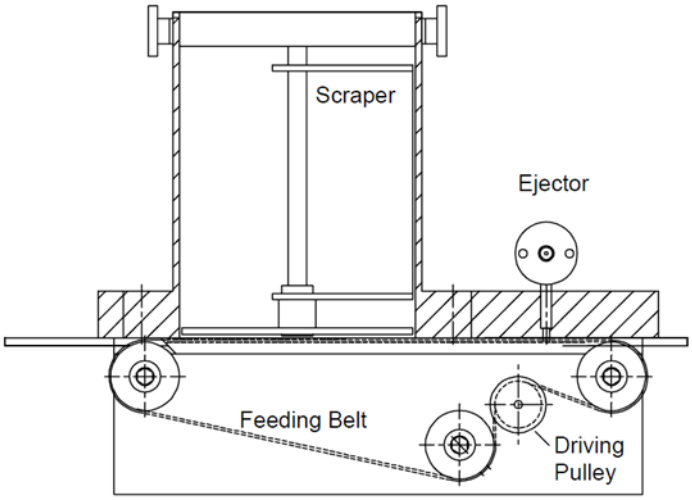

Figure 21: Dust dispenser scheme

2.2.4 Optical Particle Sizer Spectrometer

The Optical Particle Sizer (OPS) 3330 manufactured by TSI Incorporated is used to measure the aerosol concentration and particle size distribution. It uses a single particle counting technology that exploits the light scattering phenomenon.

Figure 22: Optical Particle Sizer 3330

A sample aerosol is aspirated from the test chamber by an internal pump and after a dilution process it goes into the measurement region of the instrument. The pump provides a constant air flow to the instrument, because the concentration measured by the OPS is sensitive to the flow rate, which is monitored by two pressure transducers and kept at 1 L/min $\pm$ 5%. The sample flow entering the measuring chamber is surrounded by a sheath flow supplied by the pump exhaust, that has the task to keep it confined on the laser beam and to keep the optics clean . As the particle passes through the beam, the scattered light is picked up by a 120° elliptical mirror and focused onto the photo detector. This signal, whose intensity is proportional to the particulate dimensions, is then processed by the electronics and individual counts are distributed among 16 size ranges, from

0.3 μm to a maximum particle diameter of 10 μm. The flow exiting the optics chamber is then filtered two times, before and after the internal pump; half of it is expelled while the other half is recirculated to act as sheath flow.

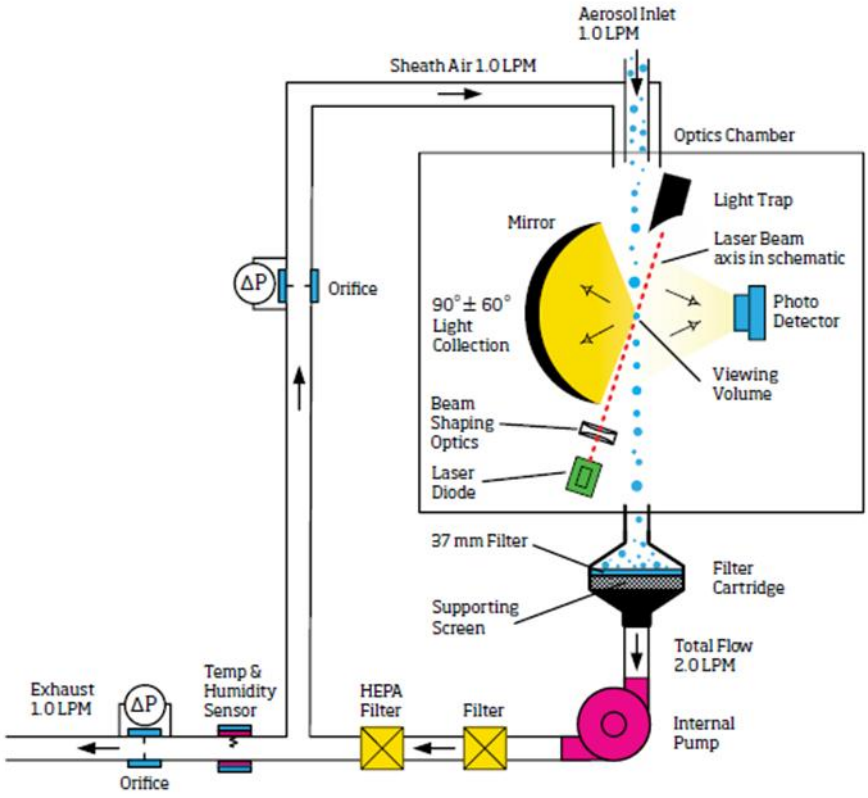

Figure 23: OPS 3330 scheme

The OPS measures particle concentration by counting individual pulses from the photo detector, meaning that, for high aerosol concentrations, the single pulses may overlap and the number of particles is underestimated. To account for this phenomenon a dead time correction factor is introduced: it compensates for the time interval in which multiple particles are present simultaneously in the viewing volume. Therefore the particle concentration is given by:

$$C_i = \frac{N_i}{Q \times (t_s - DTC \times t_d)} \qquad 2.2$$

- C_i is number concentration in the i-th size channel $\left[\frac{\#}{cm^3}\right]$
- N_i is number of particles counted in the i-th size channel in a single time sample
- Q is the sample flow rate, kept constant by the pump and equal to 16.67 $\left[\frac{cm^3}{s}\right]$
- t_s is the sample time duration $[s]$
- t_d is the dead time $[s]$
- DTC is the dead time correction factor $[-]$

Since the maximum total concentration that the OPS can detect is limited to 3000 #/cm^3 one or two diluters are mandatory to avoid coincidence errors (particles not counted for overlapping with each other).

2.2.5 Dynamic dilution system

To dilute the aerosol without altering the particle size distribution the Dynamic Dilution System 560 manufactured by TOPAS is used.

Figure 24: Dynamic Dilution System 560

The dilution is obtained by separating the main flow into a bypass and a capillarity flow. The bypass flow is sent to an HEPA filter that removes all particles, while the capillarity flow remains untouched. When they merge again the resulting flow will be diluted by an amount given by the rate of the bypass flow to the capillarity flow. This dilution rate can be controlled with a valve in the bypass line.

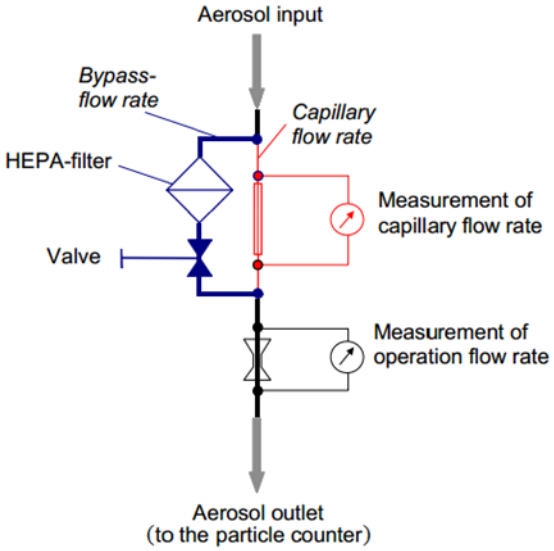

Figure 25: Dynamic Dilution System 560 scheme

2.3 Measurement setup

2.3.1 Conditions

The operating conditions of the measurement campaigns are summarize in Table 1. The aim of the work is to highlight the performances of the high pressure spray systems in decontaminating an atmosphere with a particulate suspension similar to the one present in the containment of a Light Water Reactor during a severe accident. Studies have stated (Fermandjian 1984) that the most important part of the fission products is emitted in the particulate form with a size close to 1µm with a density in the range of 2-3 g cm^{-3}. Monodisperse amorphous silica, SiO_2, has been chosen as constituent for the aerosol because it has physical proprieties similar to the fission product and has no chemical interaction with water that could lead to an overestimation of the decontamination process.

Table 1: Conditions of the high pressure spray tests

Spray fluid	Demineralized water
Spray pressure [bar]	50 - 100 - 130
Spray flow rate at 100 bar [l/min]	1.17
Nozzle number	1
Particle type	SiO_2
Particle size [µm]	0.5 – 2*
Particle concentration [mg/m^3]	1-50
Air flow to reach the desired particle concentration [l/s]	5 - 10
Air temperature	Ambient
Air pressure	Ambient
Recording time [s]	120
Sampling frequency [Hz]	1

*measurements relative to 1µm powder have been performed in a previous thesis (Casella 2014)

For each different powder, three different levels of concentration have been tested in order to evaluate its effect on the decontamination process. Ideally the initial concentration should be the same, but practically is acceptable a slight variance, due to the difficulty in creating repetitively always the same homogeneous atmosphere. The levels of concentration used in our tests are:

- Low concentration: 1-3 mg/m^3
- Medium concentration: 10-20 mg/m^3
- High Concentration: 30+ mg/m^3

For each powder composition at least two measurements have been done for every concentration level and for every different pressure for a total of more than 40 measurements as summarized in Table 2

Table 2: test matrix, to be performed twice for each different powder

Pressure [bar]	Nominal concentration [mg/m^3]
50	2 – 12 – 40
100	2 – 12 – 40
130	2 – 12 – 40

Every single measurement is composed of the following steps:

- Activate the air injection line;
- Activate the dust dispenser;
- Start particle data acquisition;
- Monitor the concentration of the size class of interest until the predetermnated nominal value is reached;
- Stop both the air and the dispenser;
- Wait 10 seconds to uniform the powder inside the chamber (the reached here will be the initial value for the data processing) (sintetico spiega per uniformare);
- Activate the water spray for 120 seconds;

2.3.2 Powder structure

Amorphous SiO_2 is used to realize our tests. It is manufactured by NIPPON SHOKUBAY and is dispatched directly from Japan in blisters of 1kg.

In a preliminary test, as shown in Figure 26, the powders distributions clearly show a peak of particle number inside the nominal granulometry size range.

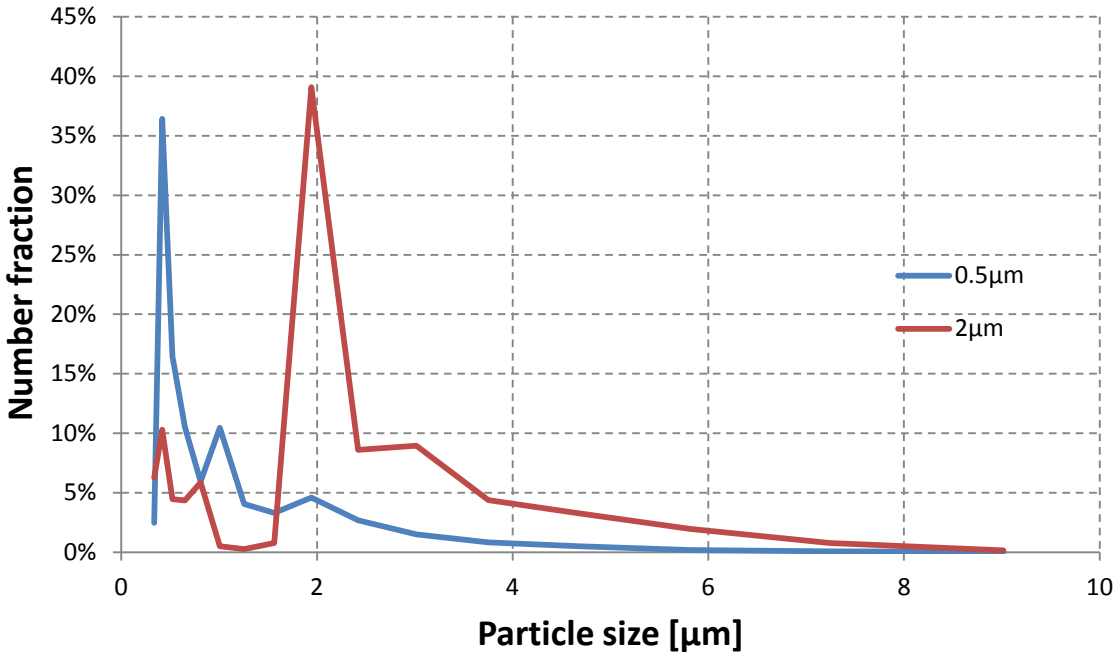

Figure 26: 0.5 and 2µm powder composition measured with OPS 3330

2.4 Data processing and analysis

This chapter includes the results of all the measurement campaigns and to offer a complete overview on the phenomena, also the measurements on the 1µm powder are included.
The experimental data, evolution of the particulate sampled every second, were interpolated using the following function:

$$C(t) = [C(0) - C(\infty)]\, e^{-\lambda t} + C(\infty) \qquad 2.3$$

where the exponential coefficient λ [1/s] is the decontamination coefficient, C(0) is the initial measure of particle concentration and C(∞) is the asymptotic value reached by the concentration at the end of the tests. The latter proved to be always small enough to result negligible.
With this assumption the equation turns in the expression:

$$\frac{C(t)}{C(0)} = e^{-\lambda t} \qquad 2.4$$

Where C(t)/C(0) is the Decontamination Factor.
The time to halves the particle has been calculated as follows:

$$\text{Half life [s]} = -\frac{\ln(0.5)}{\lambda} = -\tau \log(0.5) \qquad 2.5$$

2.4.1 0.5 µm powder

Figure 27,Figure 28 andFigure 29 show the time evolution of the decontamination process for each initial particle concentration, for different levels of the spray pressure.

All figures display that the decontamination factor increase with pressure. In fact a pressure increase will determinate a higher mass flow rate, a droplet distribution switched toward smaller diameters with higher concentration of droplets in the ambient and higher velocities.

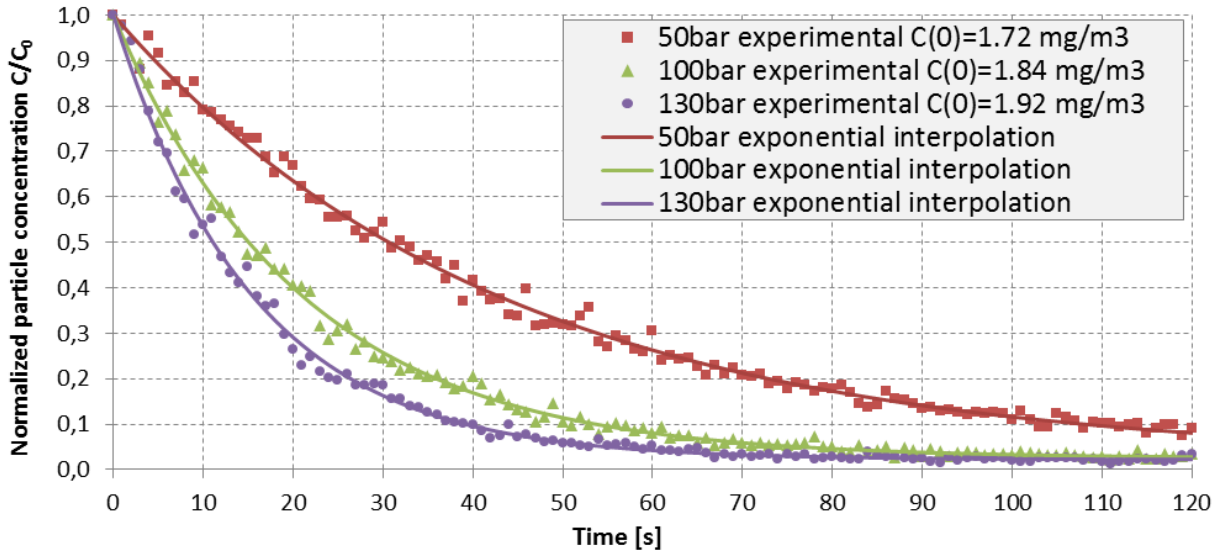

Figure 27: Decontamination curves for low initial particle concentration, 0.5µm powder

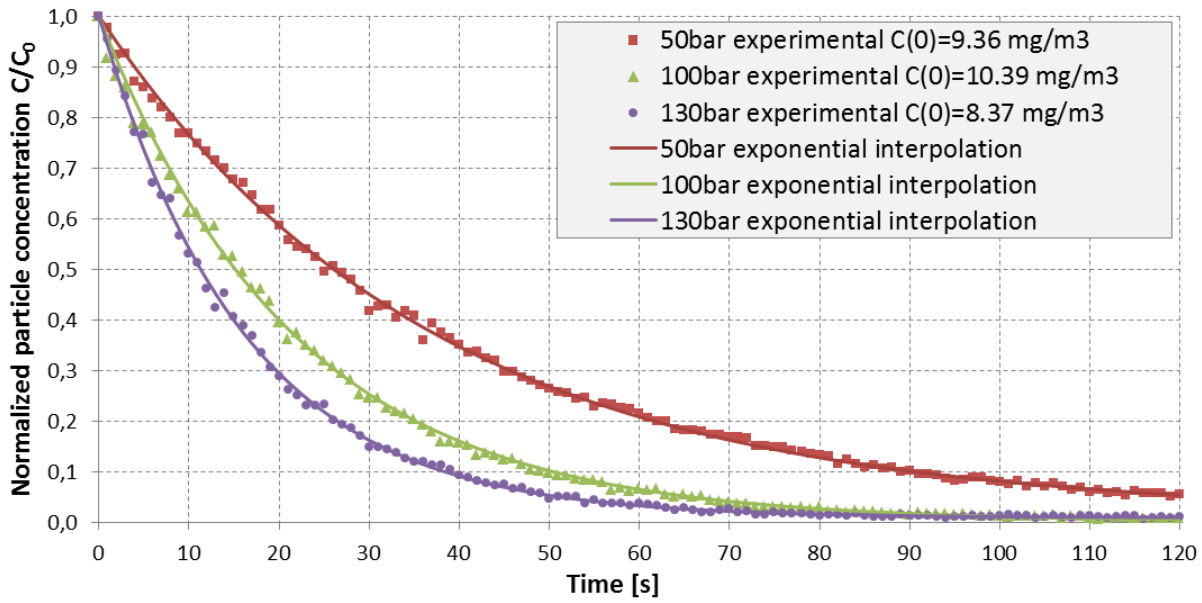

Figure 28: Decontamination curves for medium initial particle concentration, 0.5µm powder

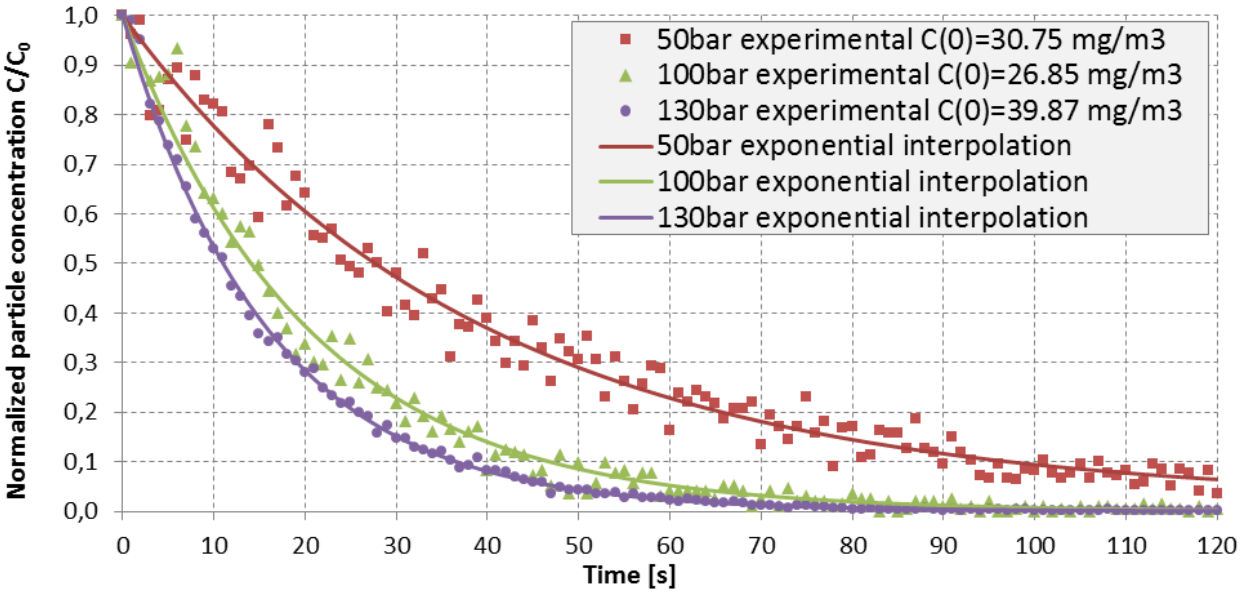

Figure 29: Decontamination curves for high initial particle concentration, 0.5µm powder

In Table 33 appear the values of the decontamination coefficient observed for this particle granulometry and is shown that λ is not influenced by the initial concentration.

This behaviour can be better observed in Figure 30 where for a determinate pressure, 130 bar in this case, the total number of particles removed increases with their initial concentration, but the half-life time is always the same.

Table 3: values of the decontamination coefficient for 0.5µm particles

P [bar]	$\bar{\lambda}$ [1/s] Low concentration	$\bar{\lambda}$ [1/s] Medium concentration	$\bar{\lambda}$ [1/s] High concentration	$\bar{\lambda}$ [1/s] Total	Half-Life time
50	0,023	0,025	0,026	0,024 ± 0,002	28,1
100	0,049	0,0483	0,051	0,049 ± 0,002	14,0
130	0,064	0,063	0,066	0,064± 0,002	10,8

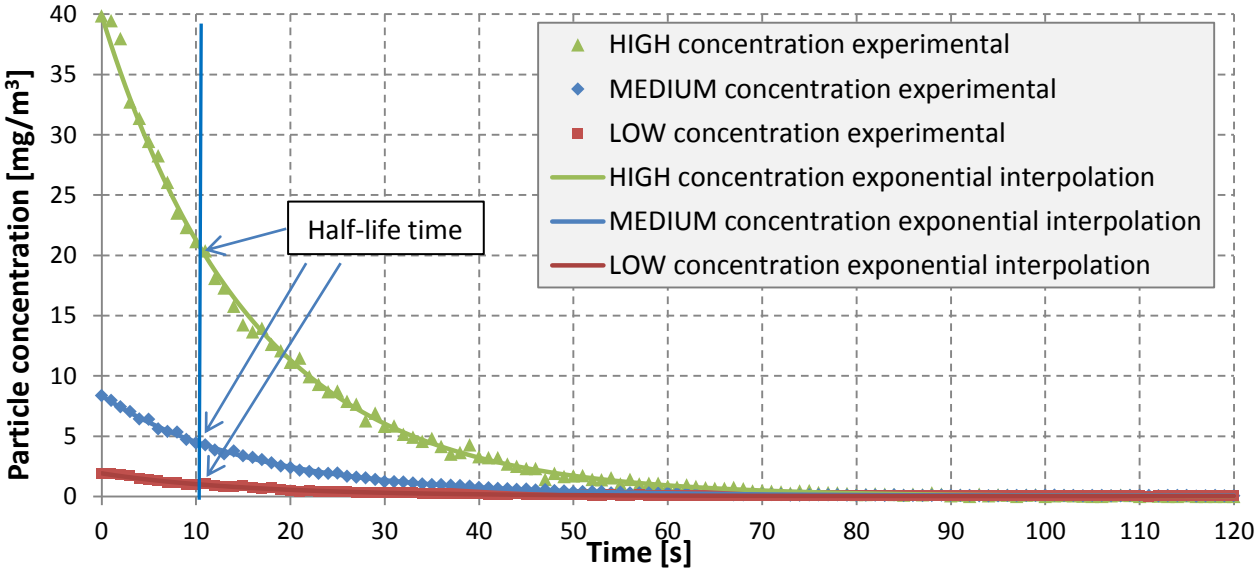

Figure 30: decontamination curves with different initial particles concentration at a fixed pressure (130bar)

Figure 31 shows that the value of the decontamination coefficient is linearly dependant on the pressure.

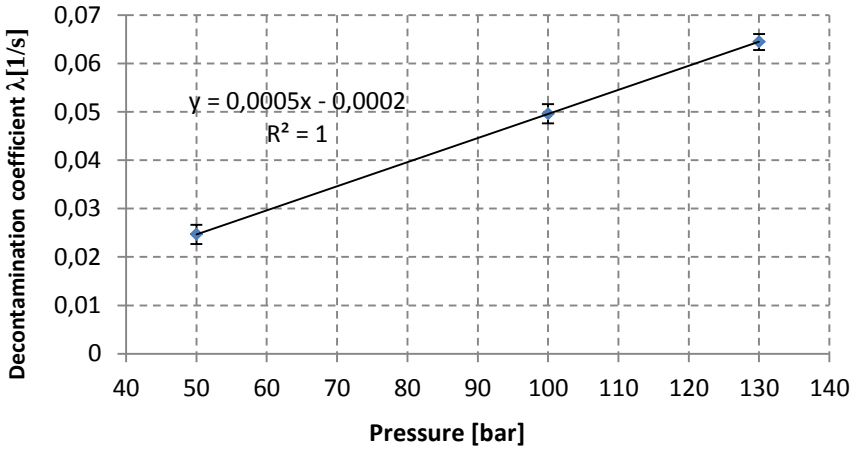

Figure 31: decontamination factor as function of water pressure for 0.5µm particles

The value of the half-life time has been interpolated and reported in Figure 32 together with the experimental results.

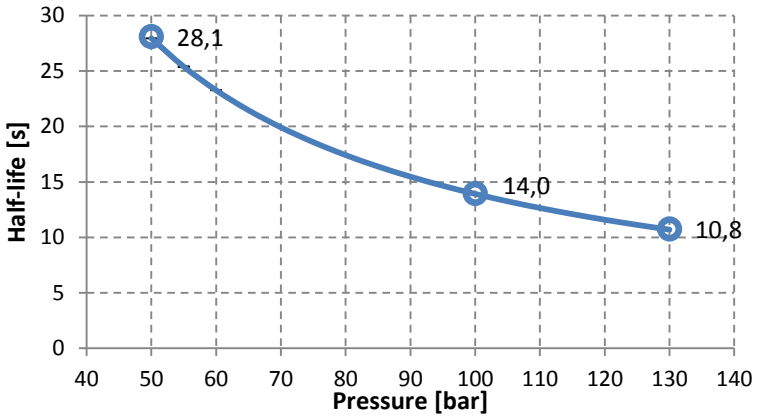

Figure 32: half-life time for 0.5 µm particles, interpolation and experimental data

2.4.2 2µm powder

The results obtained with the 2 µm powder show the same behaviour as the smaller dimension powder: an increase in the water pressure results in a better cleaning process, while the initial particle concentration doesn't affect the total decontamination factor that is linearly dependant on spray pressure. The process is overall much faster than with the 0.5µm and much smaller half-life time have been calculated.

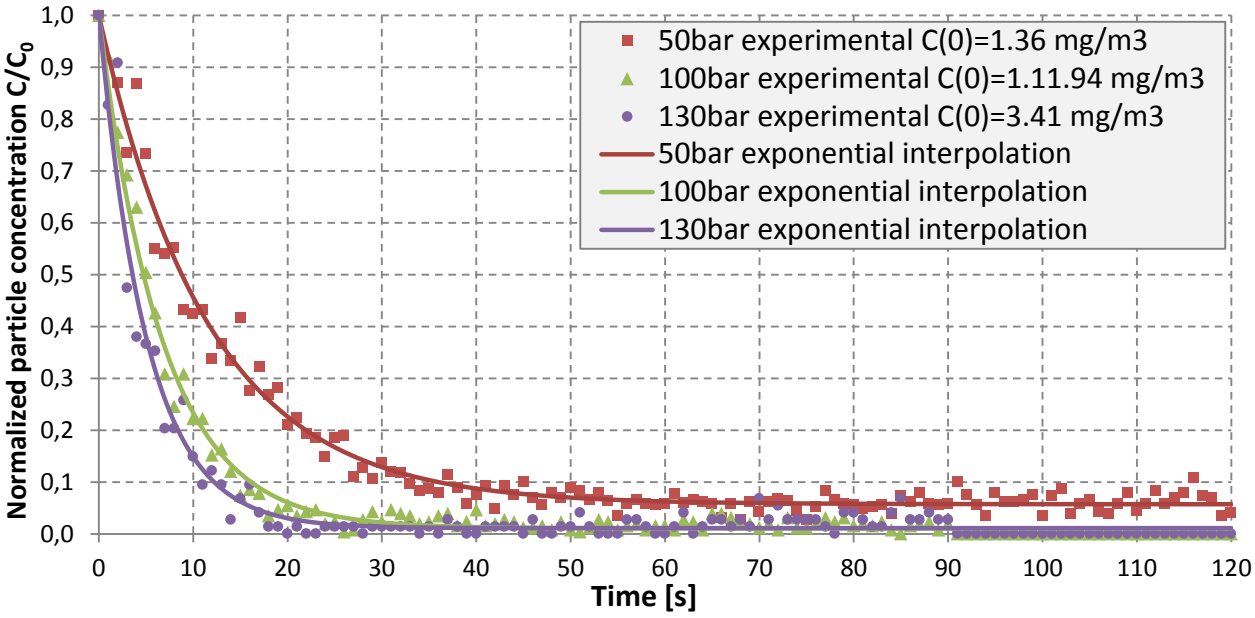

Figure 33: Decontamination curves for low initial particle concentration, 2µm powder

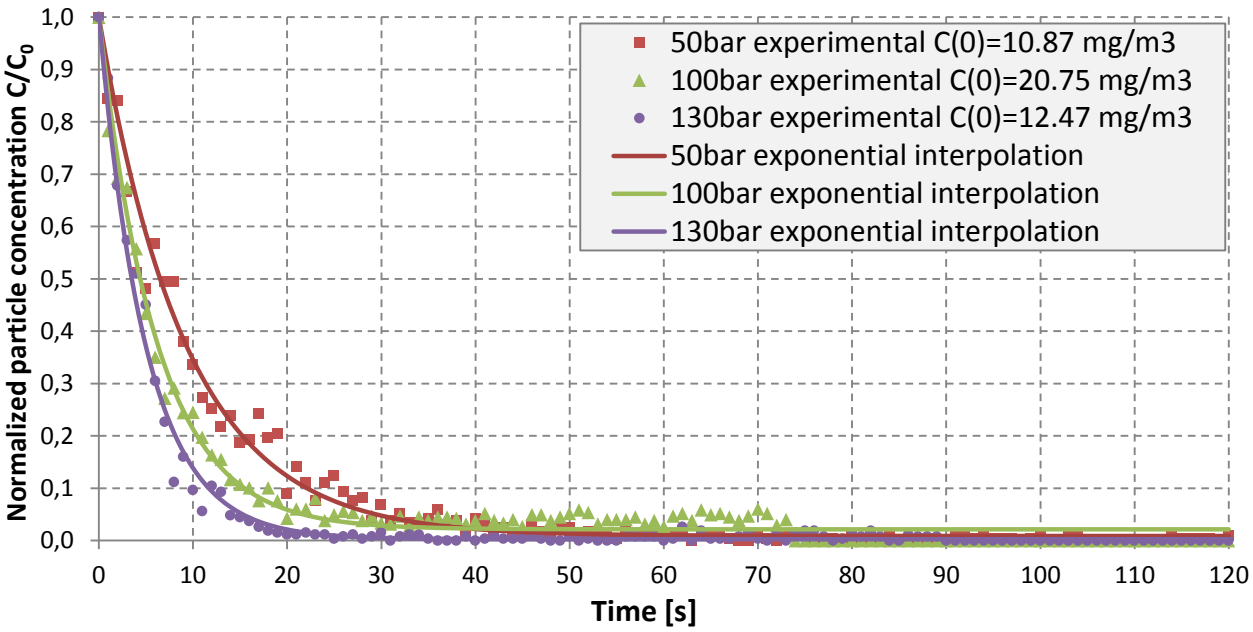

Figure 34: Decontamination curves for medium initial particle concentration, 2µm powder

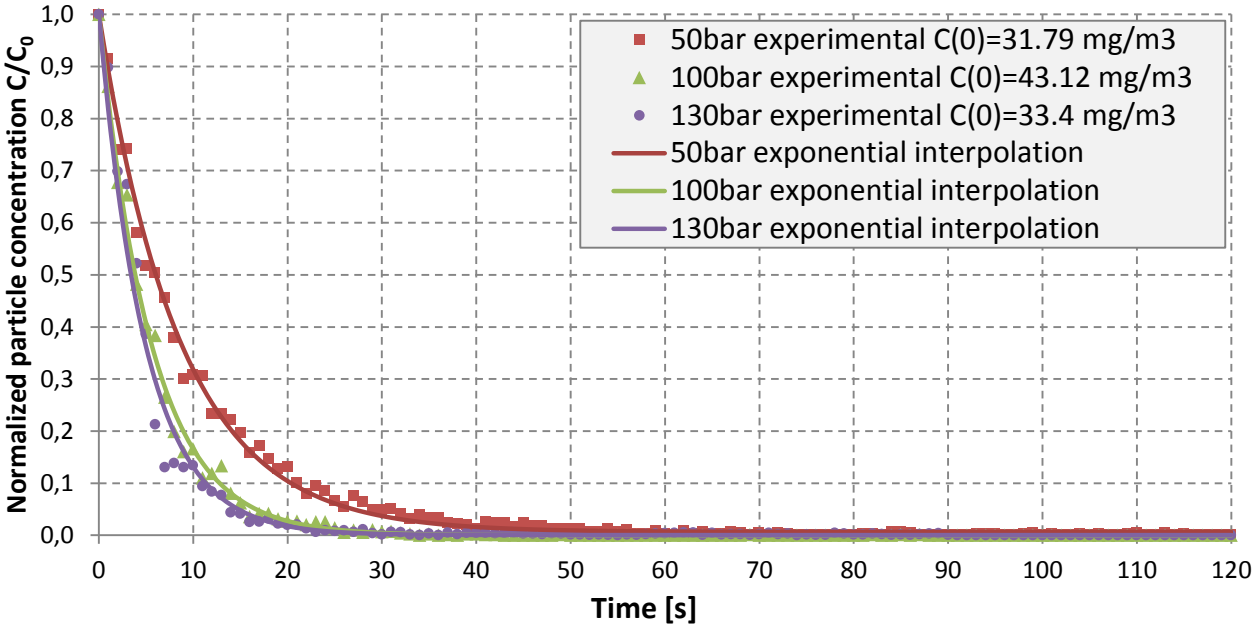

Figure 35: Decontamination curves for high initial particle concentration, 2µm powder

Table 4: values of decontamination factor for 2µm particles

P [bar]	$\overline{\lambda}$ [1/s] Low concentration	$\overline{\lambda}$ [1/s] Medium concentration	$\overline{\lambda}$ [1/s] High concentration	$\overline{\lambda}$ [1/s] Total	Half-Life
50	0,086	0,109	0,116	0,103 ± 0,011	6,7
100	0,167	0,168	0,183	0,173 ± 0,011	4,0
130	0,198	0,162	0,203	0,201 ± 0,021	3,7

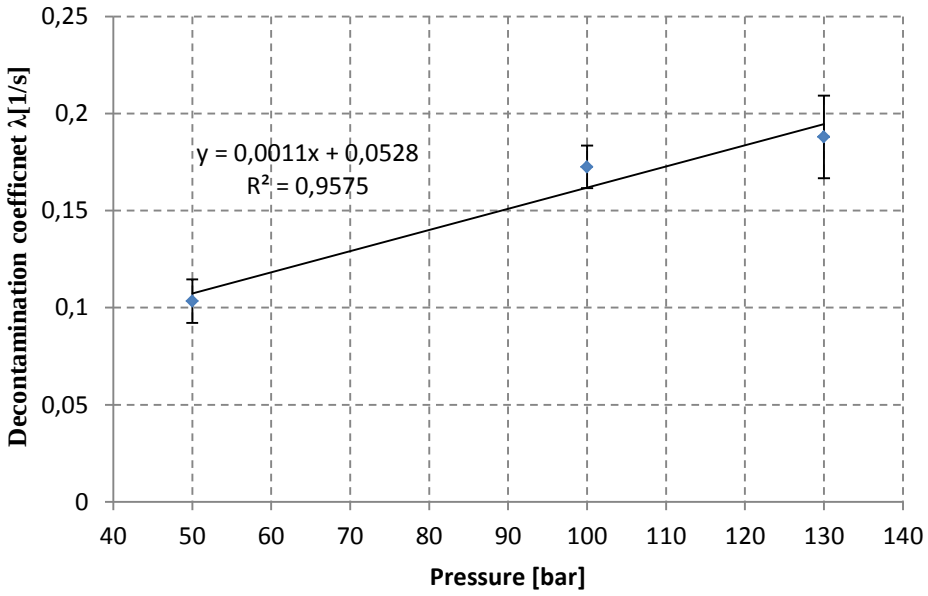

Figure 36: decontamination factor as function of water pressure for 2µm particles

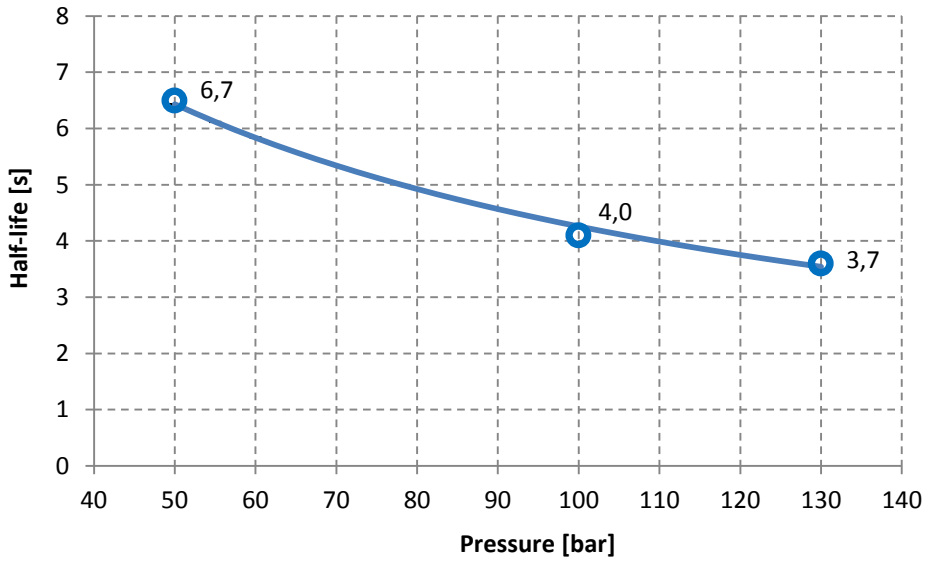

Figure 37: half-life time for 2µm particles, experimental data and interpolation

2.4.3 1 µm powder

This powder showed the same behaviour of the previous ones, so only a summary table on the decontamination factor will be shown.

Table 5: values of decontamination factor for 1µm particles

P [bar]	$\overline{\lambda}$ [1/s] Low concentration	$\overline{\lambda}$ [1/s] Medium concentration	$\overline{\lambda}$ [1/s] High concentration	$\overline{\lambda}$ [1/s] Total	Half-Life
50	0,039	0,044	0,043	0,042± 0,002	16,5
100	0,088	0,084	0,079	0,084 ± 0,003	8,3
130	0,124	0,120	0,116	0,120 ± 0,003	5,8

2.4.4 Powders comparison

As conclusion the three different powder used are compared. The slope of the fitted lines tend to increase with the particle dimension resulting in faster decontamination process as the powder dimension increases. This can be explained as the collision efficiency between droplets and particulate matters is mainly influenced by the inertia of the latter. The particle of 0.5µm will have almost negligible inertia so as the droplets approach, their boundary layer will deviate the particulate trajectory and prevent the streamlines to cross their path and successfully generate a collision that will lead to particle capture.

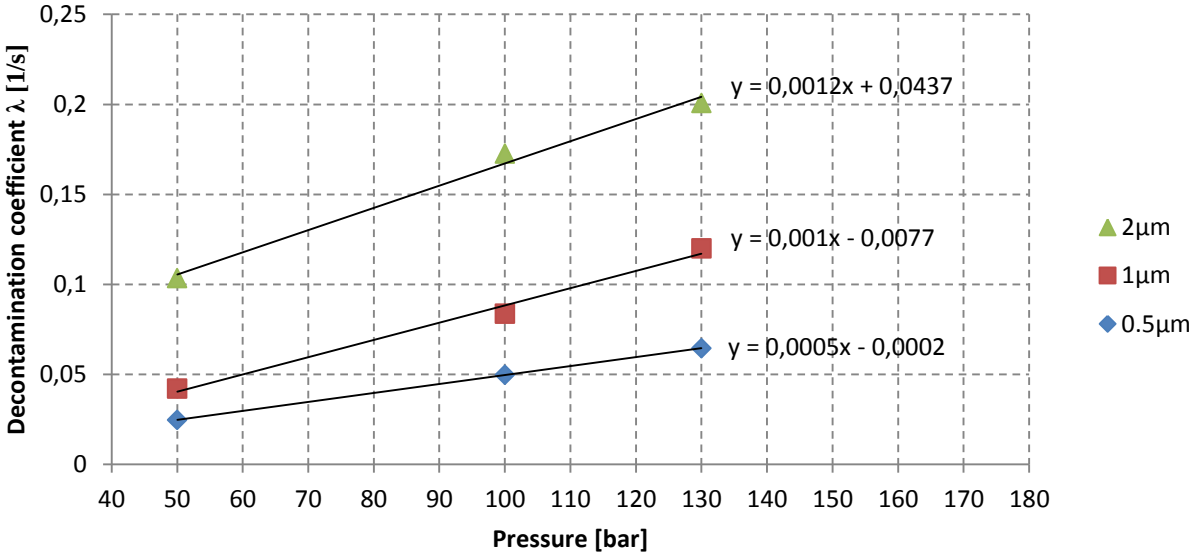

Figure 38: decontamination coefficient as function of water pressure and particle size

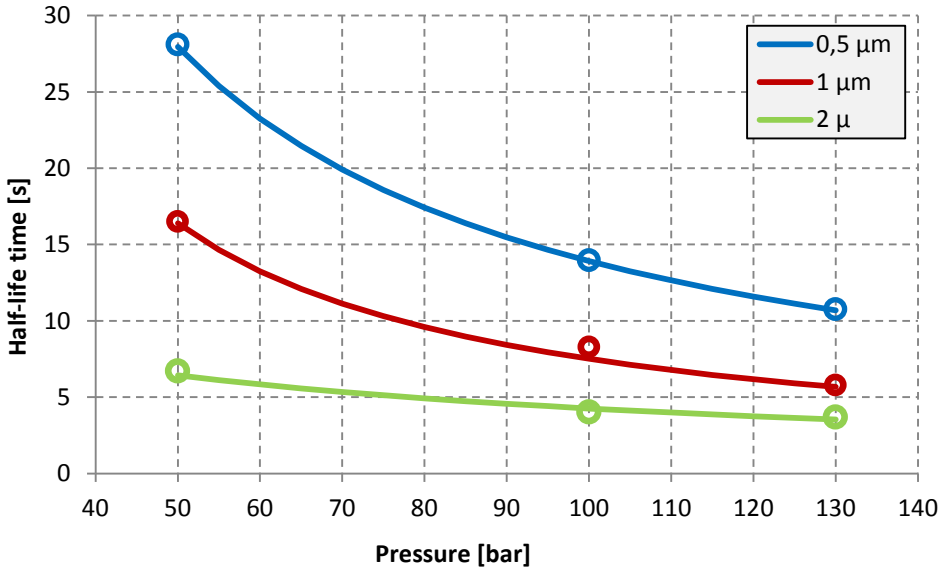

Figure 39: half-life time as function of water pressure and particle size, experimental data and interpolations

3 Spray measurement

This chapter report the analysis of the experimental activity, developed in collaboration with CNR-ICMATE (previously CNR-IENI), that have the aim to collect data on the size distribution and velocity of the spray droplet generated by the nozzle used, in order to gain both input and comparison data for our modeling activity.

3.1 Introduction

The aim of this experimental activity is to obtain the size distribution and velocity of the droplets to be used and to validate the model output.
To achieve that we used a non-invasive measurement method called Phase Doppler Anemometry (PDA) that uses the properties of coherence and polarisation of two crossing laser beams to measure the velocity and the size of the water droplet passing through it.
Measurements are carried out with the spray axis oriented vertically downwards, along 5 cross patterns traversing diametrically the spray, located perpendicular to the spray axis at the axial distance of 50, 100, 250, 500 and 750 millimetres respectively. The water pressure was continuously monitored, the mass flow rate was measured once for each test pressure.

3.2 Experimental Set-up

3.2.1 Water Nozzle

The water spray is generated by the B070 injector of CJX series, that is produced by PNR Italia S.r.l.. This nozzle consists of one central injector and six peripheral ones. The tests have been performed with only the central injector, the lateral injectors have been closed to avoid the effects due to the spray interactions. It is characterised by an orifice diameter of 0.49 millimeters, as shown in Figure 40, and a flow number of 1.95 10^{-6} m^3 s^{-1} $bar^{-0.5}$, thus providing a volumetric flow rate of 1.95 10^{-5} m^3 s^{-1} at the water pressure of 100 bar (Santangelo, 2012). The nozzle has been provided by Bettati Antincendio S.r.l.

3.2.2 High pressure pump

Filtered tap-water at ambient pressure is pressurized by a volumetric pump produced by SIMM Engineering whose specifics are reported in the next table. The water pressure was monitored by three manometers, one installed close to the pump, the other two before the nozzle. The water temperature was not monitored.

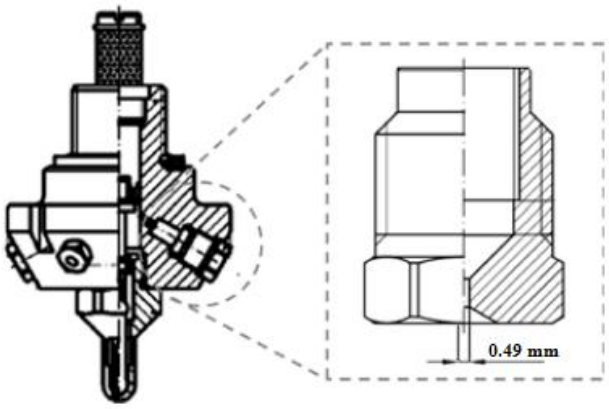

Figure 40: Technical sketch of the employed nozzle

Table 6: High Pressure Pump specifications

Model code	M062
Electric motor	400 V / Ph 3 / 50 Hz / 8A / 3kW
Pressure Min / Max / Permissible	30 bar / 200 bar /220 bar
Flow rate Max / min	420 L/h / 360 L/h
Max inlet temperature	70°C

3.2.3 Phase Doppler Anemometer

The PDA used is produced by Dantec Dynamics and consist of two different optics, a transmitter and a receiver, plus electronic components to acquire and analyse the signal.
The transmitting optic converges two different laser beams in a single spot, where the measure occurs, the refracted and reflected lights are captured by the receiving optic and sent to the analyser.

Table 7: PDA specifics

Transmitting optic	
Laser wavelength	514 nm (green)
Laser power	400 mW
Laser beam frequency shift	40 MHz
Laser beam diameter at the front lens	1.3 mm
Beams distance at the front lens	38 mm
Transmitting lens focal length	600 mm
Nominal measurement volume dimension (ellipsoid)	291x291x9200 microns
Fringe spacing	8.13 μm
Receiving optic	
Scattering angle (receiving optic position)	70°
Receiving lens focal length	600 mm

Sensors aperture	2 mm (maximum)
Water refractive index	1.334
Diameter range	0 – 299 μm
Spherical validation limits	± 10%
Electronics settings	
Processor	Dantec BSA P80
Software	BSA Flow software 2.1.2
Velocity range	-22.8 ÷160 m/s
PMT high voltage	970-1000 volts
Signal gain	28 dB
Burst detection SNR level, level validation ratio	0 dB, level 8:1

3.2.4 Configuration and measurement pattern

The water spray nozzle is mounted at a height of 1 meter and its axis (vertical, downward directed) is referred to as Z, on an orthogonal coordinate system XYZ centred with the nozzle orifice as the origin of its coordinate system.

The PDA transmitting and receiving optics were mounted on a traverse system that allows the measurement point to be moved freely in the three dimensions.

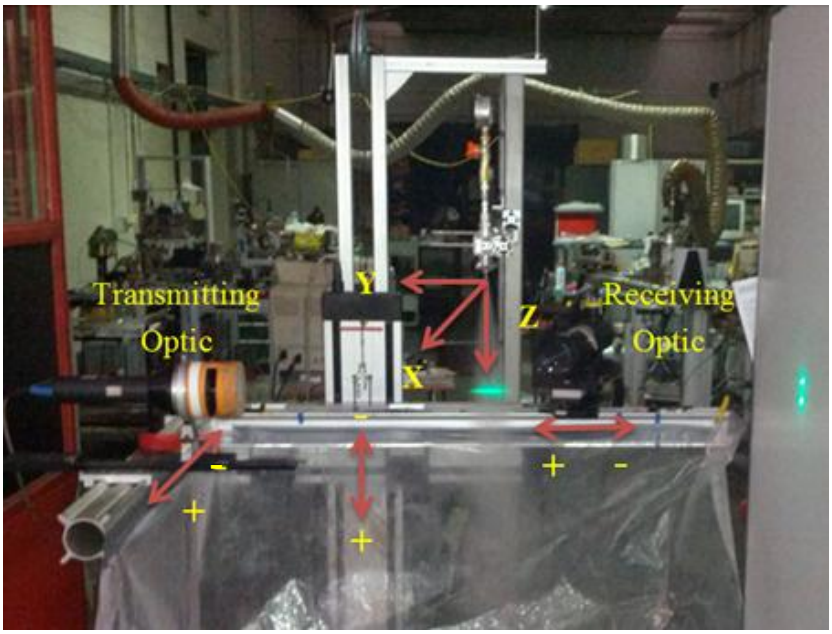

Figure 41: PDA set-up

The PDA traverse Z axis is accurately centred on the spray axis by checking its symmetry with a preliminary measurement set. The alignment may change slightly during the measurements due to the possibility of very small changes in the spray orientation at different water pressures, and the possible elasticity of the whole support system.

The PDA measurement grid in the spray consists of five crosses at five different Z; each cross is composed by 26 positions, disposed along two perpendicular diameters of the spray, 13 positions along X and 13 along Y, the central position being acquired twice.

Table 8: PDA measurement grid

Z position [mm]	X and Y limits [mm]	Space step [mm]	Acquisition points	Acquisition time [s]
50	-15 to 15	2.5	26	5
100	-30 to 30	5	26	5
250	-60 to 60	10	26	10
500	-90 to 90	15	26	20
750	-120 to 120	20	26	20

At each point of the measurement grids, droplets are measured for a fixed amount of time that is constant at the same Z. The whole grid is repeated for each water pressure.
The acquisition time at each position increase with larger Z coordinate, to account for the spray dilution resulting in lower droplet density and lower velocity, both reducing the data rate, which is the number of droplets detected per second, to acquire a sufficient and similar number of droplet, for better statistical analysis, at each Z distance. In average 20’000 droplet are acquired at each position, ranging from 60’000 in the central regions that are denser, up to few hundreds on the spray periphery that is more diluted.

3.3 Phase Doppler Anemometry (PDA)

To fully understand the results and its processing it’s useful to understand the measurement mechanics.

3.3.1 Principles

The underlying principle of PDA is based on light-scattering interferometry and therefore requires no calibration. The measurements are performed at the intersection of two monochromatic and polarized laser beams, generated by splitting a single beam to ensure coherence, which defines the measurement volume MV. The measurements are performed on single particles as they move through the sample volume. Particles thereby scatter light from both laser beams, generating an optical interference pattern.
The receiving optics projects a portion of the scattered light onto multiple detectors. Each detector converts the optical signal into a Doppler burst with a frequency linearly proportional to the particle velocity. The phase shift between the Doppler signals from different detectors is a direct measure of the particle diameter.

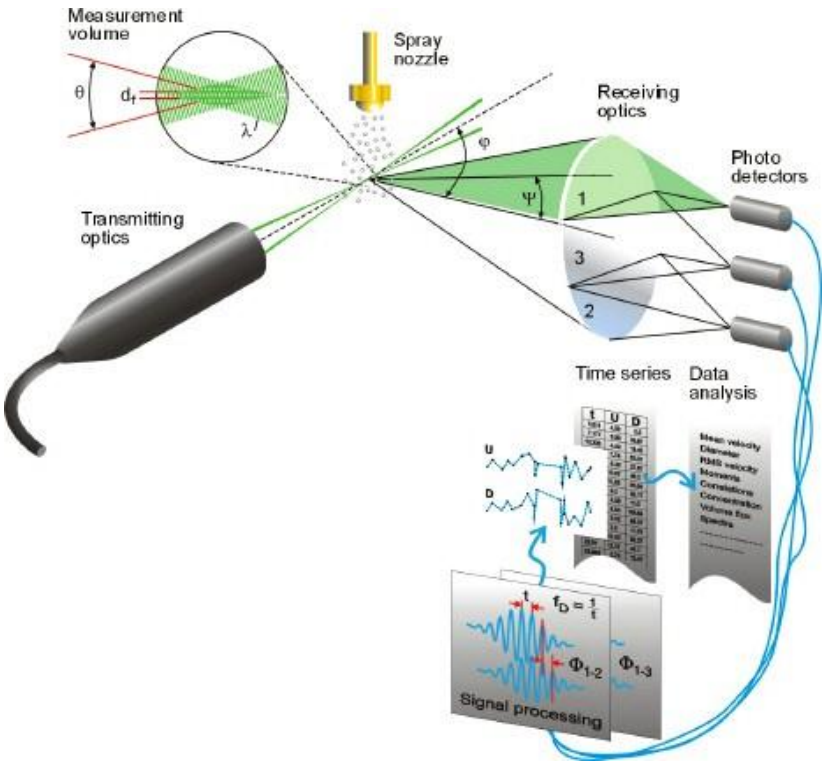

Figure 42: PDA measure principles

The measurement volume is shaped like an ellipsoid, whose diameter is function of the light intensity, cut by the projection of a vertical slit, so that only the central part of the MV is seen by the receiving optic where the signals are stronger, and thus reducing also the probability that two particles are detected at the same time, which would invalidate the measure.
The problem is that the larger particles are more easily detected, which leads to a bias error in the average results.

3.3.2 Bias correction

The procedure to correct the bias in PDA measurements is known as Saffman correction (M. Saffman, P. Buchhave, and H. Tanger, 1984). Each droplet that crosses the laser intersection will generate a different dimension measurement volume proportional to the droplet size. The MV dimension is considered proportional to the probability of a droplet to be detected by the instrument. The value of MV(D) can be extracted by data post-processing, and the factor 1/MV can be used as a weight to correct the averages from the bias.
This weight is calculated once for all measures as follows.
The output of the measure is formed by a set of three values: transit time (TT), velocity (LDA) and diameter (D) of each droplets. The product of TT*LDA is the value of the droplet trajectory intercepted by measurement volume ellipsoid; for droplets having the same diameter, its maximum value is ideally the ellipsoids vertical diameter length, which is proportional to the value of the measurement volume for that class of droplet diameter.
The value of the weight is calculated from the curve that strictly subtends the region with all the MV values in a graph of measurement volume versus droplet diameter.

The weight is calculated as the ratio between a reference diameter and the measured diameter elevated to an empirical exponent which value is found to be 0,3.

$$Weight = \left(\frac{D_{ref}}{D_d}\right)^{0.3} \qquad 3.1$$

The reference diameter is the higher dimension of the measured droplet that is not affected by the bias error, which in our optical configuration is 10µm.

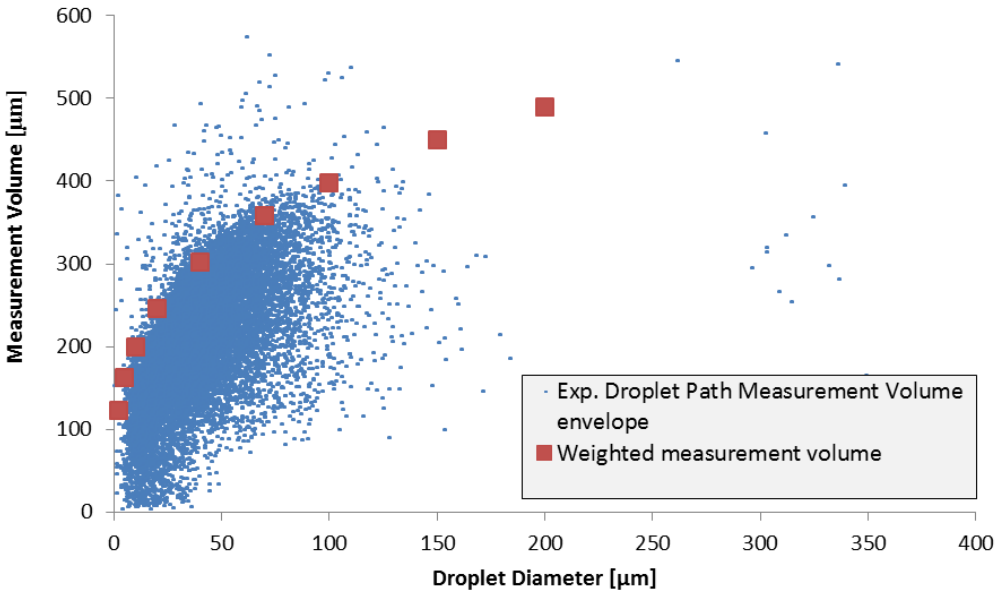

Figure 43: Weight calculation to correct the PDA bias

This weight is a statistical correction that modifies the number of bigger droplets seen. For example a droplets whose measure is 150µm has to be seen as 0,4438 droplets of 150µm.
As result the population histogram of a single measure will looks like:

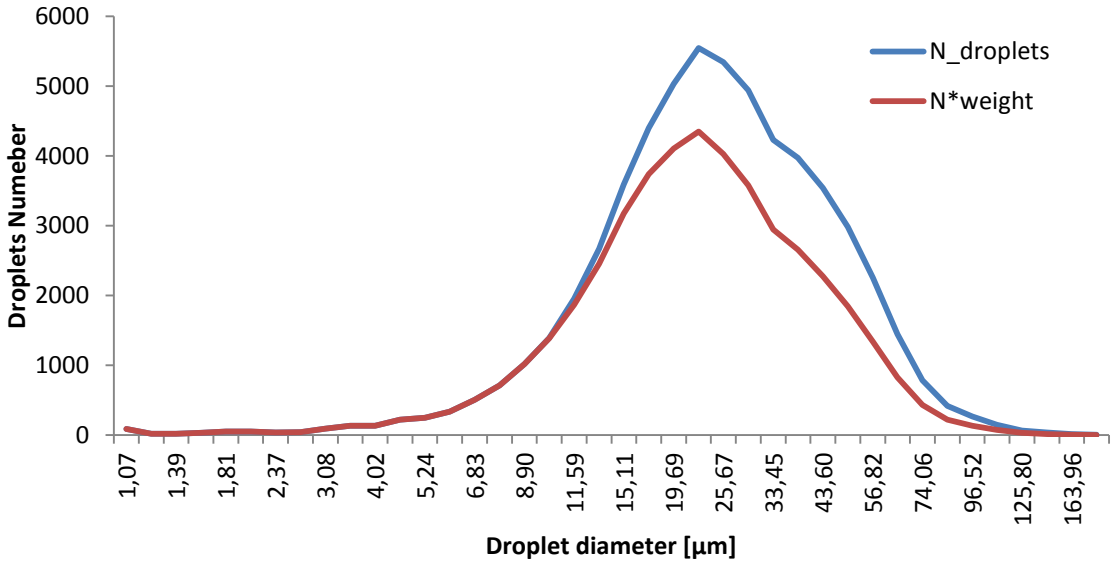

Figure 44: PDA bias free histogram

The mean diameter has to be corrected as follows:

$$\overline{D}_{weighted} = \frac{\sum D_i * weight_i}{\sum weight_i} \quad 3.2$$

3.4 Data processing and analysis

In this chapter the result of the measurement campaign is shown. The results are divided in a progressive manner showing the process that leads from the single point measurements to the value used as input to our modeling activity, passing from the cross-planar total value.

3.4.1 Single point measurements

For each measurement point the PDA will give output information on transit time, axial velocity and diameter for each sampled droplet.
For each measurement point (26 each Z quote, 5 quotes) a histogram is created, as shown in Figure 44: PDA bias free histogram, creating 40 classes, from 1 to 200 μm, with logarithmic amplitude (to get more classes in the small diameter zone) counting the number of droplets in each interval.
For each point the following values are calculated:

- Data Rate: is the value of the number of droplets sampled each second
- Velocity: is the measure of the axial velocity of the droplets, corrected for the PDA bias

$$V_c = \frac{\sum V_i * weight_i}{\sum weight_i} \quad 3.3$$

- Characteristics diameters, each corrected for the PDA bias

$$D_{10} = \frac{\sum D_i * weight_i}{\sum weight_i} \quad 3.4$$

$$D_{20} = \left[\frac{\sum {D_i}^2 * weight_i}{\sum weight_i}\right]^{1/2} \quad 3.5$$

$$D_{30} = \left[\frac{\sum {D_i}^3 * weight_i}{\sum weight_i}\right]^{1/3} \quad 3.6$$

$$D_{32} = \frac{\sum {D_i}^3 * weight_i}{\sum {D_i}^2 * weight_i} \quad 3.7$$

The graph results are shown here, the values are reported in the appendix tables.

3.4.1.1 50 bar

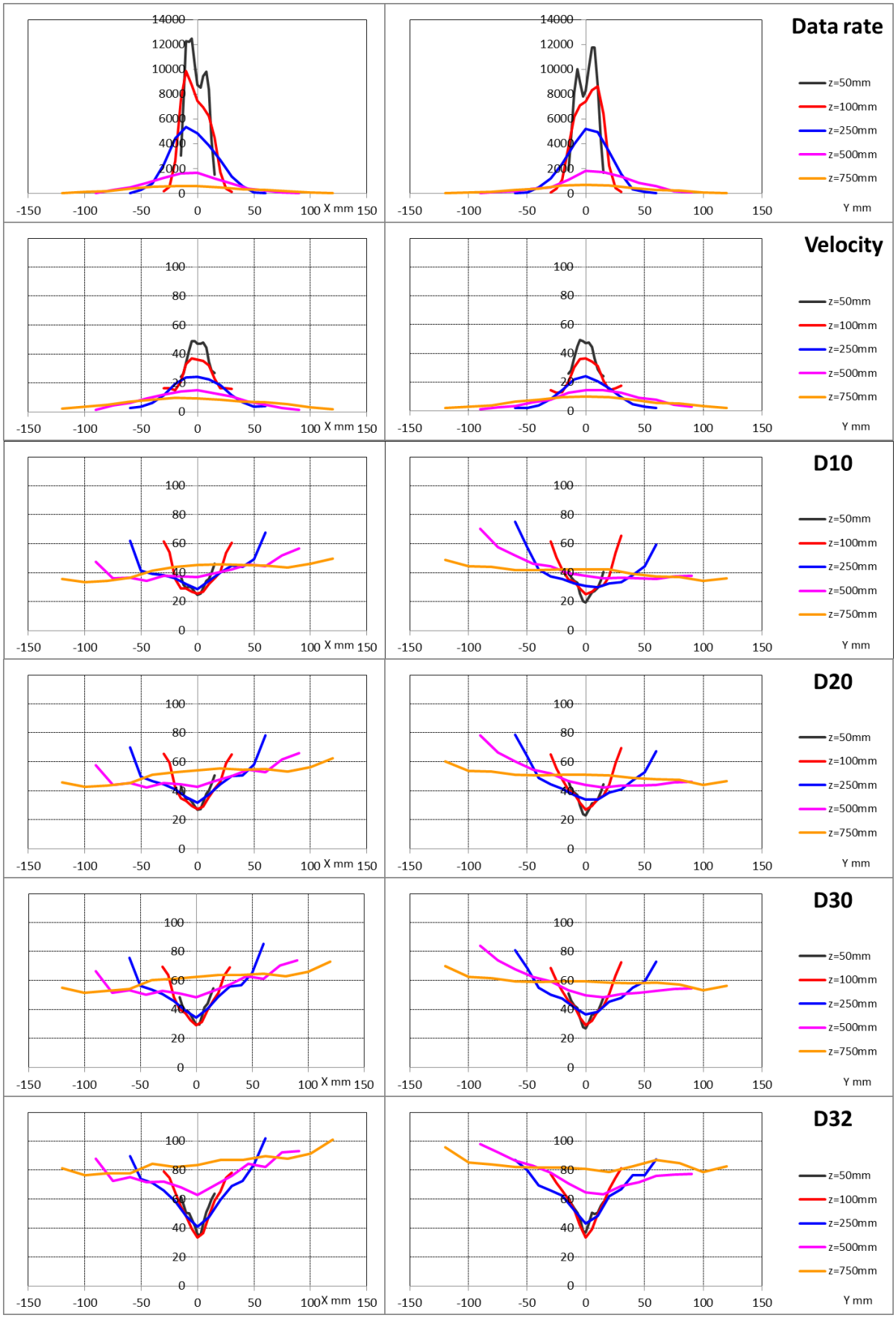

Figure 45: 50bar single point measurements results

3.4.1.2 80 bar

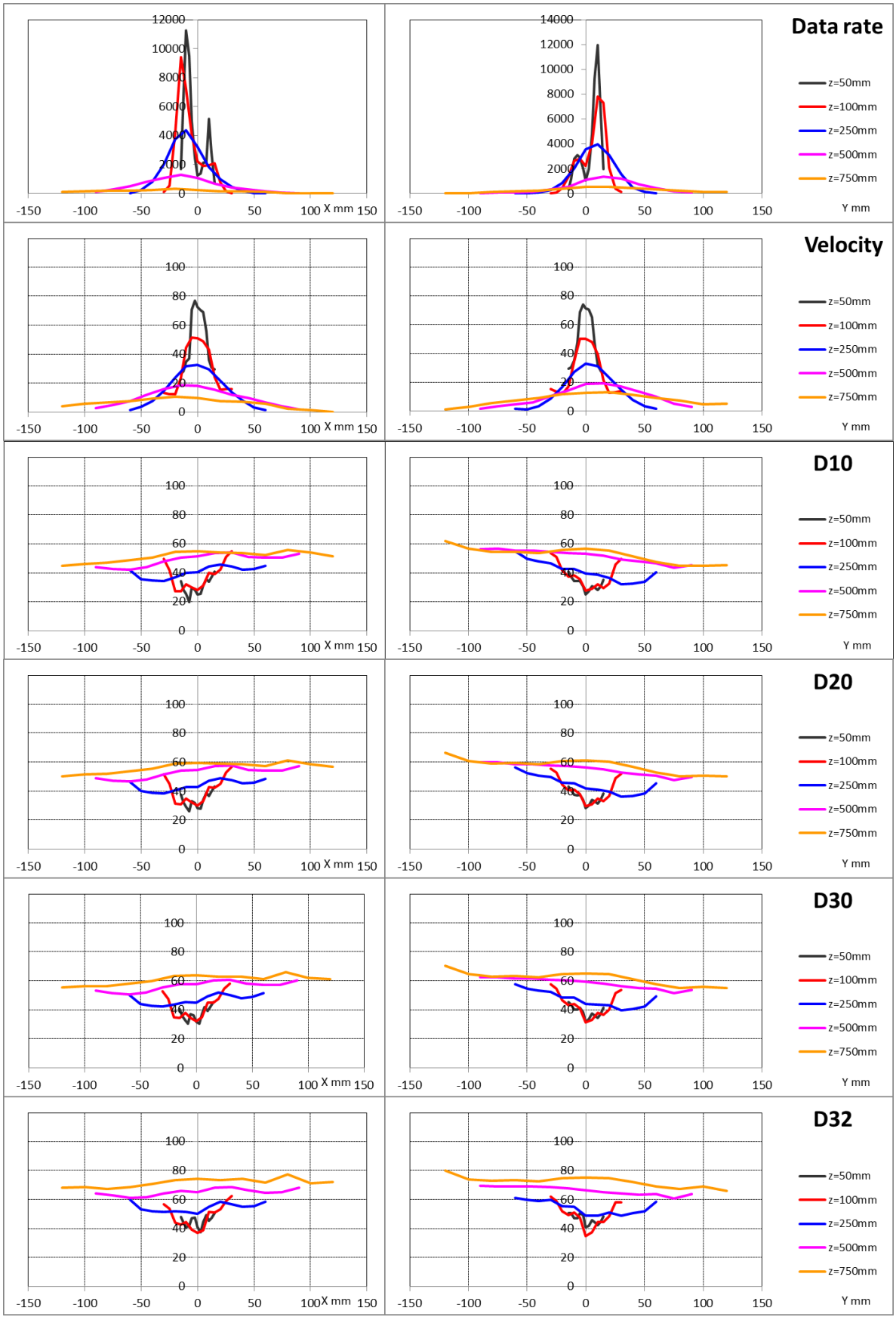

Figure 46: 80bar single point measurements results

3.4.1.3 100 bar

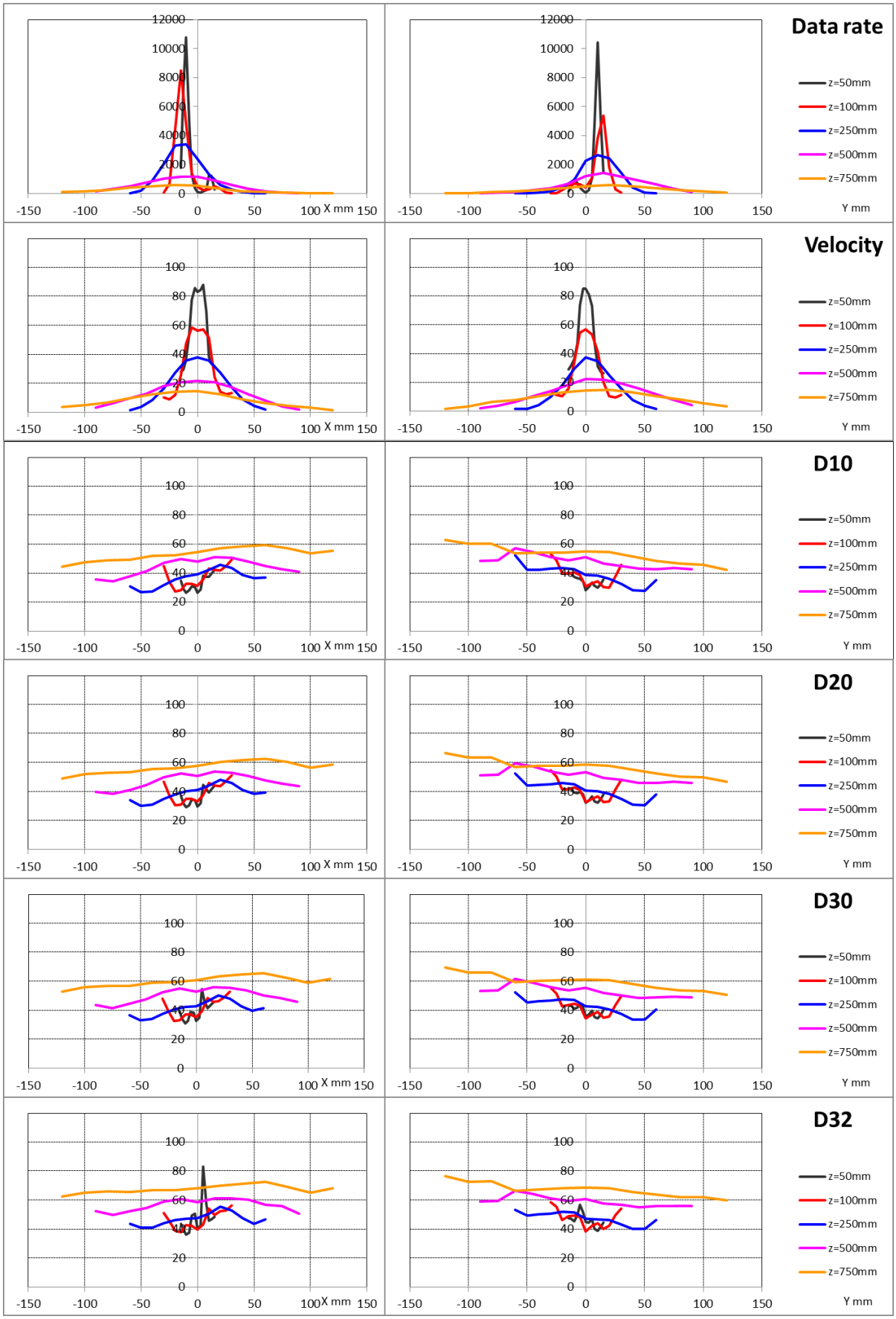

Figure 47: 100bar single point measurements results

3.4.1.4 130 bar

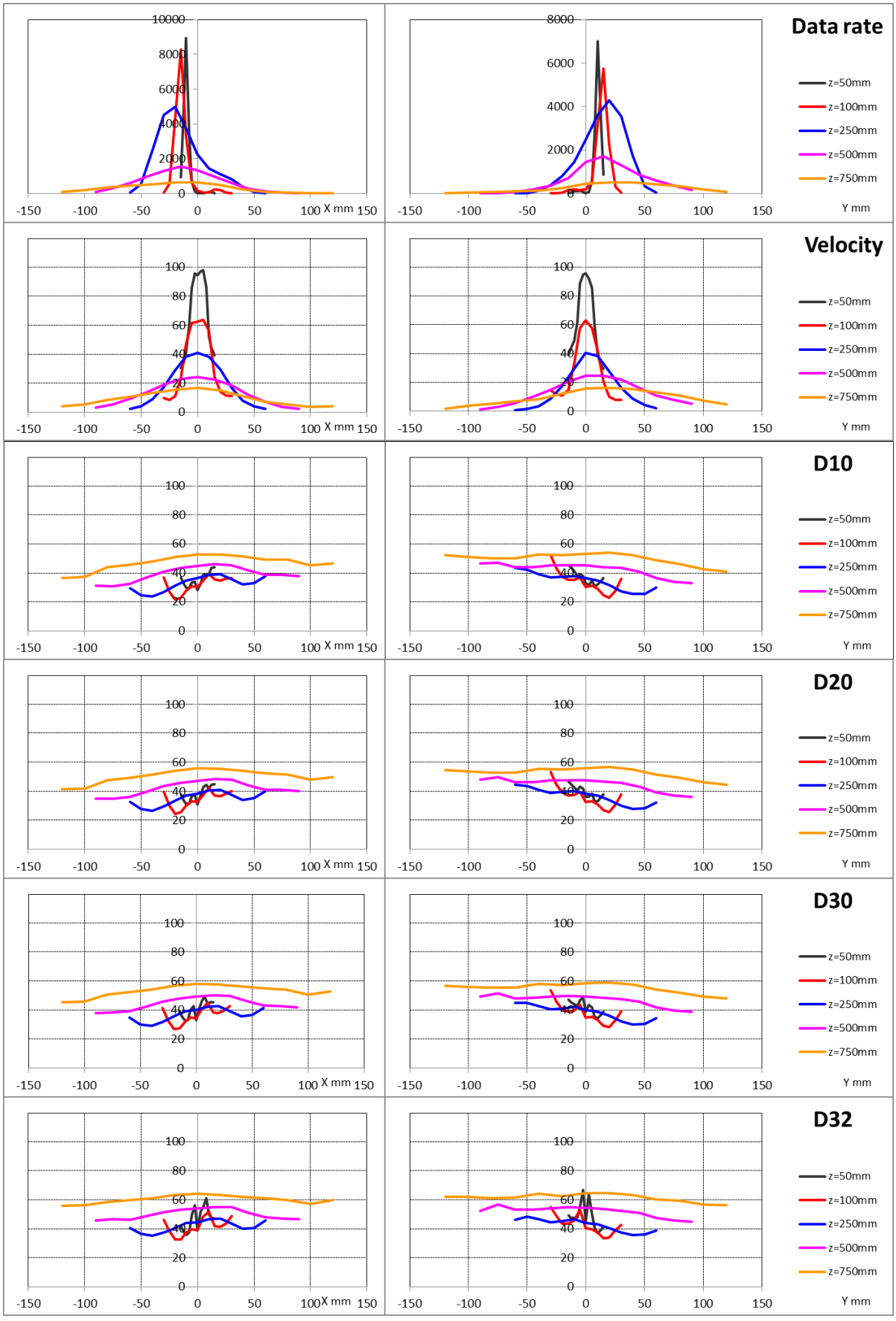

Figure 48: 130bar single point measurements results

The PDA in the denser zone doesn't perform optimally, as it can be seen in both the data rate and in the diameters profiles. The data rate in the near nozzle region (low Z values) shows a maximum shifted towards the positive Y and negative X because it's the zone where the scattered light has to cross less region of the "mist zone" to be captured by the receiving optic. The diameter value will be slightly higher in the negative Y and positive X for the PDA propensity to easily sample the bigger droplets (the scattered light of the bigger droplets has stronger intensity compared the smaller ones and is easily received by the receiving optic).

3.4.2 Cross-planar approach

Since our model splits-up the spray cone in many planar layers, each one perpendicular to the spray axis, it's useful to obtain planar information on our spray.

3.4.2.1 Obtaining the values

It is done by considering a section plane that cuts the spray at each Z quote and dividing it in many circular sectors of amplitude equal to the distance between each measurement point. The measurement point will be considered at the center of the circular sector.

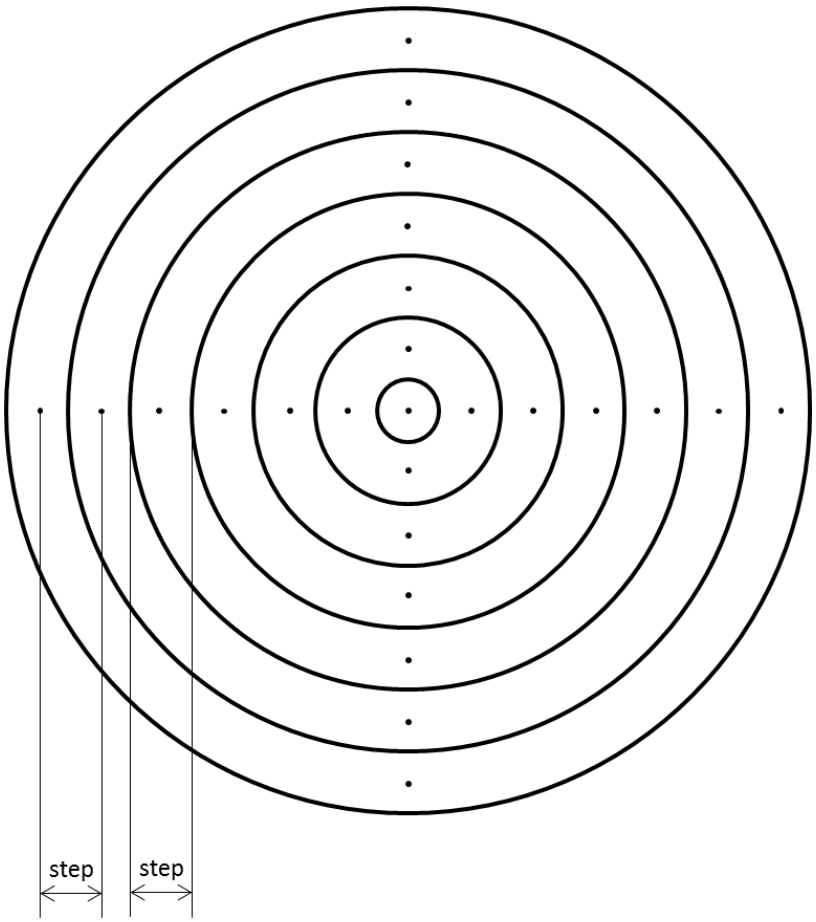

Figure 49: Example of spray planar section, dots are measurement points, solid lines are boundaries of each sector

For each point the number histogram, already bias corrected, is then area weighted considering the circular sector area referred to each point (the center point as half value since it's detected twice, the other points with the same radius are divided by four since they are detected twice on the X and twice on the Y in the same circular sector).
To obtain the area-histogram the number of droplets contained in each interval is then calculated as follow:

$$n_{i\_c\_aw} = \frac{\sum n_i * aw}{\Delta t} \qquad 3.8$$

- $n_{i\_c\_aw}$ is the number of droplet that belongs to the i-th diameter class, corrected for the bias error, area weighted, per unit of time
- n_i is the number of droplets belonging to the i-th diameter class in each measurement point
- aw is the area-weight
    - If the considered point is the center aw is half of the area of the circle with radius equal to half radial step
    - Otherwise aw is the area of a quarter of circular sector whose point refers to
- Δt is the sampling time referred to each point, it changes with Z quote

A rescale work is needed to obtain the real total number of droplets.
The flow rate of each i-th diameter droplet is calculated:

$$\dot{m}_i = n_{i\_c\_aw} * V_i * \rho_{water} \qquad 3.9$$

Where V_i is the volume of the droplets of i-class diameter and ρ_{water}=997 kg/m^3.
Then each value of $n_{i\_c\_aw}$ is multiplied by the value $\frac{\sum \dot{m}_i}{\dot{m}_{real}}$ to obtain the number of droplets that will generate the real mass flow rate.
The final result of this process leads to a diameter distribution shown in the next figure:

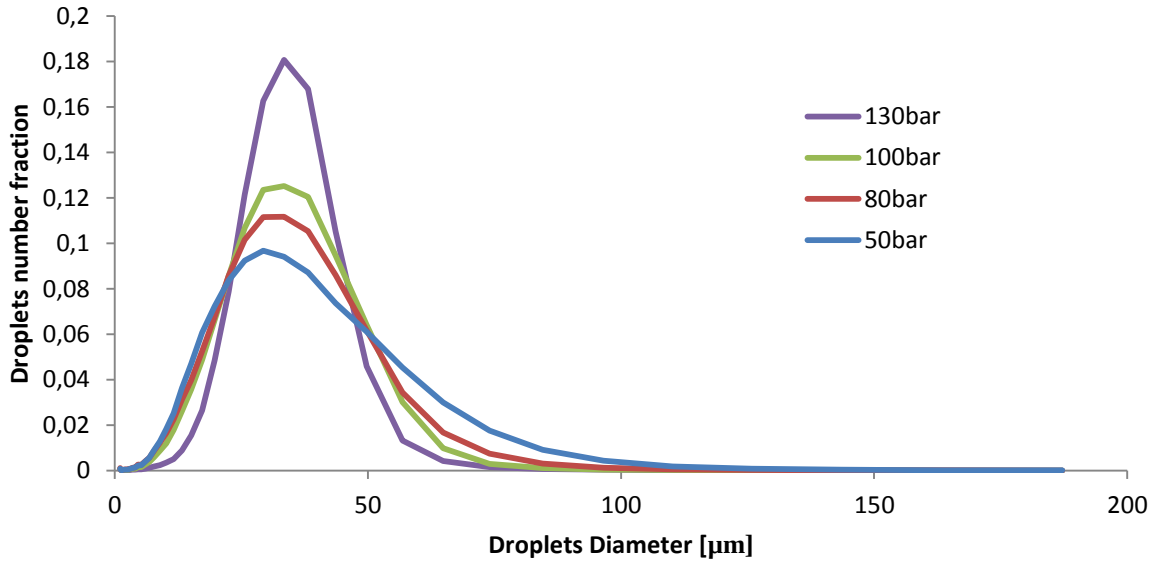

Figure 50: Droplets diameter distribution after the planar averaging process

With increasing pressure the number of the droplets present in the curve tails tend to decrease, leading toward narrower diameter distributions.

3.4.2.2 Total number of droplets

The total number of droplets detected will be shown here as function of the injection pressure and of the distance from the nozzle of the spray

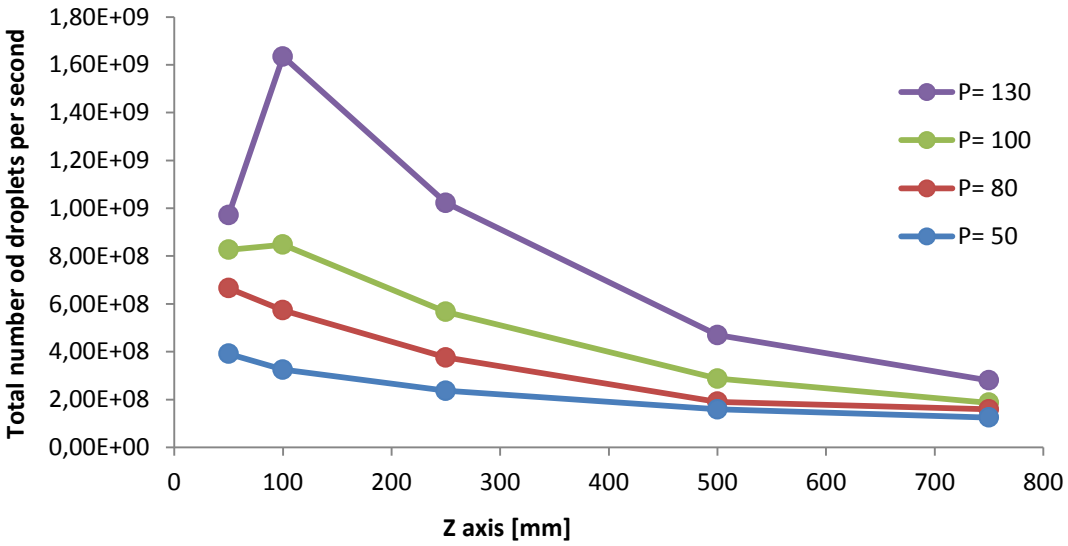

Figure 51: Total number of droplets detected at different Z heights

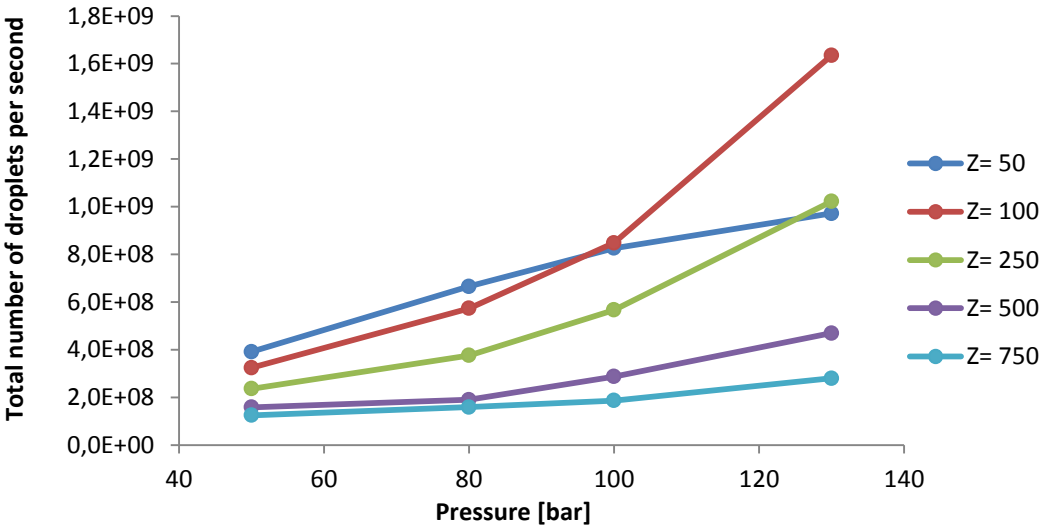

Figure 52: Total number of droplets detected at different pressures

This two graphics show the same information under different prospective, as the total number of droplets increase with increasing pressure, due to the more intense breakup, and decrease with the distance from the nozzle for both agglomerating mechanisms and water evaporation.

The limit of the PDA measurement are shown at high pressures (slightly at 100 bar and clearly at 130 bar) near the nozzle, as in this zone the spray is really dense and the PDA can't sample correctly.

3.4.2.3 Characteristics diameters

As for the number of droplets, the D_{10}, D_{20}, D_{30}, D_{32} will be shown as function of both distance from the nozzle and injection pressure

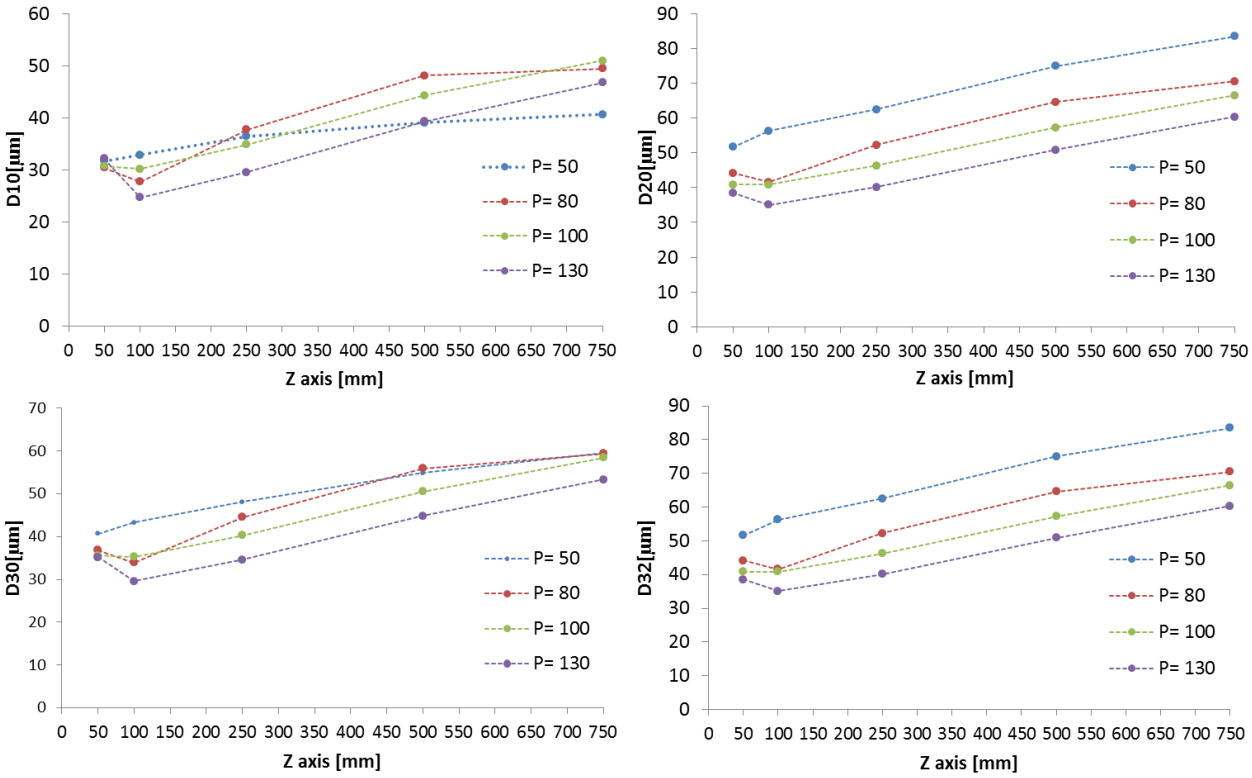

Figure 53: Trend of the characteristics diameters as function of the distance from the nozzle

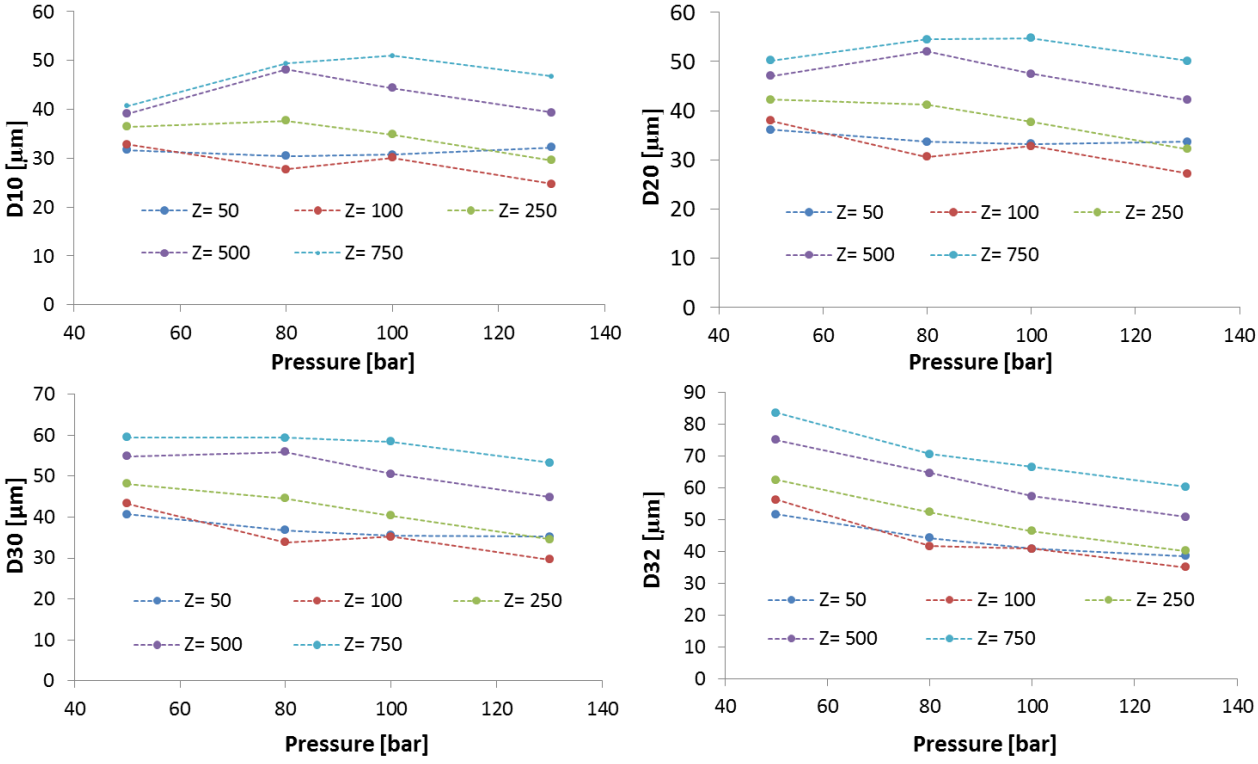

Figure 54: Trend of the characteristics diameters as function of the injection pressure

The average droplet diameters decrease with the injection pressure (especially the D_{32}), as the breakup mechanism is more intense with increasing pressures, and they increase with increasing distance as the droplets coalesce with each other and the smaller ones are more likely to evaporate. The limit of the PDA can be seen at 100 and 130 bar as the average diameter dimension, near the nozzle, is greater than what it should really be since in the dense zone the bigger droplets are more likely to be sampled.

3.4.2.4 Velocities

To obtain the mean droplet velocity for each plane a total average has been made considering all the droplets sampled, in every measurement point, and correct the bias error as follows:

$$V_{tot\_c} = \frac{\sum_{all\ points} V_i * weight_i}{\sum_{all\ points} weight_i} \qquad 3.10$$

Obtaining the following results:

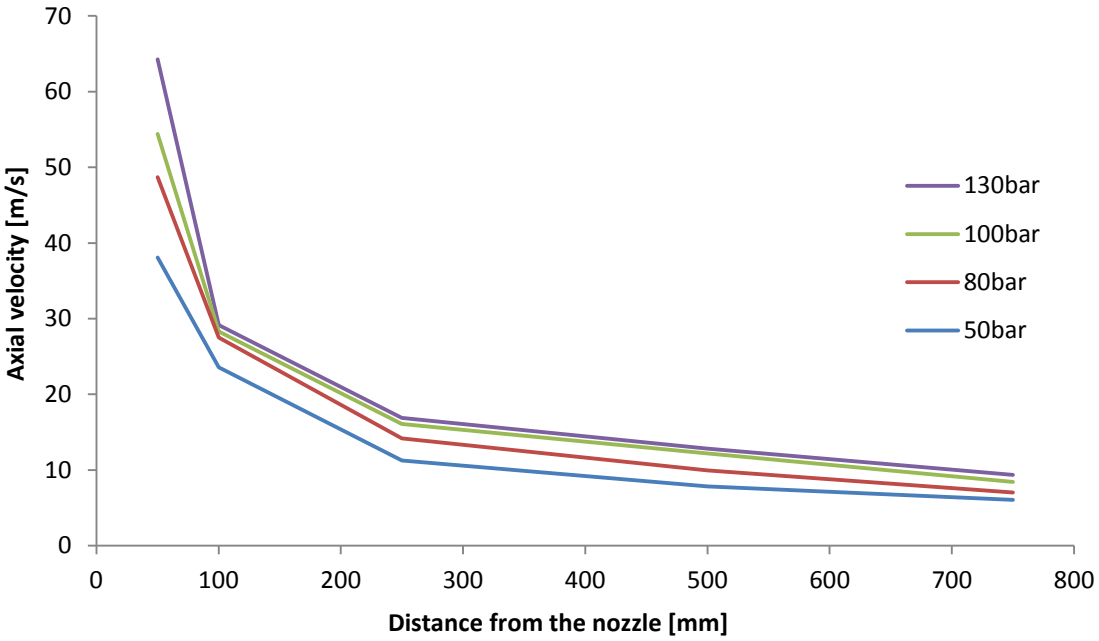

Figure 55: mean droplets velocity

3.4.3 Model input

The data collected at this point can't be used as input for the model because the data relative to 100 and 130 bar at 5 millimiters from the nozzle, as seen in Figure 51, have not the expected trend. The data available in those conditions are sampled in a denser spray cone zone, so the PDA measurements can not be performed optimally and fewer droplets, preferentially those with higher average diameters will be sampled. Correct values for size distribution and velocity need to be founded.

3.4.3.1 Droplets number and size distribution

The first step in finding correct values for number and size distribution of the droplets is to obtain a realistic value for the droplets total number.
It was found that a revisited version of the Nukiyama – Tanasawa distribution correctly interpolate the total number of droplets as function of the water pressure and the distance from the nozzle.

$$N_{tot} = P^m * e^{-(Z/n)} \qquad 3.11$$

Where N_{tot} is the total number of droplets, P the pressure in pascal, Z the distance from the nozzle an m,n parameter that depends on the injection system.
An optimization work has been done on equation 3.11 to find the values of n and m that will lead to the best total number fitting curve for each pressure. The results are shown in the next table.

Pressure [bar]	m	n
50	1,285	0,549
80	1,284	0,408
100	1,290	0,399
130	1,312	0,343

These values are used to calculate the total number of droplets for the pressure of 100 and 130 bar at the first position of 50 mm from the nozzle, leading to values of 955575309 and 1885060201 droplets respectively.

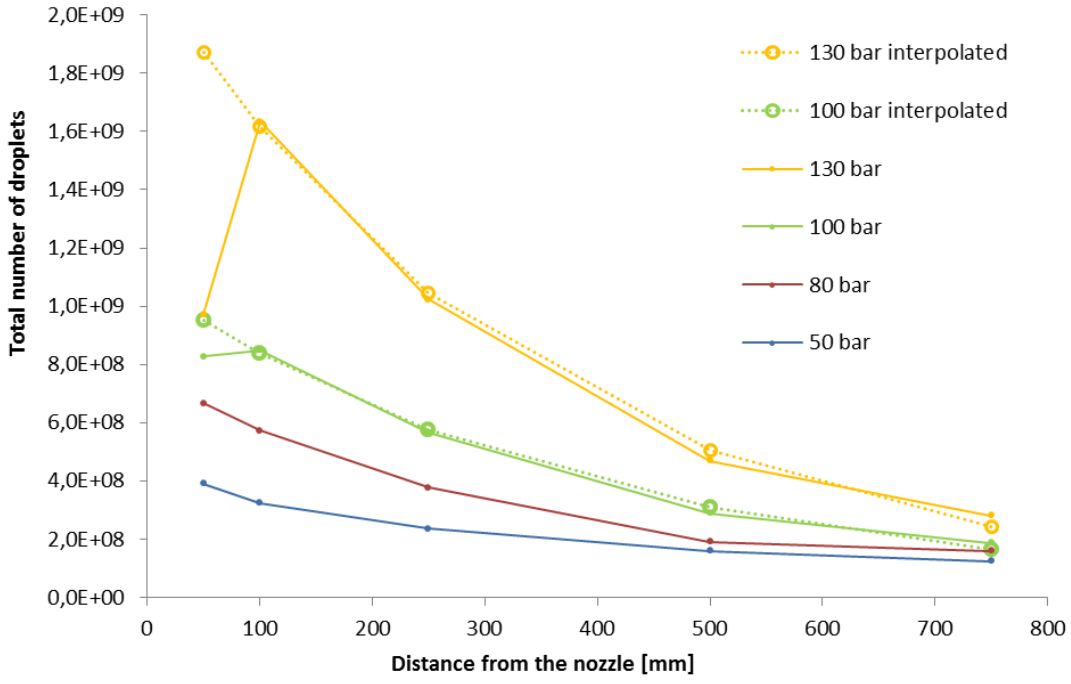

Figure 56: Corrected total number of droplets as function of pressure and distance from the nozzle

The second step is to obtain the correct size distribution of this total number of droplets. It has been done finding the best log-normal curve that approximates the fraction of droplets obtained in the cross-planar section present in each diameter class.

The fraction of droplets in each class were calculated in 3.4.2.1 and illustrated in Figure 50 as follows:

$$Fraction_{i-th} = \frac{n_{i\_c\_aw}}{\sum n_{i\_c\_aw}} \qquad 3.12$$

The log-normal interpolating function used is:

$$f(d) = a * e^{-\frac{-ln(D_d - \bar{D}_d)^2}{2\sigma^2}} \qquad 3.13$$

Where:

- $f(d)$ is the probability to find a droplets of diameter D_d
- a is a parameter used to adjust the unit of measure and include the term $\frac{1}{\sigma\sqrt{2\pi}}$
- $\bar{D}_d$ is the diameter average value of the distribution
- σ is the standard deviation in the logarithmic scale

An optimization work on has been done on those variables, minimizing the difference between the experimental fraction of droplets and the calculated one, imposing that the resulting droplets distribution would generate the total mass flow rate of water flowing through the nozzle.

This process leads to the following distribution for the number of droplets used as input for the model:

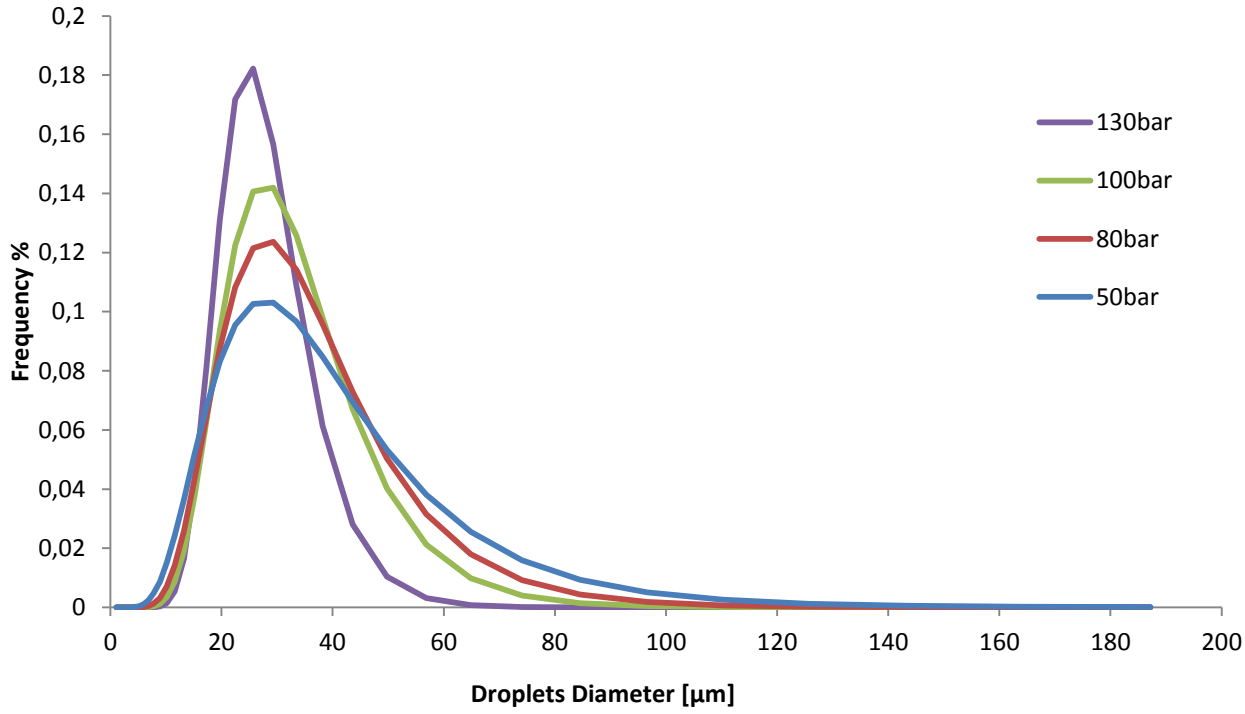

Figure 57: Droplets distribution used as input for the model

The following values for the average diameter of the resulting distribution and standard deviation have been found:

Table 9: parameter of the droplet size distribution at 50 mm from the nozzle

P [bar]	$\overline{D}_d$	σ_{log}	σ_{geo}
50	27,64	0,51	1,66
80	28,10	0,43	1,53
100	27,68	0,37	1,44
130	24,93	0,29	1,33

The distribution of the 130 bar is the one that has been more modified by this process because the values obtained from the PDA results were biased to higher droplets diameter and coulden't generate the correct flow rate with that distribution.

3.4.3.2 Droplets velocity

The model takes as input the velocity of each diameter class. To obtain it the average value of speed for each droplets class had been calculated bias corrected, area and number weighted as follows:

$$V_{i\_c\_anw} = \frac{\sum V_i * A_i * weight_i * n_i}{\sum A_i * weight_i * n_i} \qquad 3.14$$

Where:

- V_i is the velocity of the droplet belonging to the i-th diameter class
- A_i is the area referred to the measurement as shown in equation$n_{i_c_aw} = \frac{\sum n_i * aw}{\Delta t}$ 3.8
- $weight_i$ is the bias correction factor as calculated in paragraph 3.3.2
- n_i is the total number of droplets present in the i-th class diameter

The results are shown in Figure 58.

It can be seen that all the curves have a common trend, the smaller droplet rapidly move to a minimum velocity and after that point the velocity of every droplet size range increases asymptotically toward larger velocity, with its maximum value increasing with the water injection pressure.

As for the number distribution, the value obtained for 130 bar shows a trend that differs from the other pressure, in particular the velocity shows inconsistent trend for very large droplets. This is probably due to the lack of large droplets at high pressure so it is normal that average results present larger dispersion. In order to obtain a uniform trend a correlation between the bernoullian injection velocity and the velocity of each diameter size class making use of the data available for 50, 80 and 100 bar to obtain an empirical correlation.

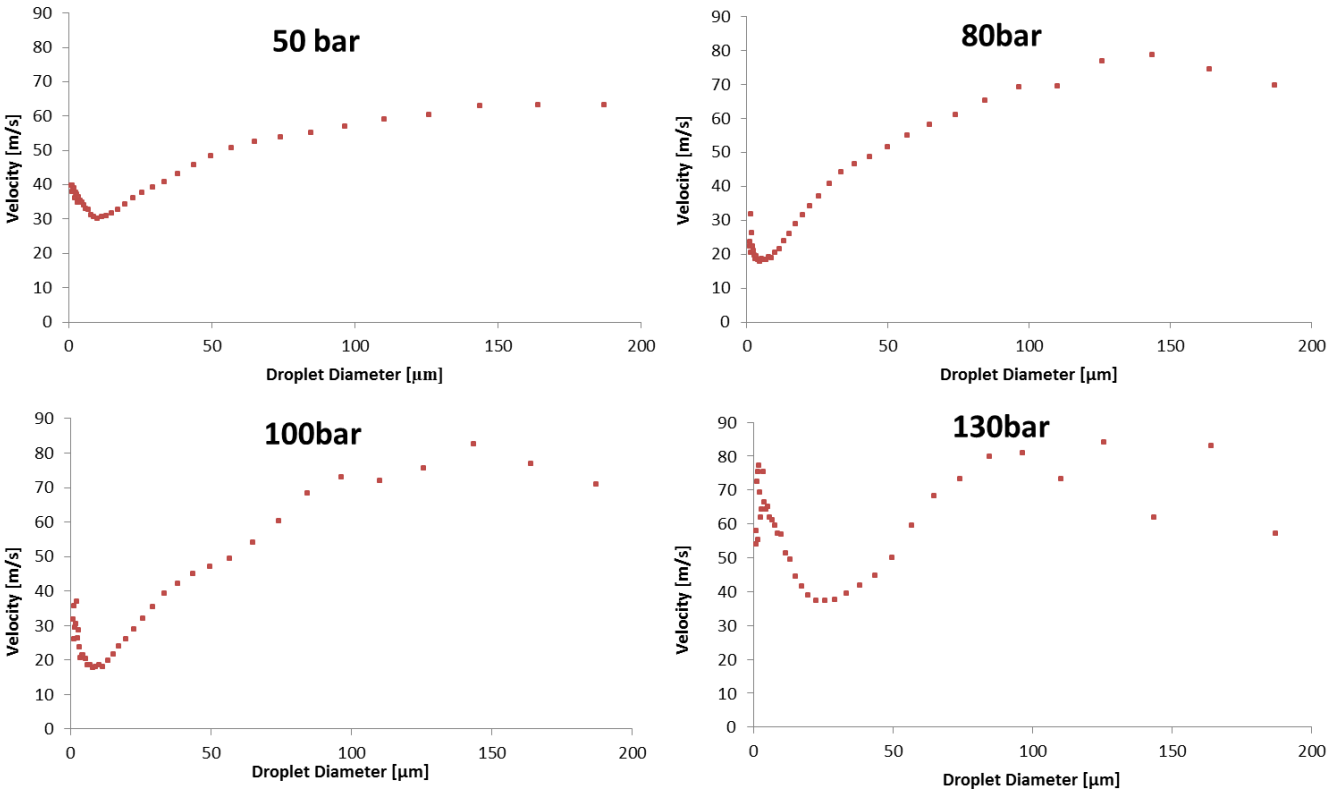

Figure 58: Average velocity of each droplets class

The bernoullian velocity is calculated in the following way:

$$V_b = \sqrt{\frac{2P_{injection}}{\rho}} \qquad 3.15$$

The velocity of each droplet size range is calculated as follows:

$$V_{i\_input} = \frac{\sum_i \bar{V}_{i\_c\_anw}}{\bar{V}_b} * V_{b_j} \qquad 3.16$$

Where the terms under the average symbol are calculated with the data available at 50, 80 and 100 bar and the meaning of the other terms are:

- i represent the droplet size range;
- $\bar{V}_{i\_c\_anw}$ is the experimental average value of velocity for the i-th droplet size area and number weighted;
- $\bar{V}_b$ is the average value of bernoullian velocity ;
- V_{b_j} is the imposed bernoullian velocity at j-th pressure;

The obtained results are shown in Figure 59.

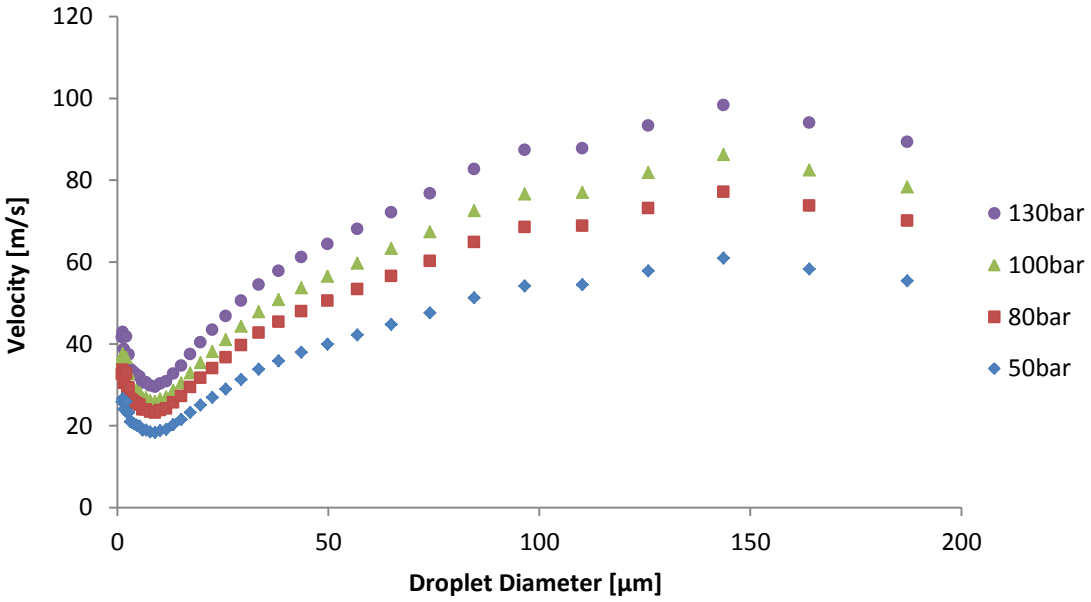

Figure 59: Droplets velocity input for the model

4 Modelling activity

This chapter provides a detailed analysis of the model developed to predict the results of the particle capture process in our test facility. The experimental data obtained with the spray analysis are used as model input and to evaluate its evolution. This model is a further development and evolution of the work previously done in RSE (F. Casella 2014).

4.1 Introduction

The model is based on a Eulerian point of view of the process. The fluidodynamic behaviour of the spray is firstly took into account with an analysis of the air-droplet and droplet-droplet interaction, then the interaction between droplet-particulate will determinate the evolution of the capture process.

The main hypotheses behind this work are:

- Monodirectionality of the spray, the physical properties of the droplets evolve along its axis while being uniformly distributed among the radial coordinate (because in high pressure sprays the cone angle is very narrow and the axial component of the velocity is predominant to the radial one);
- Particulate matters is uniformly distributed in the chamber;
- No evaporation (the air of the chamber become saturated in a few seconds after the spray activation);
- Only gravitational and diffusive mechanism are taken into account for particle agglomeration since phoretic effects are negligible in our configuration (ambient temperature and no steam that condense on the droplet surface);
- No breakup;
- Negligible particulate capture outside the spray;

The parameters that can be modified are:

- Water pressure;
- Nozzle k-factor;
- Initial droplets velocity and size distribution;
- Spray cone angle;
- Spray height;
- Air velocity outside the spray;
- Dimension, density and initial concentration of the monodispersed particulate;
- Chamber volume;
- Time and space discretization step;

The model will calculate, for each spatial step, the evolution of the spray characteristics and use them to calculate the efficiency of the decontamination process considering the particulate concentration at the end of each time interval.

4.2 Discretization

Three different discretizations are made in the model to properly treat the problem.
The cone is considered to be strictly of conical shape and from the axial distance of 5cm (thereby neglecting the initial part of the cone but avoiding the necessity of a break-up model) it is divided in many truncated cones: in our base case the spray is considered of 1,2m total height and each truncated cone of the dimension of 1mm.
The range of the considered droplet diameters is limited from 1 to 200 μm, to cover the diameters dimensions produced by the high pressure sprays. This range is then divided into 40 size intervals, called bins $1<N_b<40$), equispaced in a logarithmic scale of base 10, in order to obtain a higher accuracy for smaller droplets.
The time discretization used in the decontamination process is a multiple of a second and in our analysis is fixed to 1s and the total duration of the spray process is set to 120s to have a direct comparison with experimental data.

4.3 Model input

The model is developed around the nozzle used in our experimental activity so the k-factor and the cone angle are predetermined.
The k-factor is a parameter (mainly used in fire protection engineering) used to calculate the discharge rate from a nozzle. Its dimension is [kg s^{-1} $bar^{-0.5}$] and the mass flow rate is calculated as follows:

$$\dot{m} = k\sqrt{p_w} \qquad 4.1$$

The k-factor of our nozzle is k = 1.95 10^{-3} kg s^{-1} $bar^{-0.5}$.
The cone angle α is function of the water pressure but through a previously conducted photographic survey a constant value of around 15° has been measured (as showed in Figure 60) with no substantial difference with increasing pressures.

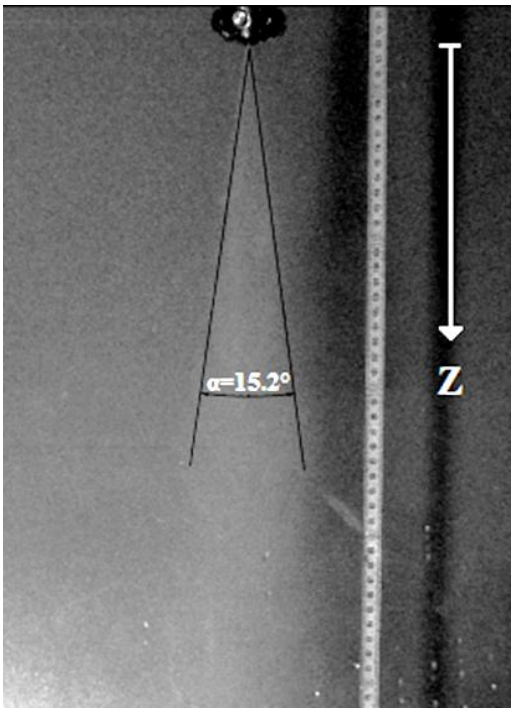

Figure 60: Photographic image of the spray at 80bar

The spray is considered to have a total height of 1.2m and inserted in a chamber with a total volume of 0.75m^3 (1.5x1x0.5m).

To have a direct comparison term with our experimental activity only the pressure of 50, 80, 100 and 130 bar are used to analyze the spray fluid dynamic and 50, 80 and 130bar for the decontamination process.

The initial droplet velocity and size distribution are taken from the experimental activity at Z=5cm from the spray nozzle, as shown in section 3.4.3. The size distribution obtained is measured as number flow rate (#/s) for each droplets class bin. To derive the "snapshot" number of droplets in the first truncated cone it is necessary to operate as follows:

$$\#_i = \frac{\frac{\#}{s_i}}{v_i}\Delta z \qquad 4.2$$

where $\#_i$ is the instantaneous number of droplets, $\frac{\#}{s_i}$ is the droplets number flow rate and v_i is the droplets velocity contained in the i-th class bin while Δz is the cone discretization step.

The external air velocity was, in a first approximation, considered to be zero due to the absence of measurements (even if in our measuring chamber some recirculation vortexes are visible outside the cone so the uniform particle concentration hypothesis is reinforced), but after the analysis of the results this assumption showed to be too strong. It has been found, in the post processing work, that a better approximation for this value is equal to 4% of the inlet bernoullian velocity.

The initial velocity of the air entrained into the cone spray is supposed to be equal to the smaller speed of the smaller droplets class since their low inertia implies that they reach equilibrium almost instantly with the fluid carrier phase.

The particulate matter is of amorphous silica having a density of 2000 kg/m^3 and with a monodispersed granulometry of 0.5, 1 or 2 µm .As stated above the particle is considered uniform inside the chamber volume.

4.4 Sub-models

4.4.1 Air-droplet interaction

The falling droplets are subjected to two main forces, the gravitational one that has a positive contribution to the falling velocity and the frictional one resulted from the interaction with the surrounding air also known as drag force. In our discretized environment a uniform value is assigned to the air around the droplets and the fact of having divided the spray cone in many thin layers makes this assumption not too strong.
As seen in section 1.2.4 the momentum balance of a drop falling in moving air is:

$$\frac{d}{dt}(mv) = mg - \frac{1}{8}\rho C_d \pi D_d^2 (v - v_{air})|v - v_{air}|$$

After integration and discretization, the loss of velocity for the droplets in each i-th size class is:

$$\Delta v_{d_i} = \left[\frac{3\,\rho_{air}\,C_D\,(\tilde{v}_{d_i} - \tilde{v}_{air})^2}{4\,\rho_d\,D_{d_i}} - 9.81\right]\Delta t_i \qquad 4.3$$

$$v_{d_i} = max\,(\tilde{v}_{d_i} - \Delta v_{d\,i}\,;\; v_{air}\,) \qquad 4.4$$

$$\Delta t_i = \frac{\Delta z}{\tilde{v}_{d_i}} \qquad 4.5$$

where the accent ~ indicates the outlet values of the previous control volume, the minimum velocity is capped at the value of the air velocity to prevent errors tied to the fact that this model is of the first order.
The drag coefficient is function of the flow Reynolds number as indicated in equation 1.13 and reported in Figure 61:

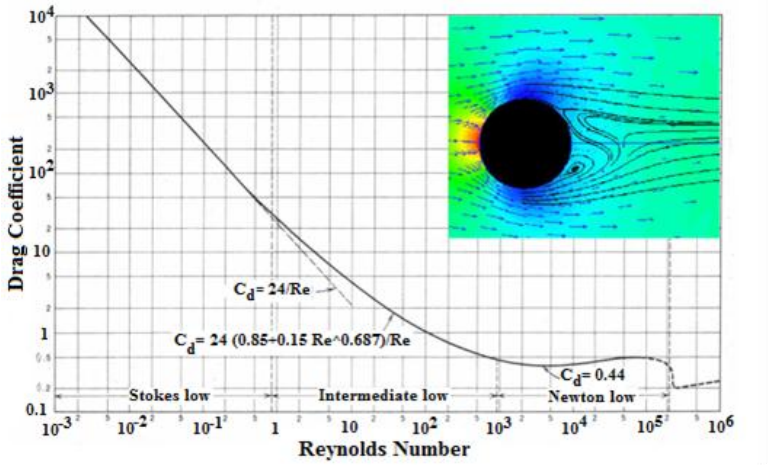

Figure 61: Drag coefficient function of the Reynolds number

The Reynolds number is calculated as (Mahmud et al., 2012):

$$Re = max\left[\frac{\rho_{air}\, D_d\, (\tilde{v}_d - \tilde{v}_{air})}{\mu_{air}}; 0.01\right] \quad 4.6$$

The velocity of the entrained air can be calculated from a momentum balance over the current control volume:

$$m_{air}\, v_{air} = \tilde{m}_{air}\, \tilde{v}_{air} + m_{air,ext}\, v_{air,ext} + \sum_{i=1}^{N_b} m_{d_i}\, \Delta v_{d_i} \quad 4.7$$

where m_{air} is the mass of the entrained air and can be calculated as:

$$m_{air} = V_{air}\, \rho_{air} \quad 4.8$$

$$V_{air} = V_{cv} - V_d \quad 4.9$$

$$V_d = \sum_{i=1}^{N_b} N_{d_i}\, V_{d_i} \quad 4.10$$

$$m_{air,ext} = m_{air} - \tilde{m}_{air} \quad 4.11$$

with V_{cv} the total volume of the truncated cone taken as control volume, V_d the total volume occupied by all droplets and $m_{air,ext}$ the mass of air encompassed with the growth of the control volume with each axial spatial step.
An average value of the droplets velocity is then obtained through:

$$\tilde{v}_d = \frac{\sum_{i=1}^{N_{bin}} \tilde{v}_{d_i}\, \dot{m}_i}{\sum_{i=1}^{N_{bin}} \dot{m}_i} \quad 4.12$$

4.4.2 Droplet-droplet interaction

In our model the only interaction allowed to the droplets is agglomeration. As shown in section 1.2.6 agglomeration is a mechanism that moves the diameters size distribution toward bigger size conserving the total mass of the spray.
In the Eulerian model, in every control volume, the total mass flow rate is preserved, not the mass (in the snapshot of the control volumes near the nozzle there will be few droplets with high velocity while in the ones near the bottom there will be many droplets with a low velocity, this implies that the droplets mass contained in each control volume increases with the distance from the nozzle). So the evolution of the size distribution in each subsequent control volume has to take into account the agglomeration and it must also provide the correct number of droplets that will generate the correct mass flow rate.
The first step is to determinate the droplets size distribution in each control volume by considering the evolution of the initial number of droplets subject of agglomeration through all the control volumes.

The collision probability among droplets of i and j classes is based on the calculation of the collision kernel $\Phi_G(D_{d_i}, D_{d_j})$ [$m^3\ s^{-1}$] related to the gravitational agglomeration and its formulation has been taken from aerosol growth theory (Allen et al., 2001):

$$\Phi_G\left(D_{d_i}, D_{d_j}\right) = \frac{\pi}{4}\left(D_{d_i} + D_{d_j}\right)^2 \left|v_{d_i} - v_{d_j}\right| \varepsilon \qquad 4.13$$

where ε is the collision efficiency and evaluate the effective probability of the collision between the streamlines. A unitary value of this parameter has been previously used but after comparing the model results with the experimental data, it has been seen that $\varepsilon = 1$ leads toward higher dimension in the droplets mean diameter (probably due to the lack of a break-up model) so it has been seen that $\varepsilon \cong 0.65$ correctly matchup.
The droplet born from the agglomeration will have the following diameter:

$$D_d = \sqrt[3]{D^3{}_{d_i} + D^3{}_{d_j}} \qquad 4.14$$

With i>j, if the new diameter shifts in a size bin higher than the size bin i, therefore the model adds a droplet in the higher size bin and it removes a droplet in each size bin i and j, otherwise only the j class droplet is removed.
The total number $N\left(D_{d_i}, D_{d_j}\right)$ of droplets that agglomerate in each control volume and size bin is then calculated as follow:

$$N\left(D_{d_i}, D_{d_j}\right) = \Phi_G\left(D_{d_i}, D_{d_j}\right)\ C\left(D_{d_i}\right)\ C\left(\ D_{d_j}\right)\ V_{cv}(z)\ \Delta t_{d_i} \qquad 4.15$$

where C indicate the number density of the class i and j [#/cm^3] and $\Delta t_{d_i} = \frac{\Delta z}{v_i}$.
In each k-th control volume the new value of the droplets number $N_{i\text{-}k}$ of the i-th class is available and the mass flow rate associated to that class can be calculated as:

$$\dot{m}_{i-k} = \frac{N_{i-k} V_i \rho_d}{\Delta t_{d_{i-k}}} \qquad 4.16$$

The result of the sum among all size bins $\sum_i \dot{m}_{i-k} = \dot{m}_k$ represents the total mass flow rate in the considered control volume. This obtained value is different from the real flow rate $\dot{m}_{nozzle}$ so there is the necessity to uniformly "inflate" the number distribution in order to obtain the correct mass flow rate in each control volume. To calculate the correct number of droplets, $\widehat{N}_{i-k}$, in each size bin $N_{i\text{-}k}$ is multiplied by a factor equal to the ratio $\dot{m}_{nozzle}/\dot{m}_k$.

$$\widehat{N}_{i-k} = N_{i-k}\frac{\dot{m}_{nozzle}}{\dot{m}_k} \qquad 4.17$$

4.4.3 Droplet-particulate interaction

The agglomeration process between droplets and particulate matters occurs mainly for differences in their respective, but as the particulate dimensions tends toward the sub-micron range the diffusive mechanism contribution due to Brownian motions to the global process increase in magnitude and can't be neglected anymore, so a global collision kernel need to be calculated.
The gravitational agglomeration contribution is the same as in the previous paragraph 4.4.2:

$$\Phi_G\left(D_{d_i}, D_p\right) = \frac{\pi}{4}\left(D_{d_i} + D_p\right)^2 \left|v_{d_i} - v_p\right| \varepsilon \qquad 4.18$$

The subscripts d_i and p respectively represent the i-th droplet diameter class and the particulate matter with its velocity v_p assumed to be equal to the air velocity v_{air} due to its low inertia. The efficiency of this mechanism is very low since the high difference in the dimensions and it has been found that the best fitting experimental value for ε are 9,58E-06 for 0.5μm 1,81E-05 for 1μm and 3.39E-05 for 2μm particulate size.
The Brownian diffusion kernel Φ_B is calculated with the following expression (Fuchs, 1964; Perkin; Lehtinen, 1997):

$$\Phi_B\left(D_{d_i}, D_p\right) = \frac{2\,k\,T}{3\,\mu}\left(\frac{1}{D_{d_i}} + \frac{1}{D_p}\right)\left(D_{d_i} + D_p\right) \qquad 4.19$$

with k [kg $m^2 s^{-2} K^{-1}$] the Boltzmann's constant, T and μ [kg $m^{-1} s^{-1}$] the temperature and dynamic viscosity of the carrier phase (air).
The overall agglomerating kernel is then calculated as follows (ECART, 2011):

$$\Phi_T = \Phi_B + 1.09\,\Phi_G \qquad 4.20$$

The number of collision (and particle captured) between droplets of the i-th size class in the k-th control volume is then calculated with as follow to take into account the integration over the discretization time step:

$$N_{i-k}\left(D_{d_i}, D_p\right) = \Phi_T C\left(D_{d_i}\right) C\left(D_p\right) V_k \frac{time\ step}{\Delta t_{d_i}} \qquad 4.21$$

With $C(D_p)$ the particulate concentration that is assumed to be uniform in all the chamber volume inside the same time step.
The particle concentration at the end of each time step is then obtained from the difference between the initial particle count in the chamber and the total number of particulate captured in each k-th control volume by each i-th droplet class:

$$C_{t+time\ step} = C_t - \frac{\sum_k \sum_i N_{i-k}\left(D_{d_i}, D_p\right)}{V_{sc}} \qquad 4.22$$

With V_{sc} the volume of the scrubbing chamber.

4.5 Results and comparison with experimental data

4.5.1 Spray fluid-dynamics

In this section the results obtained by the model regarding droplets count, velocity and size distribution will be shown. They will be compared with the experimental results at the Z height available of 100, 250, 500 and 750 mm. The results present here refers to an intermediate pressure of 100 bar.

4.5.1.1 Droplet distribution

As first the droplet size distribution, at different distance from the nozzle, will be shown and compared with the experimental results.

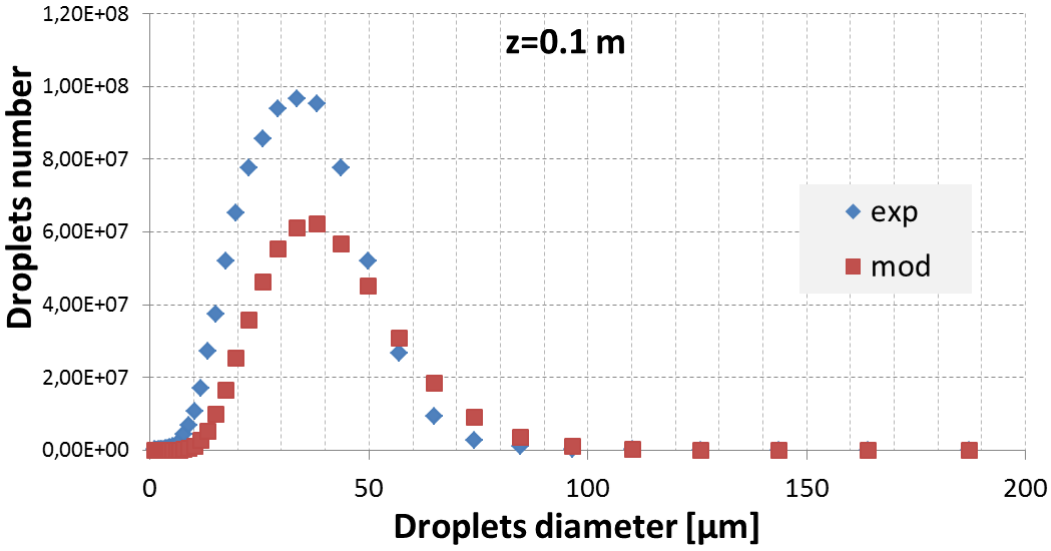

Figure 62: droplets size distribution at 0.1 m from the nozzle, experimental and modelled values

As shown in Figure 62, the two distributions, at 10 cm from the nozzle, have similar profiles, they show a peak in the same range but the model underestimates the number of droplets with lower diameters while slightly overestimates the droplets with diameters higher than 60 µm. This behaviour can be explained by the lack of a break-up sub-model that will reduce the number of bigger droplets and increase the number of the smaller ones. Another explanation could be that a uniform value of the agglomeration efficiency ε can lead to an underestimation of some agglomerations and an overestimation of other.

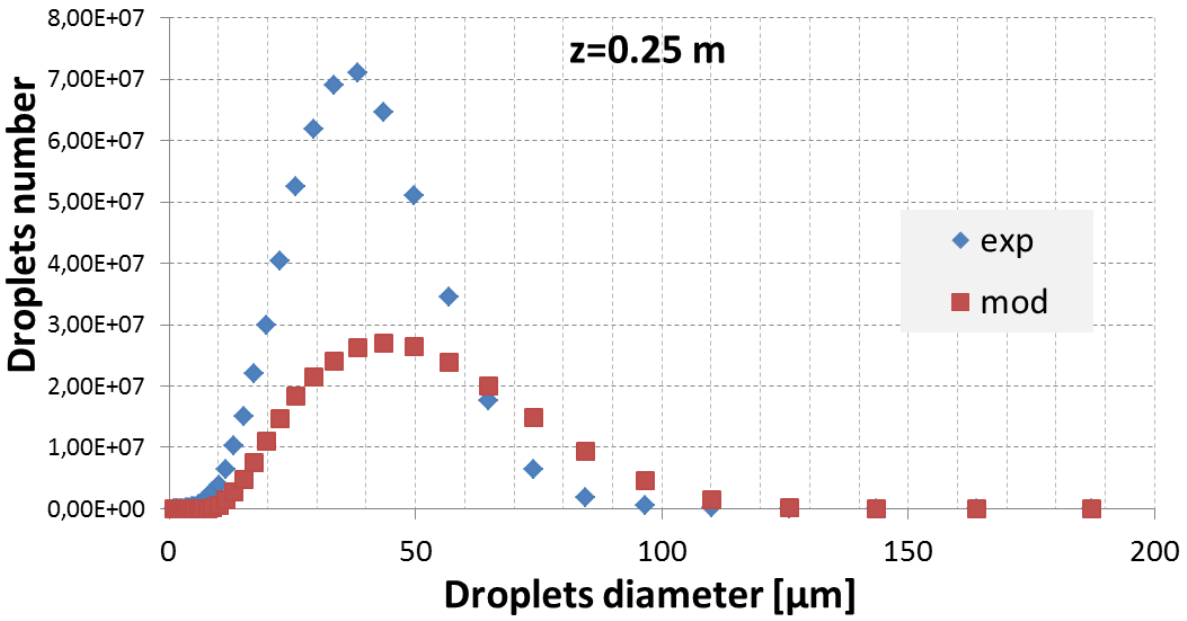

Figure 63: droplets size distribution at 0.25 m from the nozzle, experimental and modelled values

In Figure 64 is clearer that there is a further overestimation of the bigger droplets and since the distance from the spray nozzle has grown (25 cm), we should already be outside the break-up zone. The main reason for this behavior is the assumption of a constant ε that overestimates the agglomeration of the smaller droplets.

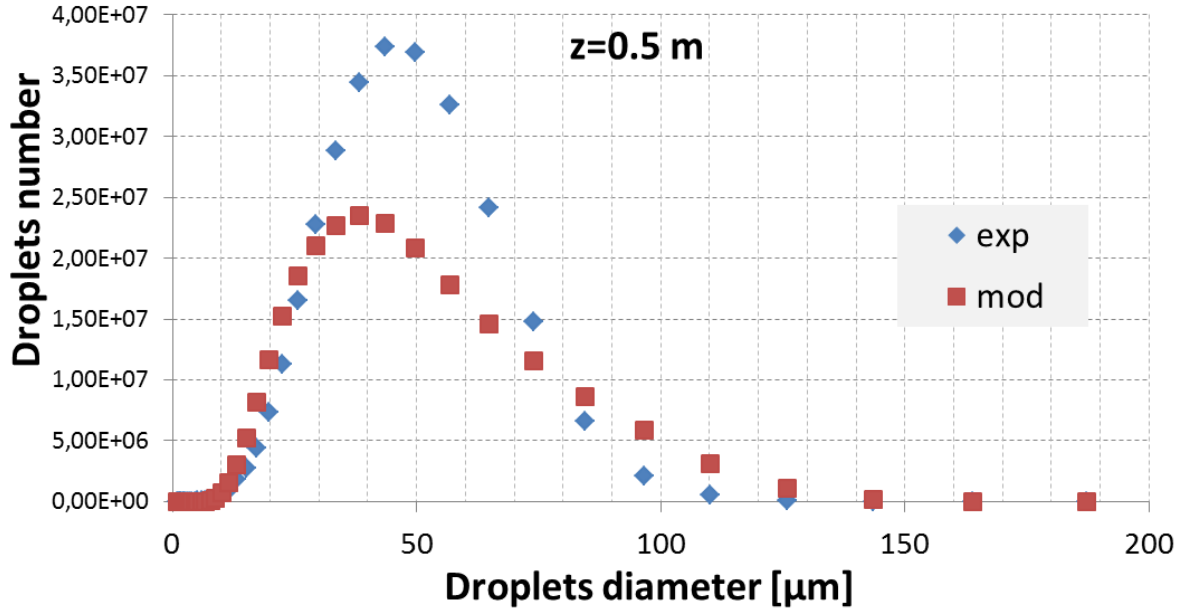

Figure 64: droplets size distribution at 0.5 m from the nozzle, experimental and modelled values

The droplet size distribution at 50 cm from the nozzle, reported in Figure 64, shows that there is always a slight overestimation of the bigger droplets, but the maximum of the distribution is moving toward smaller diameters. It is a sign that the agglomeration kernel, that is a function of the relative velocity between the droplets, is decreasing its magnitude due to the fact that the smaller droplets are the one that faster reach the equilibrium with the air (can be seen in the following chart where velocity is shown).

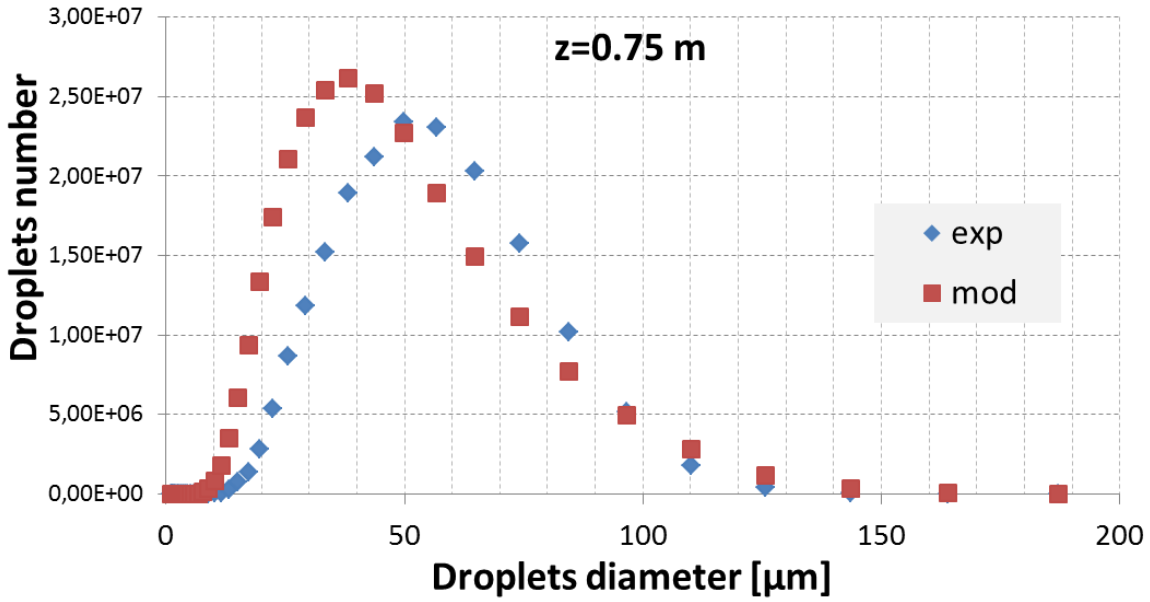

Figure 65: droplets size distribution at 0.75 m from the nozzle, experimental and modelled values

Figure 65 further validate what explained before.

Figure 66 shows the evolution of the Sauter mean diameter, D32, with the distance from the nozzle Z. We have monitored this specific diameter because it takes in account both the volume and the superficial area of the droplets that is very important for agglomeration.

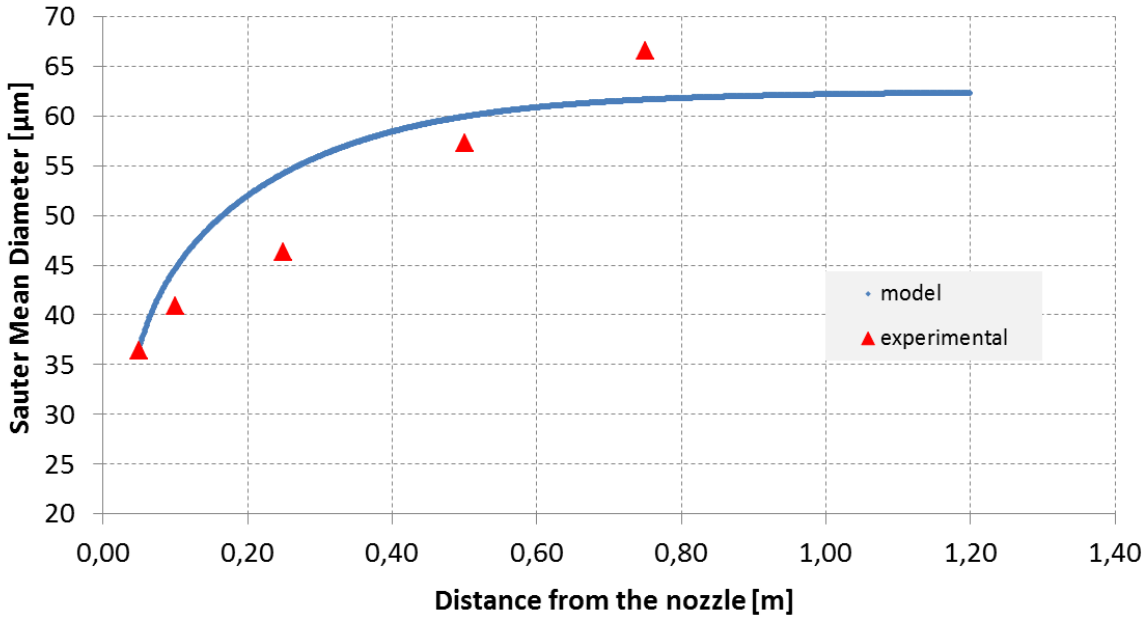

Figure 66: Sauter mean diameter as function of Z, experimental and modelled values

It is clear here that a slight overestimation of the agglomeration process occur in the first half of the spray height, around 0.6 m, while after this point it almost completely stop reaching an asymptotic value of 63 µm. The last experimental D32 value at 0.75 m is 66 µm and it is expected that at

further distance it will not continue to linearly grow as with lower heights and will reach a maximum value not far away from the modeled one.

In Figure 67 and Figure 68 the distributions of the droplets number and mass is showed. It is conserved the log-normal shape with increasing Z. The subtended area increases with the distance from the nozzle, since more droplets are suspended at the same time due to the decrease in their velocity. The peak of the distribution moves toward higher diameters with increasing Z.

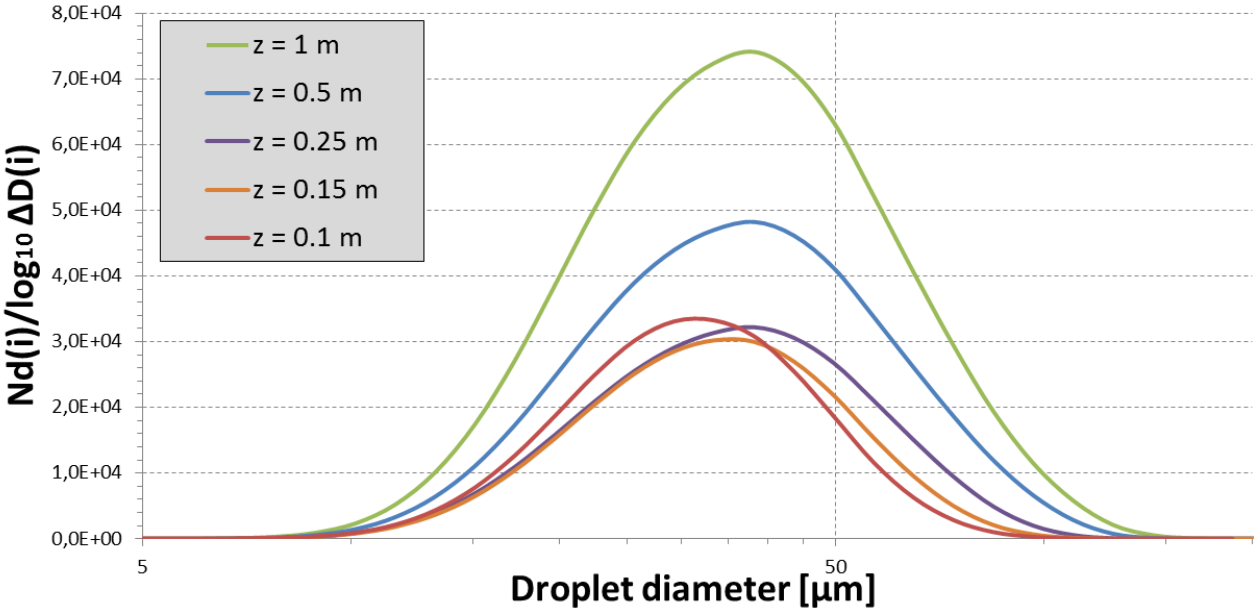

Figure 67: droplets number distribution at different heights

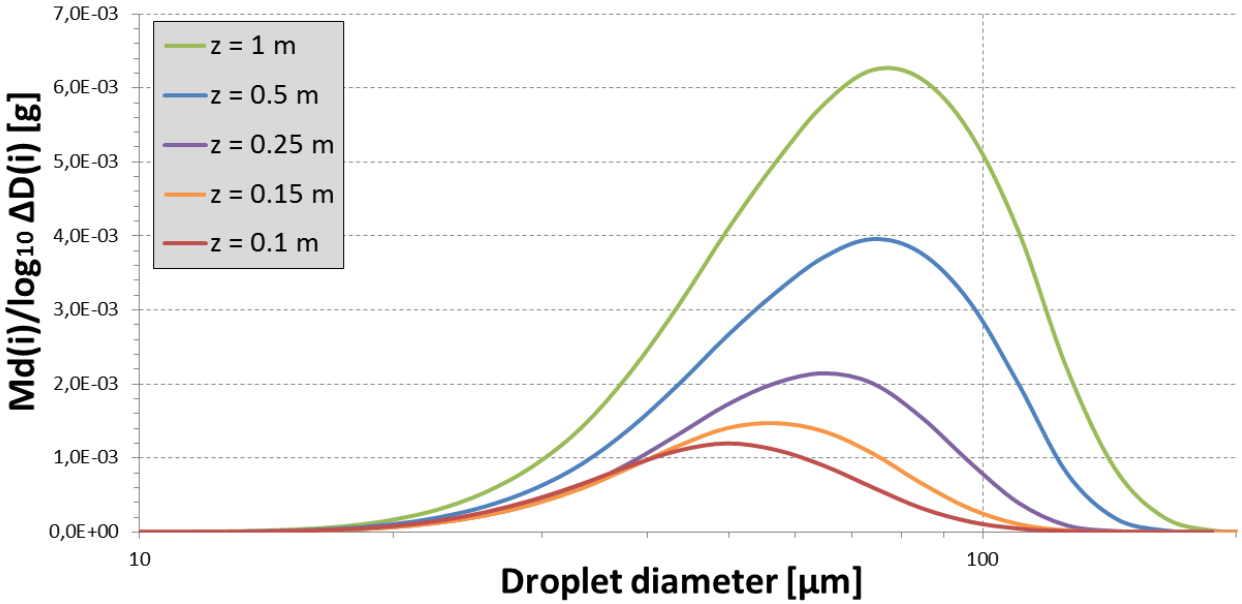

Figure 68: droplets mass distribution at different heights

4.5.1.2 Droplet velocity

The model well approximates the experimental velocities in the initial region as shown in Figure 69.

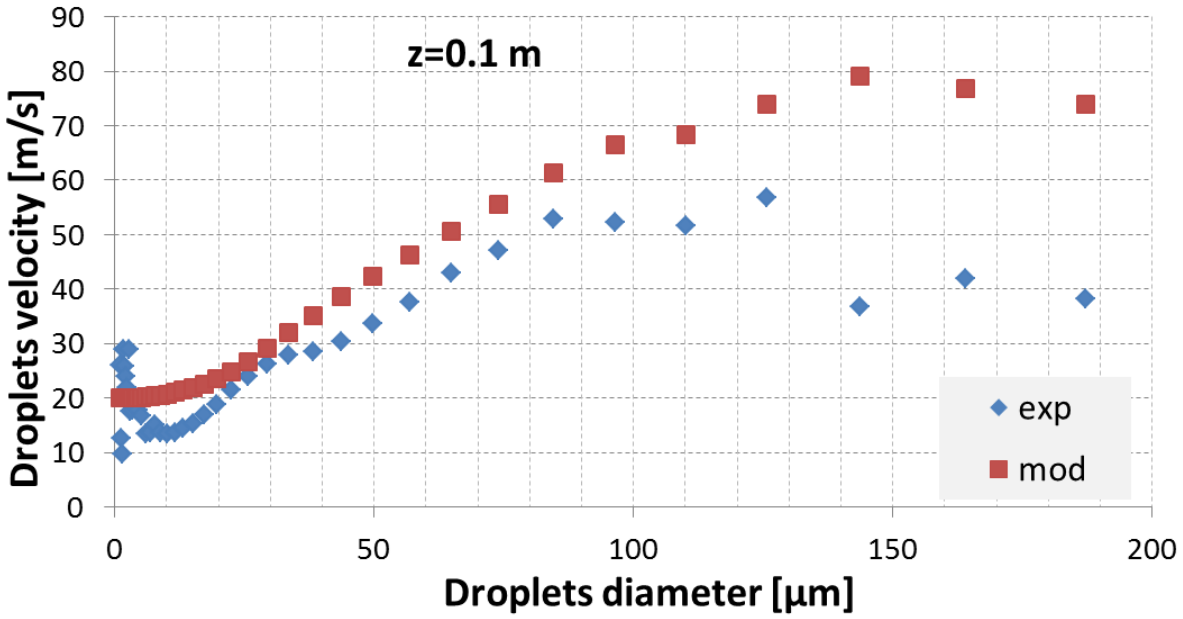

Figure 69: velocity of each droplet size interval at 10 cm from the nozzle, experimental and modelled values

Figure 70 shows that the model slightly overestimates the loss of velocity of the smaller droplet, while the bigger droplets do not loose enough momentum.

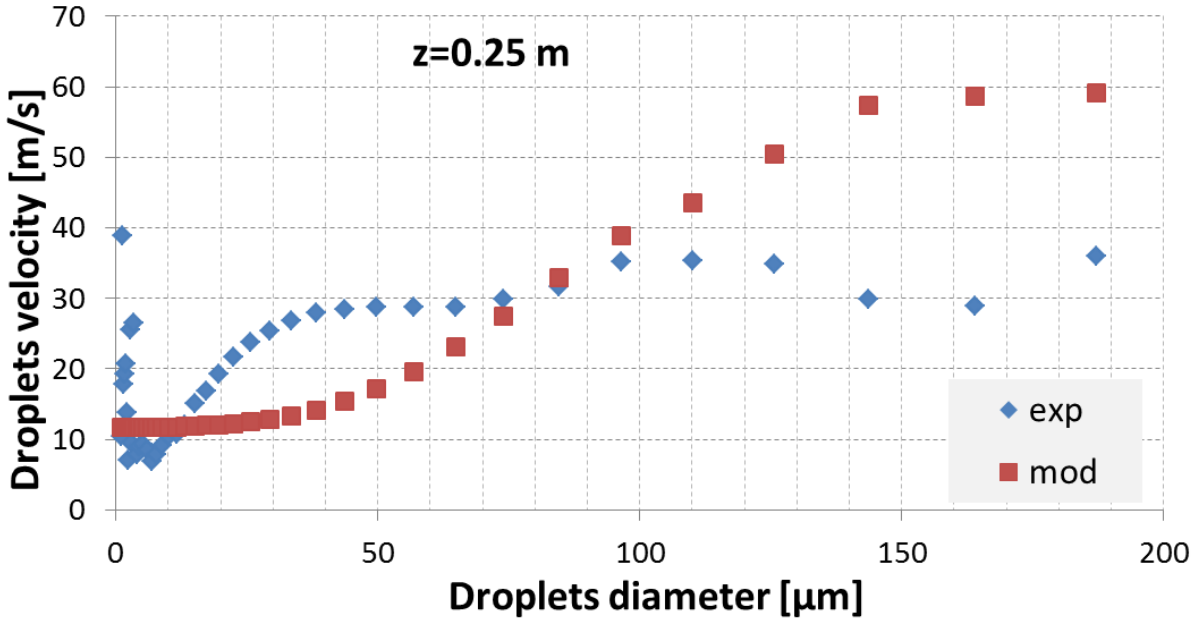

Figure 70: velocity of each droplet size interval at 25 cm from the nozzle, experimental and modelled values

Figure 71 and Figure 72 show that almost all droplets reach a constant value of velocity. The measurements bring to light that the smaller droplets, under 20 µm, keep values of velocity different from the equilibrium one. The bigger droplets, in the model, retain too much momentum, probably because it is considered only the drag force and dissipative mechanisms in droplets mutual interaction are not taken into account.

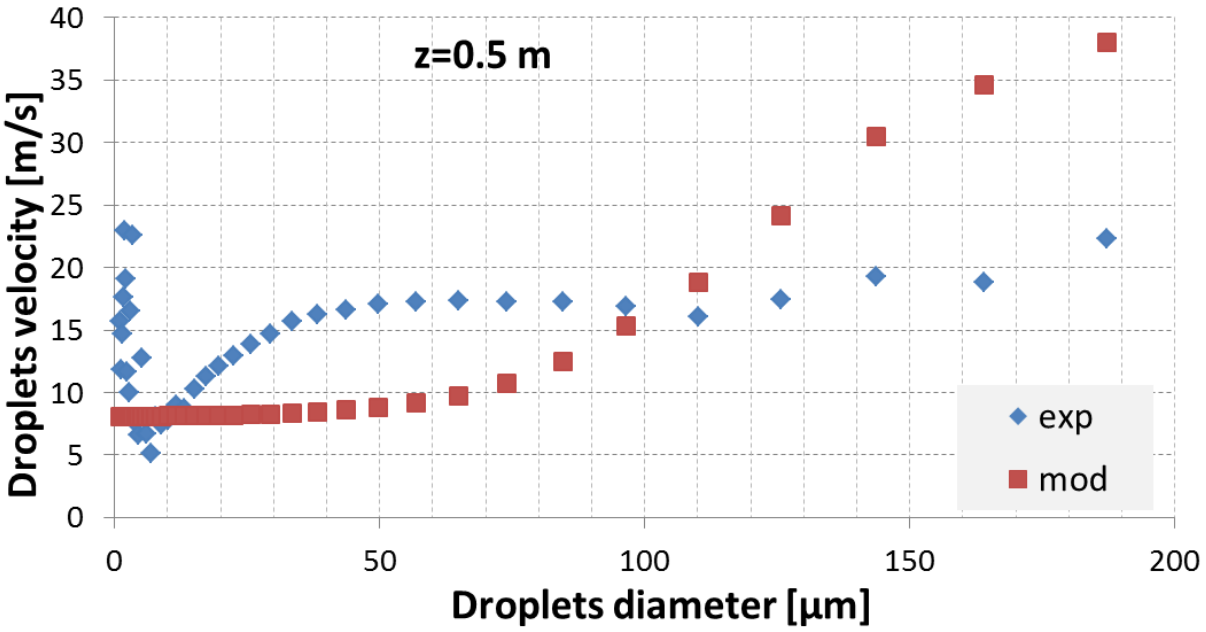

Figure 71: velocity of each droplet size interval at 50 cm from the nozzle, experimental and modelled values

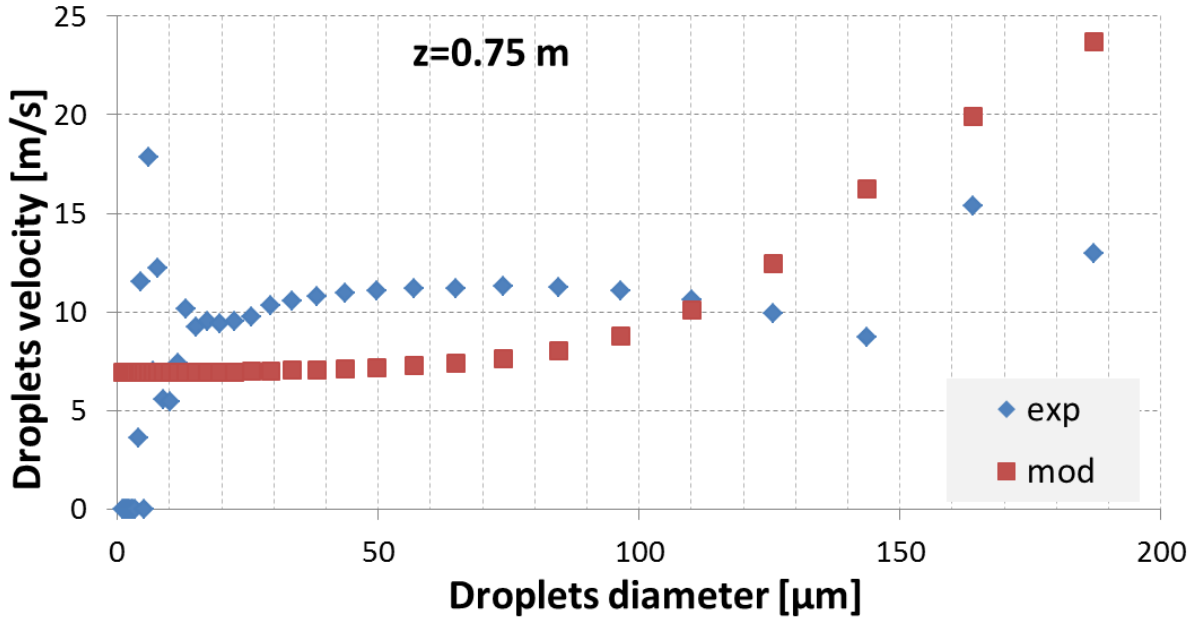

Figure 72: velocity of each droplet size interval at 75 cm from the nozzle, experimental and modelled values

Figure 73 shows the evolution of the mean values of velocity for both droplets and air. The droplet velocity is quite precise in the first quotes, while the modeled values are slightly lower than the experimental ones as the distance grew. The air velocity curve show that the assumption for its initial value is correct since it is only slightly modified in the sequent steps.

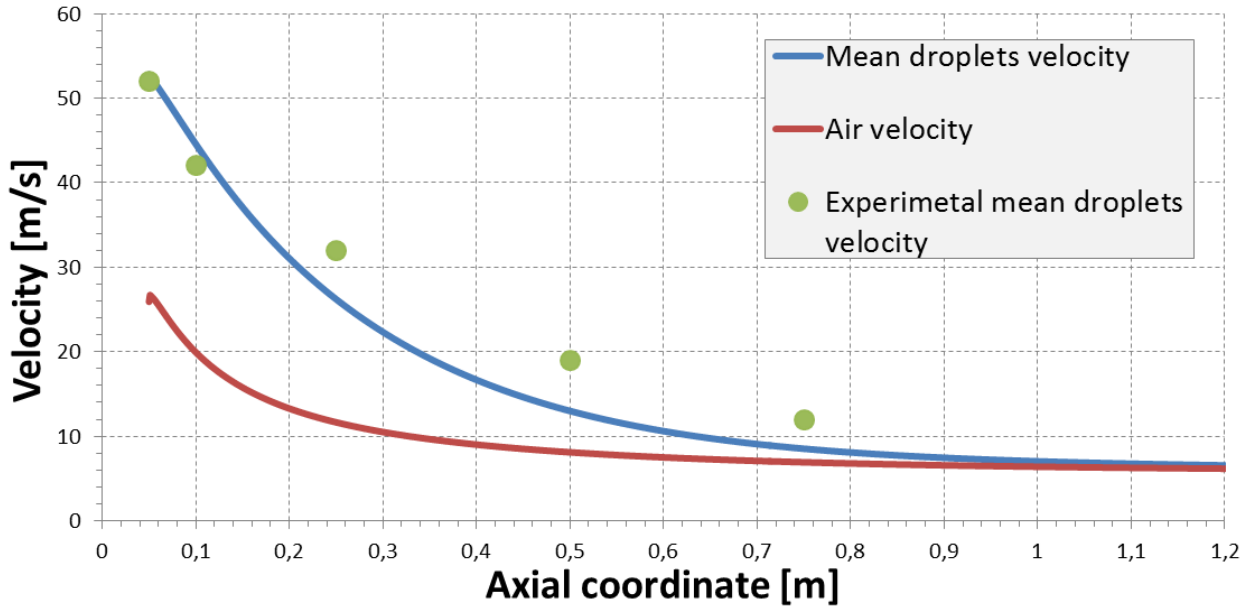

Figure 73: air and droplets average velocity, experimental and modelled values

4.5.2 Decontamination results

In this section the decontamination results provided by the model are compared with the experimental data.

It has been seen that the experimental decontamination coefficient λ is not influenced by the initial aerosol concentration but only by the powder dimension and the water injection pressure. The model results show the same behavior, with predicted results included in a 10% range.

The results obtained with the 0.5 µm, 1 µm and 2 µm powders are shown respectively in Figure 74Figure 75Figure 76.

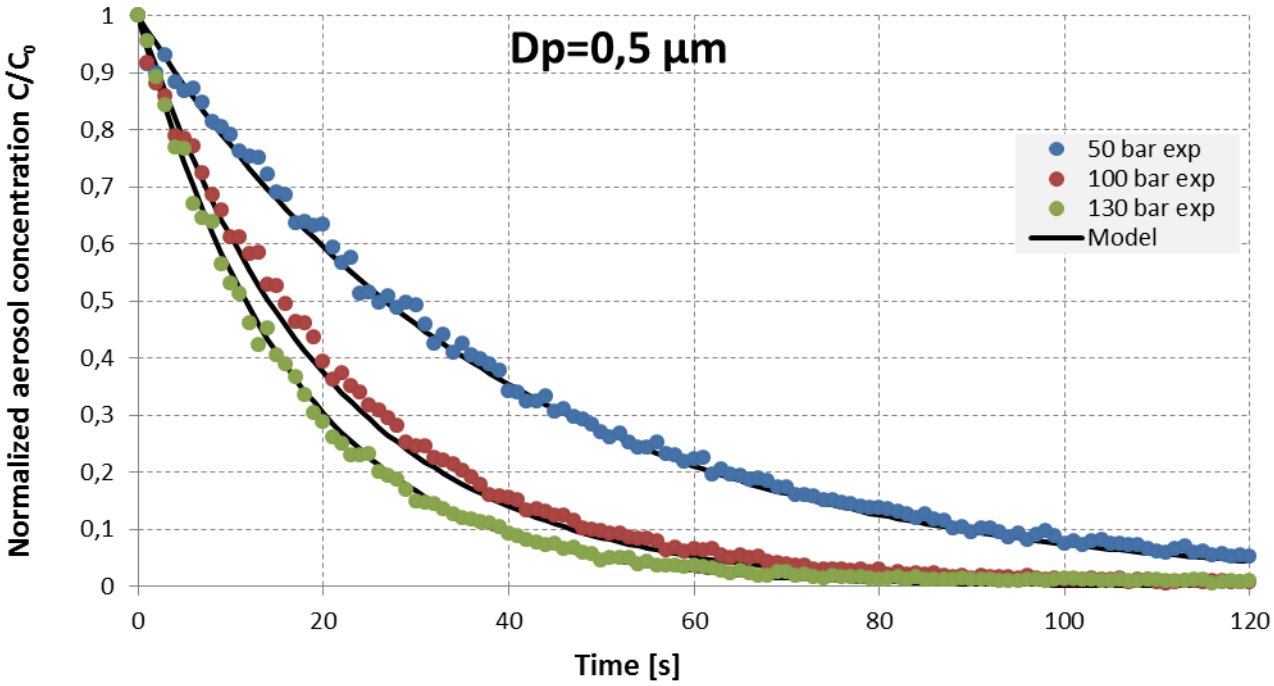

Figure 74: decontamination curves for 0.5 µm aerosol as function of the water injection pressure, experimental and model results.

The differences in the decontamination coefficients are summarized in Table 10 for 0.5 µm, in Table 11 for 1 µm and in Table 12 for 2 µm. The results show good agreement with the experimental data.

Table 10: comparison between experimental data and model results for 0.5 µm aerosol

P [bar]	$\lambda_{experimental}$ [1/s]	λ_{model} [1/s]	$(\lambda_{exp-} \lambda_{mod})/ \lambda_{exp}$ [%]
50	0.025	0.026	4.53
100	0.050	0.049	2.08
130	0.063	0.060	5.18

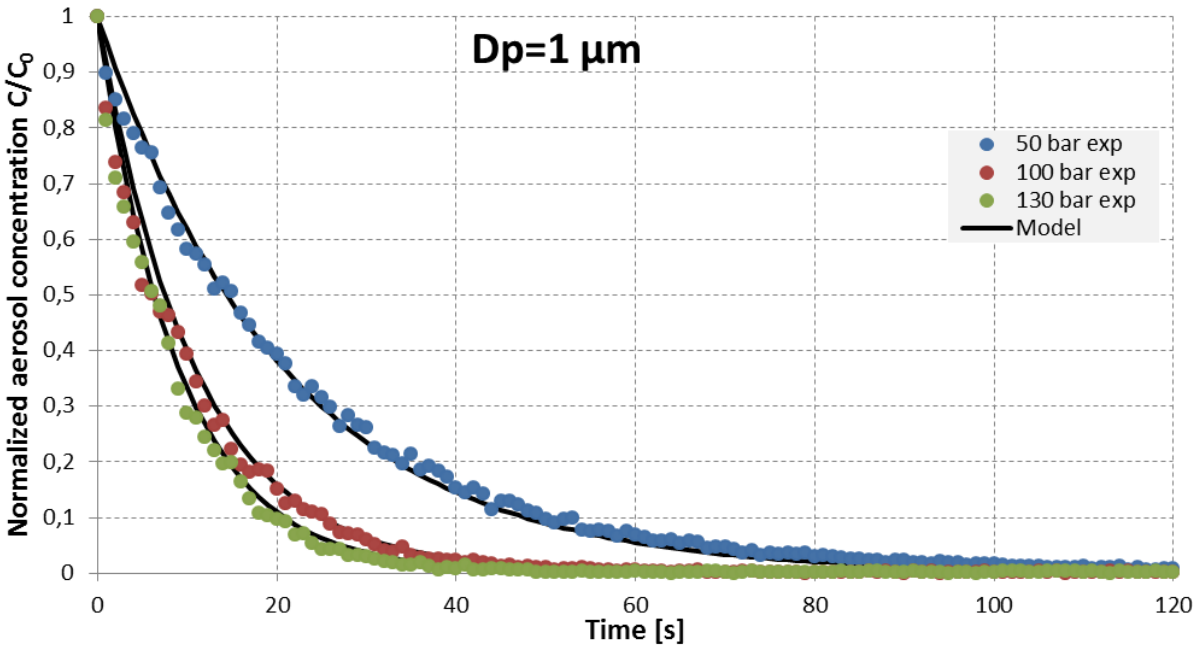

Figure 75: decontamination curves for 1 µm aerosol as function of the water injection pressure, experimental and model results.

Table 11: comparison between experimental data and model results for 1 µm aerosol

P [bar]	$\lambda_{experimental}$ [1/s]	λ_{model} [1/s]	$(\lambda_{exp-} \lambda_{mod})/ \lambda_{exp}$ [%]
50	0.049	0.048	2.0
100	0.092	0.092	0.2
130	0.116	0.110	5.4

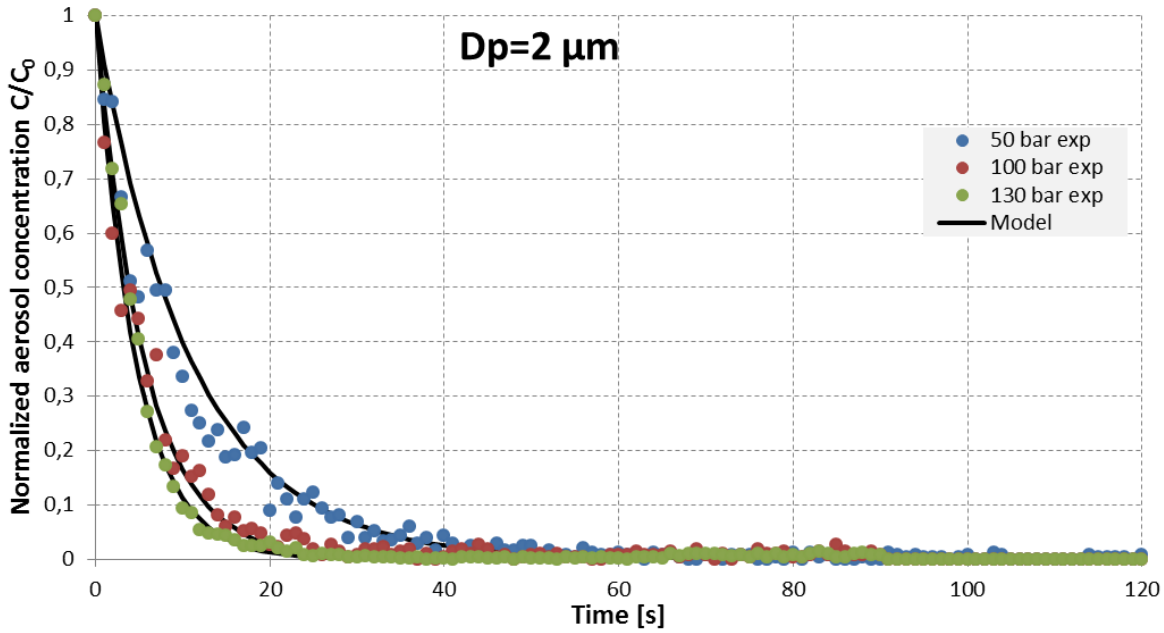

Figure 76: decontamination curves for 2 µm aerosol as function of the water injection pressure, experimental and model results.

Table 12: comparison between experimental data and model results for 2 µm aerosol

P [bar]	$\lambda_{experimental}$ [1/s]	λ_{model} [1/s]	$(\lambda_{exp-} \lambda_{mod})/ \lambda_{exp}$ [%]
50	0.103	0.092	10.91
100	0.179	0.180	0.42
130	0.200	0.218	8.79

As final comparison in Figure 77 the results for the different powder are highlighted as function of the water injection pressure.

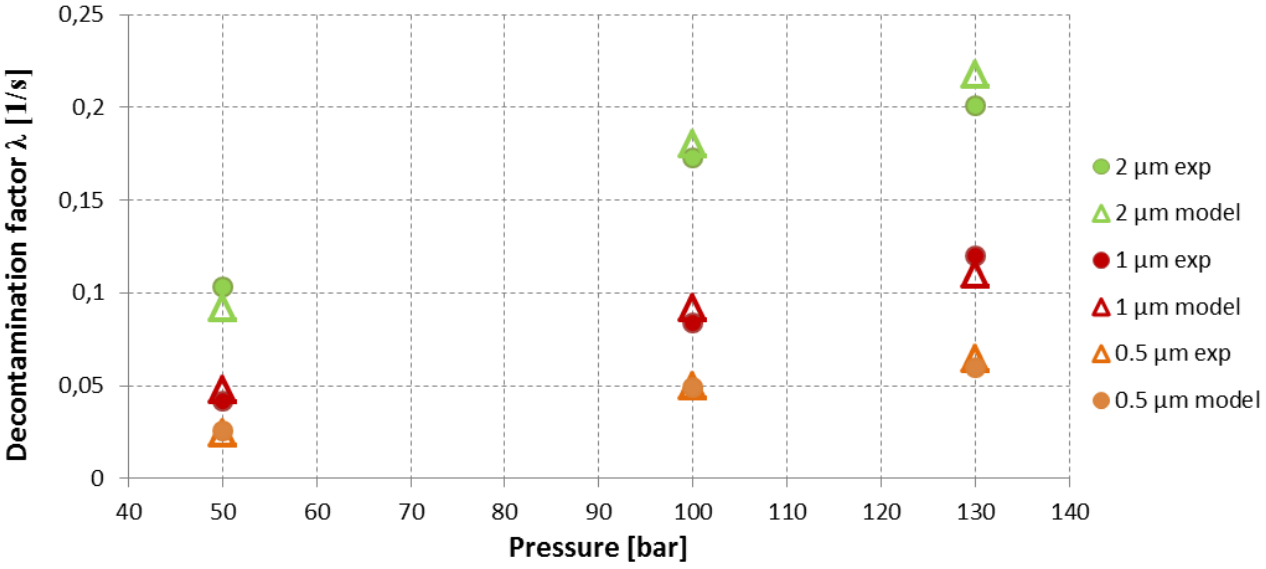

Figure 77: decontamination coefficient as function of the water pressure and aerosol size, experimental and model results

4.6 Sensitivity analysis

In this chapter is evaluated the need to carry out a detailed analysis of the spray structure to obtain reliable results.
Three different cases are showed:

- Constant input velocity, with the droplet number distribution obtained from our experimental results;
- A log-normal distribution obtained with just mean diameter and geometric standard deviation of the spray, with the velocity obtained from our results;
- Log-normal input distribution and uniform droplet velocity;

Each case will be compared with the experimental result obtained at a pressure of 100 bar, showing the evolution of the D32 and average droplet velocity and the decontamination coefficient for the different aerosol compositions.

4.6.1 Uniform velocity

The average velocity of the droplet calculated at 100 bar at 5 cm from the nozzle is 52 m/s so this value will be assigned as input value to all droplets.
As we can see in Figure 78 the resulting average velocity is slightly lower than the original model input. Figure 79 show that a uniform inlet velocity between different droplet sizes will lead to an underestimation of the agglomeration process between droplets, that is a function of the droplets relative velocity.

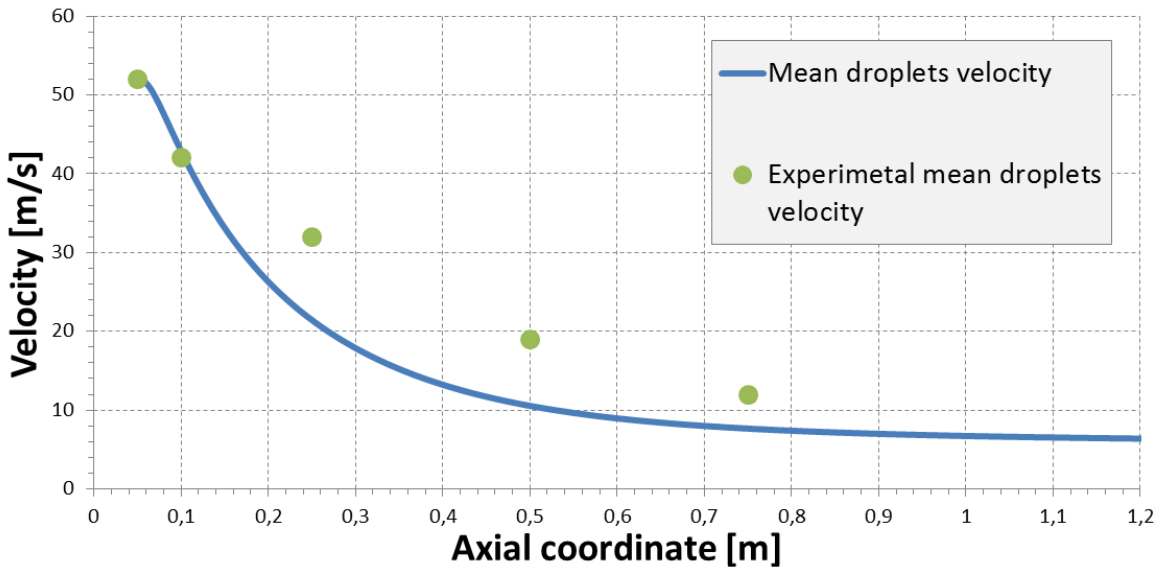

Figure 78: sensitivity analysis, mean droplet velocity evolution with uniform inlet velocity

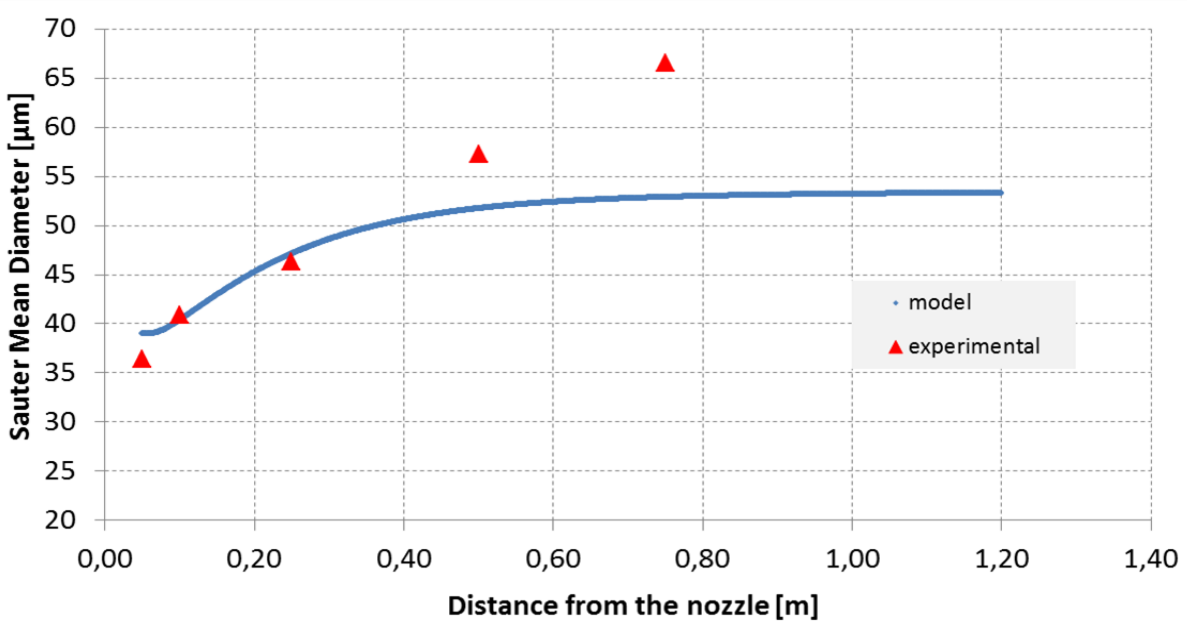

Figure 79: sensitivity analysis, Sauter mean diameter evolution with uniform inlet velocity

Table 13 show that the predicted values for λ are too far away from the experimental results.

Table 13: sensitivity analysis, decontamination coefficient λ with uniform inlet velocity

Dp [µm]	λ_{exp} [1/s]	λ_{mod} [1/s]	$(\lambda_{exp}-\lambda_{mod})/\lambda_{exp}$ [%]
0.5	0.05	0.041	18.0
1	0.092	0.072	21.7
2	0.179	0.139	22.3

4.6.2 Log-normal droplet size distribution

In this case the droplet velocity is kept as calculated in our experimental analysis, while the droplet size distribution is calculated with a generalized log-normal distribution:

$$f(D_i) = \frac{1}{D_i\sqrt{2\pi\sigma^2}} e^{\left(\frac{\ln(D_i)-\ln(\overline{D_{32}})}{\sqrt{2}\sigma}\right)^2}$$

Where $f(D_i)$ is the probability of the generic droplet to belong to the i-th size interval, σ is the geometric standard deviation in logarithmic scale and $\overline{D_{32}}$ is the Sauter mean diameter at that height.

At this pressure of 100 bar our experimental data says that $\overline{D_{32}}$=38 µm and σ =0.368 .

The total number of droplets present in each droplet size interval is then calculated as follows:

$$N_i = \frac{\dot{m} f(D_i) \Delta D_i \Delta t_i}{\rho_w \frac{4}{3}\pi r_i^2} \qquad 4.23$$

Where:

- $\dot{m}$ is the total mass flow rate;
- ΔD_i is the difference between the i-th diameter size class upper and lower bound;
- Δt_i is the time to cross the spatial step for i-th size class droplet;
- P is the droplet density;
- r_i is the droplet radius;

As we can see from Figure 80 the droplet velocity profile is the same used in our model.

Figure 81 show that this distribution gave as result a D_{32} profile very similar to the one obtained in the original simulation.

Table 14 show that the decontamination results provided well approximate the experimental data.

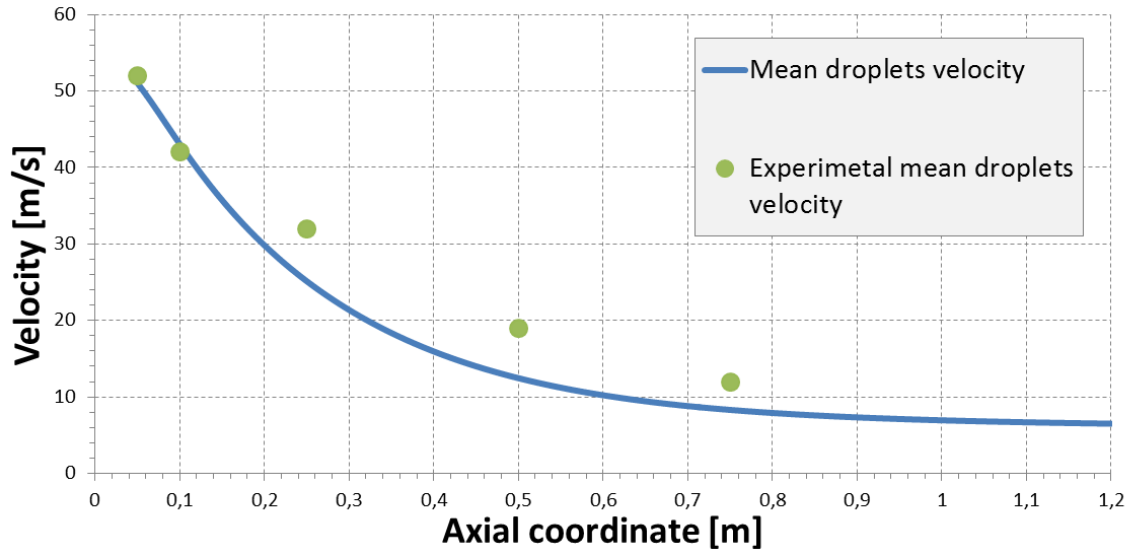

Figure 80: sensitivity analysis, mean droplet velocity evolution with log-normal size distribution as input

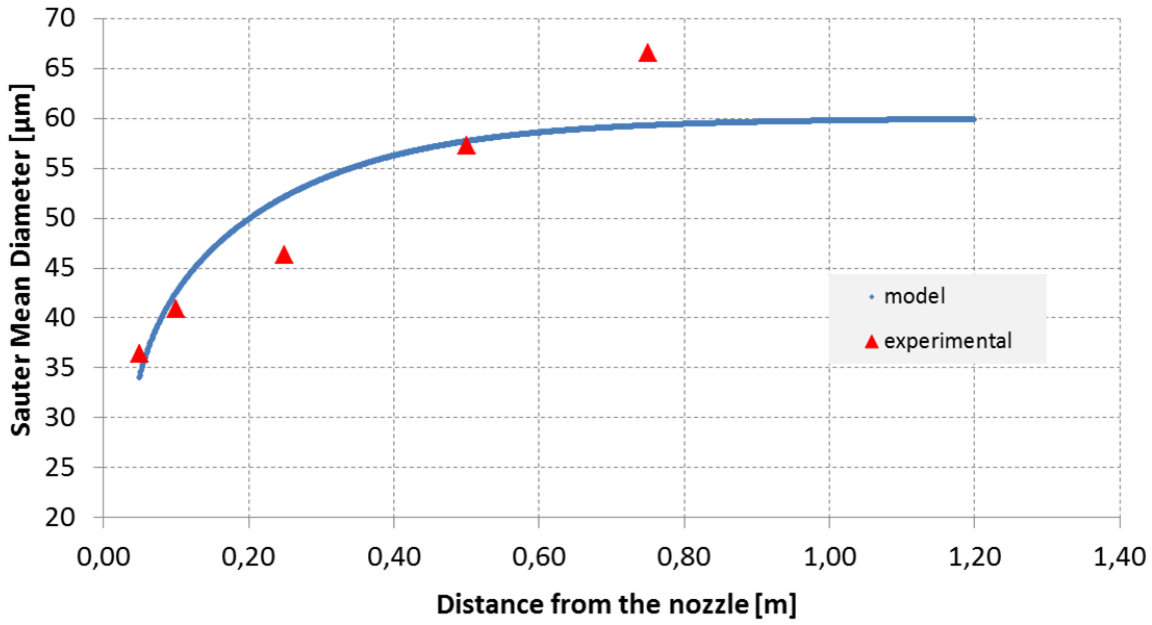

Figure 81: sensitivity analysis, Sauter mean diameter evolution with log-normal droplet size distribution as input

Table 14: sensitivity analysis, decontamination coefficient λ with log-normal droplet size distribution as input

Dp [µm]	λ_{exp} [1/s]	λ_{mod} [1/s]	$(\lambda_{exp}-\lambda_{mod})/\lambda_{exp}$ [%]
0.5	0.05	0.048	4
1	0.092	0.088	4.4
2	0.179	0.172	3.9

4.6.3 Uniform velocity and log-normal droplet size distribution

In this last case a combination of the two previous conditions is analyzed.

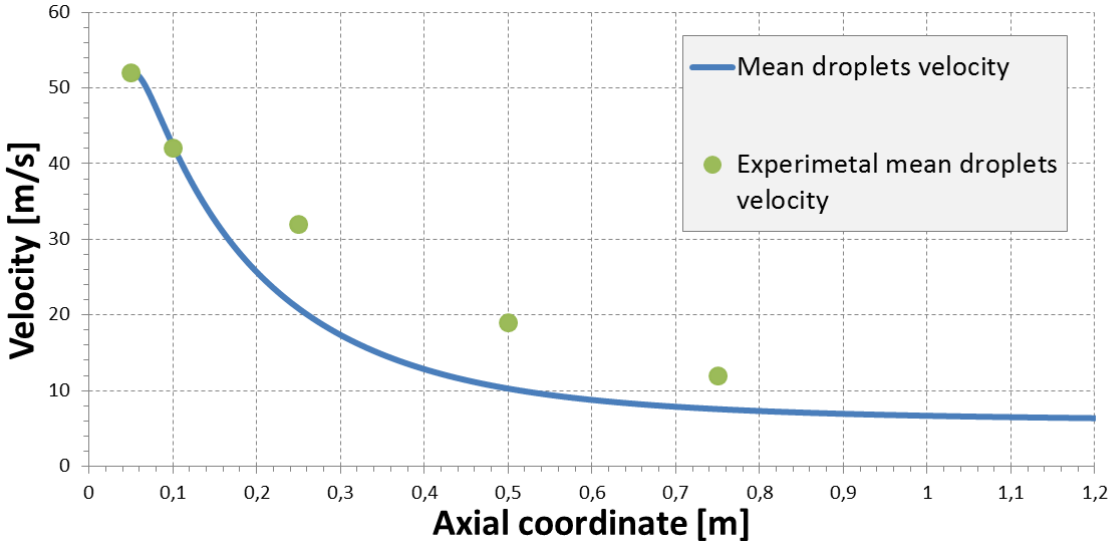

Figure 82: sensitivity analysis, mean droplet velocity evolution with uniform inlet velocity and log-normal size distribution as input

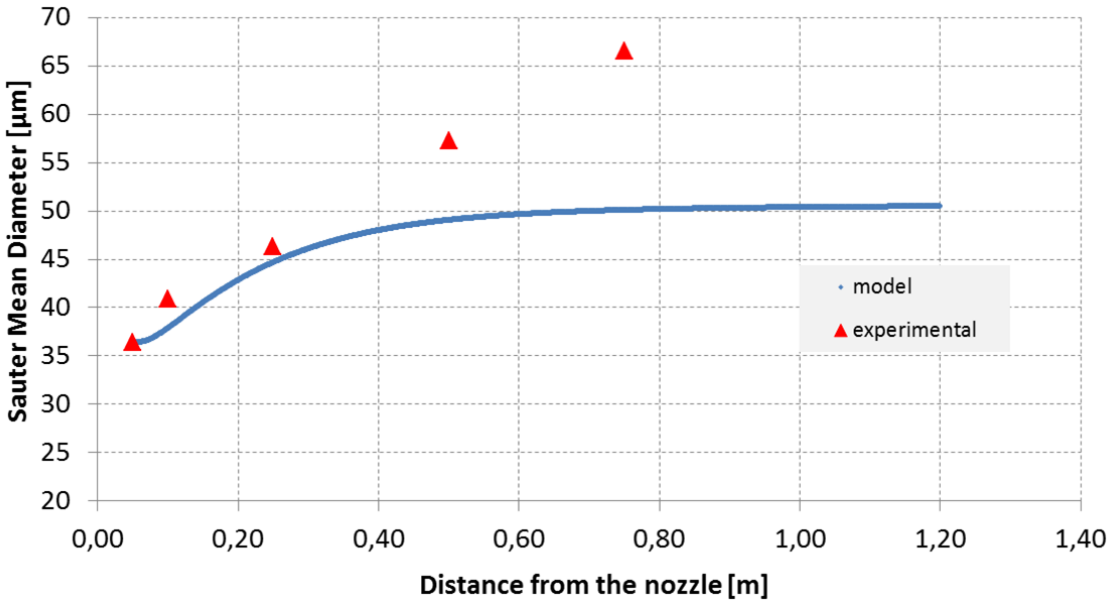

Figure 83: sensitivity analysis, Sauter mean diameter evolution with uniform inlet velocity and log-normal droplet size distribution as input

Table 15: sensitivity analysis, decontamination coefficient λ with uniform inlet velocity and log-normal droplet size distribution as input

Dp [μm]	λ_{exp} [1/s]	λ_{mod} [1/s]	$(\lambda_{exp}-\lambda_{mod})/\lambda_{exp}$ [%]
0.5	0.05	0.041	18.0
1	0.092	0.072	21.7
2	0.179	0.138	22.9

As we can see this is the worst case, where the effect of the two assumptions on the decontamination prevision sum, leading toward incorrect values.

It is clear that the assumption of uniform inlet velocity is far away from the experimental results and highly influences the final results.

On the other hand, the generalized log-normal distribution gives very similar results with our experimental data, which could be used as generalized input for the model.

5 Comparisons and conclusions

5.1 Comparison between low and high pressure spray systems

As first comparison between low and high pressure sprays, the half-life time obtained with a pressure of 50 bar will be compared with the results obtained in the TOSCANQ experiments (Porcheron et. al 2010) because the volumetric flow rate if the two experiments are comparable, $13*10^{-6}$ versus $10*10^{-6}$ m^3 s^{-1}.

Table 16 show that the difference between the decontamination half-life times is more than one order of magnitude.

Table 16: comparison between TOSQAN and SCRUPOS experimental half-life time

Particulate size [µm]	TOSCANQ half-life time [s]	SCRUPOS half-life time [s]
0.5	1200	28.1
1	900	16.5
2	500	6.7

In order to have a more correct comparison, the applicability of the Postma equation to SCRUPOS results is analysed.

As seen in section 1.3, the Postma equation (Postma 1978) $\lambda = \frac{3}{2}\frac{Q_{volumic}*h}{D_{droplet}*V_{containment}}E$ could provide a prevision of the decontamination coefficient of a droplets of a certain dimension that has a fall height of h.

The SCRUPOS facility has a volume of 0.75 m^3 and the droplets have a fall height of 1.2 m. The other input for Postma equation are taken from the measurement on the spray illustrated in section 3.4.3 and resumed in the table below:

Water pressure [bar]	Water flow rate [m^3 s^{-1}]	Droplet diameter [µm]	Droplet velocity [m s^{-1}]
50	13e-06	61	17
100	19e-06	44	24
130	22e-06	38	27

In Figure 84,Figure 85 Figure 86 are reported the decontamination coefficients λ obtained in our experimental measurements, with our model and the value calculated according to Postma equation. Postma equation can provide a good initial prevision for the decontamination coefficient λ. It underestimates the decontamination at 50 and 100 bar but in the case of 130 bar the result are very close to the experimental one.

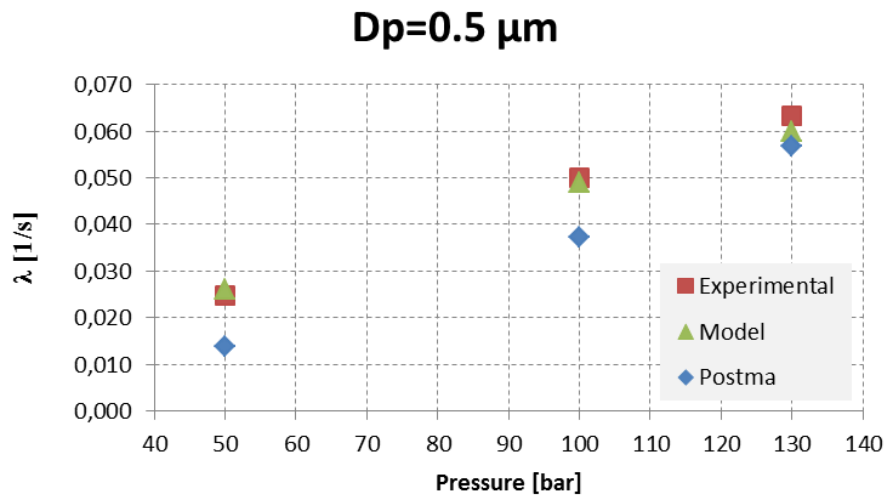

Figure 84: comparison between λ coefficients for 0.5 µm aerosol

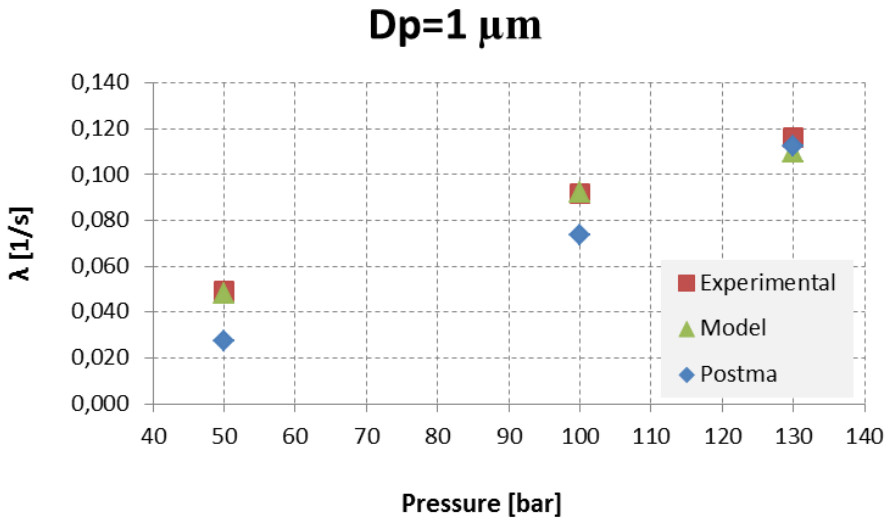

Figure 85: comparison between λ coefficients for 1 µm aerosol

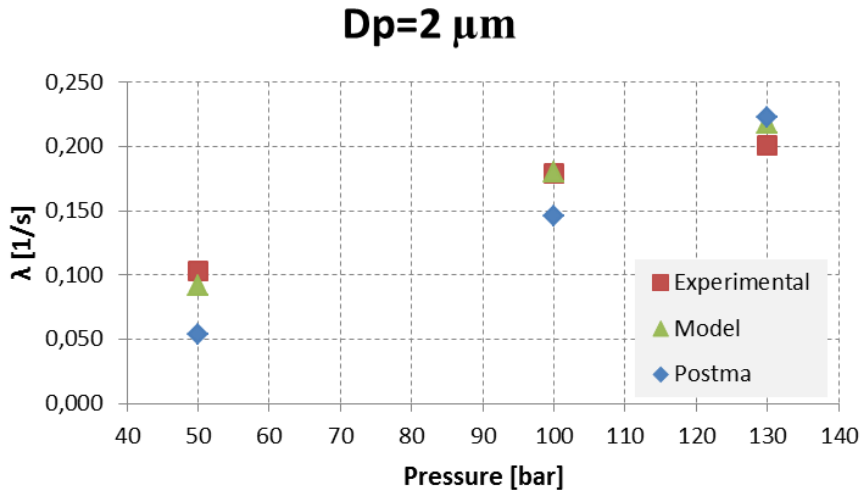

Figure 86: comparison between λ coefficients for 2 µm aerosol

In order to extract a result that is not function of the single experimental configuration the efficiency term $\frac{E}{D_w}$ is considered from the Postma equation.

$$\frac{E}{D_w} = \frac{2\lambda V_{containment}}{3hQ_{volumetric}} \qquad 5.1$$

The value of λ for TOSQAN experiments is obtained from the inverse formula for calculation of the half-life time:

$$\lambda = -\frac{\ln(0.5)}{Half - life\ time}$$

Comparison between the results of the two spray configurations are illustrated in Table 17

Table 17: comparison between the efficiency of low and high pressure spray sistem

Particulate size [μm]	E/Dw TOSCANQ	E/Dw SCRUPOS
0.5	68	1186
1	90	2179
2	162	3755

5.2 Conclusions

The aim of this work was to put in evidence the decontamination performances of high pressure spray systems and to develop a model that can predict their aerosol removal rate. The collection of experimental data provided an extensive understanding of the mechanics involved in the decontamination process.

It has been highlighted that to obtain a more intense removal of aerosol finer droplets and higher velocities are needed.

High pressure water sprays have proven to provide much higher decontamination performances than conventional sprays used in current nuclear power plants and, for this reason, further investigations on their use should be performed because this technology is already quite mature and commercially available.

5.3 Future development

During the modelling work the necessity of a deeper comprehension of the agglomeration processes and on the mutual droplet interaction has been highlighted.

It would be useful to evaluate the performances of different kind of spray nozzle and with a polydisperse aerosol.

Bibliografy

Albrecht H. E., Damaschke N., Borys M. and Tropea C., *Laser Doppler and Phase Doppler Measurement Techniques*, Springer 2003, XIV, ISBN: 3-540-67838-7;

Allen E., Smith P. and Henshaw J. 2001. A review of particle agglomeration. AEA TECHNOLOGY, US Department of Energy;

Aplisens: www.aplisens.com/pressure-transmitter-model-pce-28.html;

Araneo L., Damaschke N., Tropea C. 2000, *Measurement and Prediction of the Gaussian Beam Effect in the Phase Doppler Technique*, 10th International Symposium on Application of Laser Based Techniques to fluid Mechanics, Lisbon;

Baker L. Jr, Pilch M. and Tarbell W. W. 1988, Droplet Structure Interactions in Direct Containment Heating Proc. ANS/ENS International Meeting;

Brooks® 2010, Mass Flow Controller Model SLA5853S, Installation and Operation Manual;

Casella F. 2014, High Pressure Spray: Experimental Study on Aerosol–Droplets Interaction and Modeling;

ECART User's Manual 2011 (Enel Code for Analysis of Radionuclide Transport);

Lefebvre A. 1988, Atomization and Sprays, CRC Press;

Emekwuru N.G. 2012, Hydrodynamics - Theory and Model. Capther 4: Using the General Gamma Distribution to Represent the Droplet Size Distribution in a Spray Model. pp.79-94;

Fuchs N.A. 1964. The Mechanics of Aerosols, Pergamon Press, Oxford;

Fermandjian J. 1984, Comportement des aérosols dans l'enceinte de Confinement, SFRP - Meeting on mitigation and confinement of radioactive products in water cooled reactors, Saclay, 1984;

Kadocsa A., Tatschl R., Kristóf G. 2007, Analysis of spray evolution in internal combustion engines using numerical simulation, Journal of Applied Mathematics and Computational Mechanics 8, p.5;

Lehtinen K. E. J. 1997. Theoretical studies on aerosol agglomeration processes. Technical Research Centre of Finland, VTT Publications 304;

Mahmud H.M.I., Moinuddin K.A.M. and Thorpe G.R. 2012. Characterization of a water-mist spray: Numerical modelling and experimental validation. Centre for Environmental Safety and Risk Engineering Victoria University. 18th Australasian Fluid Mechanics Conference Launceston, Australia 3-7 December 2012;

Mugele R.A., Evans H.D. 1951. Droplet Size Distribution in Sprays, Industrial & Engineering Chemistry, American Chemical Society, pp. 1317-1324;

Nukiyama S., Tanasawa Y., Tans. Soc. Of Mech. Engrs. 4, 5 and 6 (Japan);

Pemberton C. S. 1960, J. Air Pollution 3 ,pp. 168;

Perkins R.J., "Aerosol Transport, Deposition and Resuspension in the LWR Circuit and Containment", Contract No. 4120 90-10 ED ISP GB, Interim Report No. 2, Dept of Applied Mathematics and Theoretical Physics, University of Cambridge;

Porcheron E., Lemaitre P., Marchand D., Nuboer A. and Vendel J. 2008, Experimental and numerical approaches of aerosols removal in spray for nuclear reactor containment application, 6th International Conference on Heat Transfer, Fluid Mechanics and Thermodynamics, Pretoria, South-Africa, paper number: PE1;

Porcheron E., Lemaitre P. and Marchand D. 2010, Aerosol Removal by Emergency Spray in PWR Containment, Journal of Energy and Power Engineering 5 (2011) 600-611;

Postma A. K., Sherry R. R. and Tam P. S. 1978, Technological bases for models of spray washout of airborne contaminants in containment vessels. NUREG/CR-0009, Nuclear Regulatory Commission, Office of Nuclear Reactor Regulation, Division of Site Safety and Environmental Analysis, Accident Analysis Branch;

Powers D.A., Burson S.B. 1993. A Simplified Model of Aerosol Removal by Containment Sprays, NUREG/CR-5966, SAND92-268;

Pruppacher H.R., Beard R.V. 1970, Quarterly J. R. Meteorological Society 96, pp.247;

Pruppacher H.R., Klett J.D. 1997, Microphysics of clouds and precipitations, atmospheric and oceanographic sciences library, volume 18

Rosin P., Rammler E. 1933. The Laws Governing the Fineness of Powder Coal, Journal of the Institute of Fuel 7, pp. 29-36;

Saffman M., Buchhave P. and Tanger H. 1984, *Simultaneous Measurement of Size, Concentration, and Velocity of Spherical Particles by a Laser Doppler Method* in Proceedings of the Second International Symposium on Applications of Laser Anemometry to Fluid Mechanics, Lisbon Portugal paper 8.1;

Saffman M. 1987, Automatic calibration of LDA measurement volume size Appl. Opt. 26 2592–7;

Spengler J. D. and Gokhale N. R. 1973, Applied Meteorology 12, pp.31;

Willeke K., Baron P.A., Aerosol Measurements: principles, techniques and applications, Van Nostrand Reinhold New York;

Topas GmbH 2013, Dynamic Dilution System DDS 560, Instruction Manual;

Topas GmbH 2005, Solid Aerosol Generator Series SAG 410, Instruction manual;

TSI 2010,Optical Particle Sizer (OPS) Spectrometers Model 3330, User's Manual;

Appendix A: complete spray measurement results

50 bar

Z [mm]	X [mm]	Y [mm]	D 10 [µm]	D 20 [µm]	D 30 [µm]	D 32 [µm]	Vax [m/s]	Count	Data Rate [#/s]
50	0	-15	42.09	46.69	50.91	61.26	25.98	9282	1857.35
50	0	-12.5	37.01	41.60	46.12	57.33	28.31	22009	4402.53
50	0	-10	34.45	38.56	42.86	53.52	36.83	40508	8101.82
50	0	-7.5	33.26	36.91	40.90	50.80	45.03	50096	10019.41
50	0	-5	25.52	29.83	34.48	46.57	49.35	44794	8959.07
50	0	-2.5	20.29	23.86	27.74	37.89	48.46	39091	7819.02
50	0	0	19.34	22.84	26.78	37.17	47.23	41274	8255.04
50	0	2.5	22.81	26.96	31.47	43.33	47.44	50472	10095.08
50	0	5	26.38	31.11	36.44	50.56	44.67	58824	11765.53
50	0	7.5	27.31	31.65	36.65	49.65	36.49	58642	11729.13
50	0	10	29.60	33.77	38.50	50.61	28.86	43284	8657.50
50	0	12.5	34.86	39.06	43.72	55.40	25.53	21064	4214.18
50	0	15	40.54	44.37	48.39	58.25	24.06	8408	1681.82
50	-15	0	37.45	43.09	48.35	61.59	24.25	15197	3040.53
50	-12.5	0	31.88	37.28	42.63	56.39	26.69	36725	7346.16
50	-10	0	29.57	34.18	38.83	50.65	33.78	61335	12267.37
50	-7.5	0	30.39	34.40	38.82	49.99	42.67	61095	12219.64
50	-5	0	29.45	32.78	36.67	46.39	48.76	62356	12471.40
50	-2.5	0	26.52	29.25	32.75	41.51	48.88	51436	10287.82
50	0	0	24.59	26.76	29.41	35.87	47.32	43523	8705.08
50	2.5	0	25.42	27.45	29.75	35.30	47.31	42610	8522.18
50	5	0	29.48	32.14	35.31	43.07	47.87	47270	9454.55
50	7.5	0	34.18	37.73	41.59	51.09	44.65	48898	9780.01
50	10	0	35.70	39.89	44.23	54.99	34.77	41724	8346.08
50	12.5	0	39.67	44.31	48.75	59.72	28.52	21850	4370.45
50	15	0	46.30	50.52	54.42	63.90	26.83	7623	1524.71
100	0	-30	61.59	65.08	68.64	77.34	14.28	481	96.72
100	0	-25	50.71	55.44	59.96	71.02	12.88	1794	359.22
100	0	-20	42.16	47.77	53.01	66.04	13.34	5441	1088.44
100	0	-15	35.23	40.57	45.97	59.73	20.40	18698	3740.35
100	0	-10	33.95	38.07	42.26	52.66	30.21	30922	6184.97
100	0	-5	29.04	31.68	34.60	41.71	36.10	35314	7063.47
100	0	0	25.38	27.15	28.98	33.35	36.49	37041	7408.50
100	0	5	26.89	29.48	32.33	39.27	34.46	41493	8299.22
100	0	10	30.45	34.53	38.90	49.89	31.05	42995	8599.15
100	0	15	31.18	36.65	42.32	57.06	20.90	31989	6398.30
100	0	20	37.52	44.19	50.48	66.65	14.59	11037	2208.23
100	0	25	53.81	59.02	63.55	74.61	15.72	2255	451.80
100	0	30	65.56	69.32	72.74	81.12	17.38	635	128.44
100	-30	0	61.40	65.74	69.57	78.91	16.36	758	152.50
100	-25	0	54.26	59.42	63.91	74.87	16.39	2562	512.72
100	-20	0	35.58	42.21	48.43	64.49	15.14	13029	2606.39
100	-15	0	29.14	34.69	40.28	54.94	21.40	37826	7565.42
100	-10	0	28.93	32.88	37.24	48.30	32.87	49183	9837.86
100	-5	0	27.04	29.61	32.48	39.49	37.03	43551	8710.73
100	0	0	25.50	27.28	29.06	33.33	36.36	37290	7458.26
100	5	0	26.87	29.01	31.26	36.69	35.23	34760	6952.96
100	10	0	32.37	35.91	39.58	48.60	32.15	30972	6194.69
100	15	0	36.10	41.20	46.21	58.79	22.95	22337	4467.71
100	20	0	40.47	46.26	51.58	64.89	16.39	8581	1716.34
100	25	0	53.62	58.89	63.54	74.90	16.27	1934	387.47
100	30	0	60.57	65.00	68.82	78.14	16.06	514	103.33

Z [mm]	X [mm]	Y [mm]	D 10 [µm]	D 20 [µm]	D 30 [µm]	D 32 [µm]	Vax [m/s]	Count	Data Rate [#/s]
250	0	-60	75.13	78.68	80.97	86.89	1.96	219	22.99
250	0	-50	57.79	63.97	68.62	79.97	2.13	979	98.11
250	0	-40	42.09	48.94	54.80	69.56	4.10	4787	479.49
250	0	-30	37.61	44.27	50.37	65.98	8.41	11797	1179.84
250	0	-20	35.70	41.61	47.43	62.34	14.53	24030	2403.14
250	0	-10	32.71	36.92	41.32	52.34	21.79	39750	3975.05
250	0	0	31.07	33.91	36.62	43.17	24.38	51815	5181.72
250	0	10	29.99	34.09	38.16	48.34	20.83	49351	4935.31
250	0	20	32.65	38.86	45.20	61.85	15.67	33494	3349.69
250	0	30	33.38	40.81	47.95	66.99	9.51	15328	1533.46
250	0	40	38.17	47.11	55.11	76.32	4.79	3269	327.12
250	0	50	44.36	52.64	59.43	76.69	3.07	1001	101.59
250	0	60	59.45	67.28	73.12	87.48	2.14	151	15.31
250	-60	0	61.91	69.95	75.66	89.67	2.77	291	29.16
250	-50	0	41.33	49.55	56.42	74.03	3.66	2681	268.18
250	-40	0	39.30	46.84	53.69	71.41	6.54	8001	800.12
250	-30	0	38.50	44.56	50.54	65.78	11.42	23277	2327.75
250	-20	0	36.11	40.99	45.98	58.54	19.31	44115	4411.53
250	-10	0	32.23	35.77	39.37	48.24	23.72	53401	5340.32
250	0	0	28.70	31.63	34.42	41.17	24.21	48470	4847.12
250	10	0	34.28	37.37	40.37	47.66	22.40	38427	3842.79
250	20	0	40.27	44.53	48.79	59.25	18.67	27093	2709.66
250	30	0	44.74	50.28	55.71	69.22	11.69	13313	1331.38
250	40	0	44.11	50.72	56.88	72.41	6.81	5695	570.19
250	50	0	49.33	57.86	65.22	83.93	3.66	979	97.97
250	60	0	67.50	78.34	85.13	101.88	4.23	80	8.20
500	0	-90	70.20	78.04	83.78	97.85	1.26	605	30.56
500	0	-75	57.68	66.38	73.71	92.09	2.68	2072	103.85
500	0	-60	51.77	60.27	67.73	86.63	3.61	3435	171.85
500	0	-45	46.27	54.65	62.61	83.17	6.22	7620	381.17
500	0	-30	44.28	51.99	59.34	78.24	7.74	9478	474.25
500	0	-15	39.58	46.56	53.34	70.84	12.68	22196	1109.82
500	0	0	37.70	43.93	49.80	64.74	14.56	36308	1815.45
500	0	15	36.34	42.49	48.31	63.18	14.53	34315	1715.84
500	0	30	36.51	43.63	50.59	68.84	12.55	27049	1352.51
500	0	45	36.00	43.77	51.43	71.83	9.31	16976	848.89
500	0	60	35.81	44.11	52.70	76.12	8.00	11412	570.88
500	0	75	37.44	45.86	54.25	76.83	4.35	3897	195.00
500	0	90	37.76	46.24	54.70	77.45	3.10	1858	93.17
500	-90	0	47.52	57.80	66.22	88.03	1.61	384	19.47
500	-75	0	36.00	43.88	51.70	72.62	4.63	6069	303.50
500	-60	0	36.80	45.16	53.34	75.32	6.34	9706	485.48
500	-45	0	34.26	42.09	50.08	71.75	9.43	17195	859.82
500	-30	0	37.81	45.37	52.75	72.16	12.13	24544	1227.33
500	-15	0	37.65	44.43	51.01	68.01	14.09	32198	1610.01
500	0	0	36.85	42.89	48.54	62.93	15.17	33588	1679.43
500	15	0	39.86	46.48	52.89	69.30	13.09	23630	1181.55
500	30	0	42.45	50.00	57.30	76.16	10.55	15310	765.59
500	45	0	45.92	54.58	62.83	84.29	7.20	7724	386.33
500	60	0	44.44	52.86	60.95	82.05	5.09	4130	206.65
500	75	0	51.74	61.57	70.20	92.43	2.80	1506	75.43
500	90	0	56.89	66.14	73.81	93.09	1.42	323	16.20

Z [mm]	X [mm]	Y [mm]	D 10 [µm]	D 20 [µm]	D 30 [µm]	D 32 [µm]	Vax [m/s]	Count	Data Rate [#/s]
750	0	-120	48.88	60.11	69.96	95.97	2.00	565	28.61
750	0	-100	44.65	53.90	62.51	85.13	3.23	1287	64.47
750	0	-80	44.13	53.37	61.79	83.87	3.92	2346	117.61
750	0	-60	41.87	50.86	59.46	82.28	6.70	5380	269.08
750	0	-40	41.86	50.53	59.08	81.74	8.03	7560	378.44
750	0	-20	42.44	51.25	59.60	81.61	9.77	12270	613.54
750	0	0	42.22	51.04	59.26	80.88	10.22	14017	701.03
750	0	20	42.19	50.60	58.40	78.73	9.86	12345	617.44
750	0	40	39.41	49.07	58.17	82.75	7.72	9099	455.34
750	0	60	37.67	48.11	58.35	86.88	5.84	5365	268.30
750	0	80	36.94	47.45	57.38	84.96	5.02	4232	211.72
750	0	100	34.24	43.98	53.13	78.47	3.53	1678	84.01
750	0	120	35.94	46.60	56.16	82.55	2.12	509	25.73
750	-120	0	35.49	45.66	55.16	81.46	2.26	626	32.14
750	-100	0	33.53	42.74	51.67	76.42	3.70	2292	114.84
750	-80	0	34.27	43.62	52.73	77.95	4.93	3624	181.29
750	-60	0	36.64	45.41	54.13	77.87	7.29	7996	399.93
750	-40	0	41.46	50.97	60.09	84.53	8.52	10534	526.77
750	-20	0	44.16	52.99	61.13	82.36	9.83	12130	606.81
750	0	0	45.50	54.27	62.40	83.53	9.60	11454	572.76
750	20	0	45.91	55.28	63.99	86.84	8.62	9214	460.71
750	40	0	45.23	54.66	63.61	87.23	7.36	6528	326.48
750	60	0	45.08	55.10	64.56	89.75	6.57	5406	271.17
750	80	0	43.56	53.36	62.74	87.80	5.37	3899	195.06
750	100	0	46.05	56.46	65.98	91.23	3.10	1686	84.43
750	120	0	49.87	62.46	73.05	101.22	1.88	445	22.30

80 bar

Z [mm]	X [mm]	Y [mm]	D 10 [µm]	D 20 [µm]	D 30 [µm]	D 32 [µm]	Vax [m/s]	Count	Data Rate [#/s]
50	0	-15	40.94	43.29	45.37	50.40	29.36	1574	315.09
50	0	-12.5	37.60	40.42	43.38	50.54	30.54	5778	1155.85
50	0	-10	34.52	37.37	40.26	47.23	35.07	13985	2797.23
50	0	-7.5	34.32	37.10	40.06	47.22	47.41	15432	3086.91
50	0	-5	34.54	37.61	41.32	50.43	68.94	14328	2866.77
50	0	-2.5	30.80	34.09	38.44	49.44	74.24	10019	2004.13
50	0	0	25.40	28.21	31.83	40.96	71.50	5205	1041.67
50	0	2.5	27.26	30.00	33.35	41.66	70.49	9855	1971.68
50	0	5	30.90	33.79	37.31	45.98	65.43	23950	4790.42
50	0	7.5	30.23	33.05	36.33	44.36	47.74	46264	9253.30
50	0	10	28.33	31.50	34.58	42.10	32.34	59883	11977.49
50	0	12.5	30.89	34.29	37.34	44.76	27.77	30790	6158.40
50	0	15	35.33	38.50	41.36	48.26	26.86	9849	1970.10
50	-15	0	34.36	37.58	40.58	47.84	26.34	8466	1694.94
50	-12.5	0	28.37	32.08	35.52	44.01	28.33	33356	6671.70
50	-10	0	25.72	29.15	32.49	40.79	34.63	56324	11265.00
50	-7.5	0	20.04	26.13	30.49	41.97	37.14	47425	9485.94
50	-5	0	29.90	33.07	37.07	47.09	70.88	24989	4998.07
50	-2.5	0	28.26	31.74	36.24	47.76	77.05	12255	2451.74
50	0	0	25.31	28.25	31.90	41.11	72.34	6172	1235.19
50	2.5	0	25.47	27.81	30.61	37.48	70.51	6859	1372.38
50	5	0	31.43	34.07	37.16	44.69	68.94	10547	2109.56
50	7.5	0	35.78	38.64	41.75	49.31	55.73	10907	2181.57
50	10	0	33.88	36.52	39.13	45.40	36.35	25802	5160.76
50	12.5	0	36.97	39.49	41.79	47.31	30.99	14241	2848.77
50	15	0	40.87	43.18	45.31	50.47	29.57	3574	714.89
100	0	-30	53.58	55.63	57.42	61.92	15.37	91	19.32
100	0	-25	50.84	52.83	54.57	58.94	13.55	425	85.52
100	0	-20	41.72	44.28	46.50	51.85	11.64	2222	444.66
100	0	-15	37.61	40.49	43.04	49.20	17.01	6648	1330.10
100	0	-10	38.33	41.15	44.07	51.12	34.95	13290	2658.82
100	0	-5	35.54	38.05	40.84	47.56	50.02	13916	2783.31
100	0	0	28.02	29.63	31.15	34.80	50.06	11206	2241.36
100	0	5	29.17	31.07	32.90	37.27	47.90	19955	3991.59
100	0	10	32.25	34.99	37.77	44.49	39.59	39142	7829.08
100	0	15	29.76	33.25	36.53	44.58	21.62	36392	7278.83
100	0	20	32.50	36.68	40.14	48.61	12.84	10432	2086.93
100	0	25	45.75	48.90	51.62	58.22	13.34	1845	370.03
100	0	30	49.66	51.81	53.59	58.04	14.08	589	118.04
100	-30	0	49.65	51.52	52.99	56.73	13.41	524	105.49
100	-25	0	41.81	45.10	47.60	53.63	12.62	2630	526.16
100	-20	0	27.41	31.43	35.05	44.06	12.50	20922	4185.20
100	-15	0	27.59	31.05	34.38	42.59	23.94	46943	9389.00
100	-10	0	32.18	34.91	37.71	44.48	44.42	36117	7223.88
100	-5	0	30.02	32.04	34.21	39.42	51.56	20271	4055.00
100	0	0	28.13	29.96	32.09	37.20	50.96	11079	2215.92
100	5	0	31.43	33.17	34.84	38.86	48.84	9457	1892.12
100	10	0	39.90	42.53	45.13	51.41	43.31	9772	1954.74
100	15	0	39.44	42.22	44.84	51.17	24.35	10419	2084.26
100	20	0	42.33	45.07	47.43	53.14	15.69	3812	763.04
100	25	0	50.90	53.02	54.72	59.01	15.84	645	129.26
100	30	0	54.85	56.63	58.20	62.25	16.13	142	28.65

Z [mm]	X [mm]	Y [mm]	D 10 [µm]	D 20 [µm]	D 30 [µm]	D 32 [µm]	Vax [m/s]	Count	Data Rate [#/s]
250	0	-60	55.05	56.52	57.84	61.33	1.89	17	1.82
250	0	-50	49.58	52.26	54.39	59.61	1.45	182	18.53
250	0	-40	48.05	50.79	53.20	59.05	3.60	886	88.93
250	0	-30	46.73	49.65	52.59	59.71	8.71	2795	279.67
250	0	-20	42.82	45.79	48.61	55.41	16.77	8355	835.58
250	0	-10	42.53	45.42	48.24	55.05	27.25	19942	1994.42
250	0	0	39.59	41.79	43.85	48.82	32.80	35604	3560.52
250	0	10	38.69	41.08	43.39	48.93	31.36	39408	3940.94
250	0	20	36.44	39.80	43.06	50.99	23.37	31093	3109.55
250	0	30	32.30	36.03	39.74	48.88	14.77	15782	1578.56
250	0	40	32.45	36.41	40.48	50.57	7.82	4893	489.54
250	0	50	33.98	38.17	42.09	51.77	3.52	1203	120.61
250	0	60	40.68	45.30	49.15	58.56	1.92	132	13.42
250	-60	0	41.84	46.32	50.20	59.66	1.64	235	23.59
250	-50	0	35.82	40.06	43.92	53.39	3.74	2207	220.92
250	-40	0	34.64	38.75	42.56	51.94	7.69	8211	821.47
250	-30	0	34.34	38.29	42.08	51.38	14.64	20129	2013.13
250	-20	0	36.81	40.39	43.78	52.00	23.87	37372	3737.40
250	-10	0	40.28	42.88	45.38	51.43	31.67	43435	4343.65
250	0	0	40.67	42.89	45.03	50.22	32.59	32089	3209.06
250	10	0	44.53	46.96	49.30	54.96	29.38	17969	1797.09
250	20	0	45.98	48.99	51.79	58.57	21.79	9895	989.87
250	30	0	44.48	47.50	50.24	56.86	13.83	4380	438.53
250	40	0	42.18	45.21	48.14	55.22	7.87	1755	175.66
250	50	0	42.89	45.85	48.66	55.45	3.41	302	30.69
250	60	0	44.94	48.38	51.37	58.61	1.46	19	2.05
500	0	-90	56.40	59.68	62.58	69.65	1.87	337	16.88
500	0	-75	56.55	59.62	62.34	69.00	3.31	1102	55.30
500	0	-60	55.31	58.70	61.72	69.09	4.99	1785	89.37
500	0	-45	55.38	58.69	61.71	69.09	6.28	2967	148.40
500	0	-30	54.40	57.76	60.86	68.42	10.54	6435	322.08
500	0	-15	53.73	57.02	60.07	67.51	14.41	11129	556.51
500	0	0	53.26	56.42	59.33	66.42	18.93	21526	1076.34
500	0	15	52.09	55.20	58.04	64.95	19.31	26587	1329.64
500	0	30	49.31	52.85	56.16	64.20	17.00	24000	1200.08
500	0	45	48.03	51.67	55.09	63.38	13.55	15184	759.43
500	0	60	46.76	50.65	54.47	63.74	9.97	9046	452.32
500	0	75	43.70	47.70	51.51	60.79	5.04	3046	152.57
500	0	90	45.29	49.64	53.73	63.71	3.05	1130	56.80
500	-90	0	44.19	49.05	53.46	64.29	2.86	2512	125.86
500	-75	0	42.53	47.22	51.69	62.68	5.22	5802	290.35
500	-60	0	42.23	46.64	50.82	61.07	7.66	9633	481.75
500	-45	0	43.93	48.06	52.02	61.67	11.83	16141	807.08
500	-30	0	47.77	51.69	55.38	64.33	15.97	21602	1080.12
500	-15	0	50.49	54.15	57.58	65.90	18.54	25835	1291.84
500	0	0	51.46	54.74	57.72	64.95	18.38	21585	1079.47
500	15	0	53.59	56.99	60.23	68.09	15.42	13140	657.06
500	30	0	53.97	57.55	60.83	68.80	11.88	7988	399.64
500	45	0	50.97	54.55	58.01	66.40	9.74	5999	300.18
500	60	0	50.50	53.96	57.12	64.81	6.74	3114	155.77
500	75	0	50.70	54.13	57.27	64.90	4.12	980	49.09
500	90	0	53.44	57.04	60.24	68.00	2.09	254	12.77

Z [mm]	X [mm]	Y [mm]	D 10 [µm]	D 20 [µm]	D 30 [µm]	D 32 [µm]	Vax [m/s]	Count	Data Rate [#/s]
750	0	-120	61.95	66.52	70.41	79.88	1.41	180	9.47
750	0	-100	56.63	60.84	64.59	73.71	3.20	695	34.83
750	0	-80	54.38	58.89	62.98	72.92	5.89	2438	122.06
750	0	-60	54.73	59.27	63.44	73.57	7.46	3255	162.92
750	0	-40	53.88	58.35	62.46	72.48	9.28	4678	233.98
750	0	-20	56.10	60.67	64.80	74.86	11.79	7943	397.33
750	0	0	56.56	61.07	65.21	75.29	12.89	10407	520.64
750	0	20	55.51	60.24	64.50	74.89	13.00	11197	559.87
750	0	40	51.69	56.60	61.08	72.02	11.25	8850	442.52
750	0	60	47.65	52.75	57.50	69.17	9.24	6477	324.12
750	0	80	45.08	50.28	55.18	67.25	7.37	4564	228.28
750	0	100	45.12	50.58	55.83	68.83	4.98	2210	110.67
750	0	120	45.21	50.16	54.79	66.17	5.35	2083	104.51
750	-120	0	44.82	50.30	55.40	68.02	4.11	2338	116.94
750	-100	0	46.26	51.53	56.43	68.51	5.78	3431	171.61
750	-80	0	47.01	51.92	56.41	67.41	6.64	3774	188.88
750	-60	0	49.07	53.76	58.07	68.60	7.44	3631	181.65
750	-40	0	50.72	55.48	59.92	70.75	9.29	4879	244.24
750	-20	0	54.65	59.15	63.26	73.28	10.87	6340	317.02
750	0	0	54.91	59.52	63.83	74.34	9.97	4957	248.05
750	20	0	54.29	58.91	63.11	73.34	7.81	3202	160.34
750	40	0	53.65	58.51	63.04	74.09	7.35	2798	140.05
750	60	0	52.46	57.07	61.34	71.72	5.79	2047	102.43
750	80	0	55.82	61.00	65.78	77.47	2.42	493	24.85
750	100	0	54.00	58.51	62.16	71.05	1.36	164	8.27
750	120	0	51.40	56.73	61.14	71.90	0.39	30	1.82

100 bar

Z [mm]	X [mm]	Y [mm]	D 10 [µm]	D 20 [µm]	D 30 [µm]	D 32 [µm]	Vax [m/s]	Count	Data Rate [#/s]
50	0	-15	40.43	42.22	43.72	47.43	29.13	689	137.97
50	0	-12.5	39.55	41.48	43.09	47.04	31.84	2168	433.99
50	0	-10	37.44	39.41	41.11	45.24	36.22	4859	972.00
50	0	-7.5	36.39	38.86	42.02	49.67	46.96	3570	714.77
50	0	-5	36.07	39.80	44.63	56.74	73.64	2159	432.14
50	0	-2.5	34.30	38.06	41.99	51.68	85.04	1046	209.36
50	0	0	28.38	32.02	35.74	45.03	85.03	379	76.30
50	0	2.5	30.60	33.70	36.83	44.47	80.88	1207	241.61
50	0	5	33.52	36.48	39.47	46.74	73.11	5332	1067.56
50	0	7.5	31.11	33.16	35.19	40.06	47.47	23957	4792.33
50	0	10	30.04	32.26	34.24	38.97	31.31	52178	10436.02
50	0	12.5	32.43	34.87	36.97	42.02	27.33	24056	4812.34
50	0	15	35.71	37.98	39.90	44.52	26.26	7157	1432.41
50	-15	0	34.69	37.03	39.01	43.78	27.84	8770	1754.15
50	-12.5	0	29.08	31.75	34.13	39.85	29.79	37224	7445.46
50	-10	0	26.63	28.97	31.05	36.04	36.27	53843	10769.24
50	-7.5	0	28.33	30.48	32.56	37.53	53.74	25212	5043.13
50	-5	0	30.96	34.28	38.57	49.34	77.57	6719	1344.81
50	-2.5	0	30.24	33.84	38.54	50.53	85.85	1773	355.20
50	0	0	26.34	29.55	32.75	40.64	82.94	533	106.69
50	2.5	0	28.49	31.77	34.87	42.47	84.24	418	83.90
50	5	0	38.35	44.35	54.43	82.97	87.84	704	140.93
50	7.5	0	37.37	41.45	46.03	57.40	69.64	1177	235.43
50	10	0	37.44	39.41	41.34	45.98	38.52	6169	1234.07
50	12.5	0	39.70	41.56	43.09	46.84	33.71	6079	1215.98
50	15	0	42.17	43.85	45.20	48.59	31.94	1439	288.38
100	0	-30	53.38	54.51	55.56	58.43	13.90	39	8.00
100	0	-25	48.86	50.18	51.64	55.35	11.22	182	36.69
100	0	-20	40.05	41.58	42.87	46.10	10.45	1252	250.72
100	0	-15	39.52	41.44	43.60	48.84	15.90	2493	498.74
100	0	-10	40.69	42.71	44.57	49.11	34.02	3336	667.48
100	0	-5	38.69	40.87	43.09	48.43	54.64	3178	635.68
100	0	0	30.98	32.77	34.38	38.24	56.86	2108	422.48
100	0	5	32.87	34.88	37.10	42.43	53.38	5381	1076.27
100	0	10	34.45	36.67	38.84	44.08	41.44	19093	3819.38
100	0	15	30.28	32.70	34.84	39.99	20.09	26941	5388.33
100	0	20	30.02	33.10	35.81	42.36	10.64	9110	1823.04
100	0	25	37.97	41.19	43.69	49.70	9.70	1350	270.46
100	0	30	45.89	47.94	49.68	53.99	11.26	250	50.30
100	-30	0	44.71	46.46	47.77	51.10	10.36	415	83.08
100	-25	0	34.12	37.15	39.58	45.43	9.09	3345	669.41
100	-20	0	27.52	30.33	32.84	38.89	12.08	22158	4431.79
100	-15	0	28.41	30.77	32.90	38.01	25.59	42514	8503.84
100	-10	0	32.63	34.91	37.15	42.54	47.09	24289	4859.79
100	-5	0	32.86	34.98	37.14	42.33	58.34	7066	1413.39
100	0	0	31.30	33.14	35.12	39.85	56.46	2280	456.24
100	5	0	35.52	37.37	39.05	43.12	57.11	1229	246.78
100	10	0	43.25	45.76	48.25	54.29	51.59	1358	272.47
100	15	0	42.23	44.09	45.74	49.78	24.50	2591	518.79
100	20	0	41.74	43.75	46.30	52.45	14.19	1589	318.00
100	25	0	45.13	47.26	48.83	52.75	12.59	320	64.21
100	30	0	49.30	51.25	52.72	56.45	13.15	56	11.36

Z [mm]	X [mm]	Y [mm]	D 10 [µm]	D 20 [µm]	D 30 [µm]	D 32 [µm]	Vax [m/s]	Count	Data Rate [#/s]
250	0	-60	52.20	52.41	52.41	53.04	1.51	11	1.23
250	0	-50	42.24	43.97	45.53	49.39	1.82	119	12.17
250	0	-40	42.43	44.39	46.04	50.09	4.37	483	48.62
250	0	-30	43.01	44.95	46.61	50.69	10.05	1556	155.96
250	0	-20	43.82	45.85	47.63	52.01	17.85	4106	410.88
250	0	-10	42.86	44.95	46.92	51.71	29.43	9440	944.07
250	0	0	38.64	40.64	42.54	47.14	37.47	22464	2246.61
250	0	10	38.28	40.30	42.20	46.80	34.77	26366	2636.68
250	0	20	36.00	38.35	40.65	46.18	25.06	24453	2445.45
250	0	30	32.43	35.02	37.41	43.17	15.71	14191	1419.52
250	0	40	28.19	31.02	33.63	39.94	7.91	4076	407.92
250	0	50	27.61	30.62	33.34	39.92	3.76	746	75.17
250	0	60	35.22	38.02	40.41	46.16	1.91	67	6.80
250	-60	0	30.70	33.91	36.71	43.50	1.68	299	30.32
250	-50	0	26.79	30.17	33.25	40.82	3.90	1982	198.32
250	-40	0	27.50	30.77	33.76	41.07	8.43	8881	888.17
250	-30	0	31.72	34.65	37.36	43.91	16.23	20589	2058.97
250	-20	0	35.59	38.10	40.50	46.27	27.26	32991	3299.35
250	-10	0	37.84	40.04	42.15	47.24	35.75	33996	3399.91
250	0	0	39.12	41.07	42.93	47.42	37.71	23712	2372.04
250	10	0	42.21	44.20	46.06	50.57	35.73	13172	1317.23
250	20	0	45.78	48.02	50.22	55.58	27.43	6039	604.45
250	30	0	43.74	45.80	47.85	52.87	17.21	3016	302.15
250	40	0	38.90	41.00	42.93	47.58	8.82	994	99.62
250	50	0	36.65	38.37	39.86	43.50	4.39	198	20.62
250	60	0	37.01	39.05	41.26	46.58	2.08	33	3.58
500	0	-90	48.48	51.02	53.38	59.12	1.98	378	18.92
500	0	-75	49.01	51.42	53.73	59.38	3.90	1095	54.78
500	0	-60	57.29	59.47	61.41	66.28	6.45	2446	122.60
500	0	-45	54.65	57.01	59.14	64.43	10.47	4647	232.48
500	0	-30	51.14	53.56	55.75	61.13	14.18	7632	381.67
500	0	-15	48.74	51.30	53.60	59.20	18.30	13718	685.98
500	0	0	50.91	53.34	55.53	60.91	22.22	24186	1209.33
500	0	15	46.73	49.39	51.85	57.80	21.95	28803	1440.26
500	0	30	45.08	47.82	50.38	56.58	19.51	23438	1171.93
500	0	45	43.01	45.96	48.63	55.07	15.72	17664	883.42
500	0	60	42.79	45.92	48.81	55.79	11.79	12398	620.12
500	0	75	43.55	46.54	49.31	56.01	8.02	6604	330.34
500	0	90	42.68	45.88	48.80	55.85	4.32	2025	101.54
500	-90	0	35.59	39.76	43.45	52.49	3.42	2993	150.05
500	-75	0	34.47	38.13	41.54	49.86	6.48	6762	338.28
500	-60	0	37.70	41.15	44.38	52.19	9.79	10330	516.71
500	-45	0	41.28	44.50	47.44	54.56	12.97	14891	744.63
500	-30	0	46.99	49.82	52.43	58.74	17.96	20390	1019.53
500	-15	0	49.88	52.46	54.83	60.62	21.01	23067	1153.37
500	0	0	47.88	50.47	52.82	58.55	21.66	23329	1166.48
500	15	0	51.03	53.48	55.76	61.33	20.61	18229	911.52
500	30	0	50.43	53.02	55.40	61.22	17.08	11693	584.68
500	45	0	47.97	50.76	53.50	60.16	12.53	6524	326.42
500	60	0	44.77	47.65	50.36	56.93	7.90	2758	138.12
500	75	0	42.58	45.50	48.56	55.96	4.29	943	47.26
500	90	0	41.12	43.58	45.68	50.78	1.94	172	8.66

Z [mm]	X [mm]	Y [mm]	D 10 [µm]	D 20 [µm]	D 30 [µm]	D 32 [µm]	Vax [m/s]	Count	Data Rate [#/s]
750	0	-120	63.10	66.40	69.37	76.68	1.80	175	8.79
750	0	-100	60.40	63.36	66.03	72.60	3.32	719	36.12
750	0	-80	60.38	63.38	66.10	72.80	6.71	2247	112.53
750	0	-60	53.64	56.75	59.58	66.47	8.03	3040	152.32
750	0	-40	54.22	57.43	60.34	67.42	10.55	4591	229.71
750	0	-20	54.33	57.65	60.69	68.09	13.34	7743	387.26
750	0	0	55.15	58.40	61.30	68.38	14.30	9613	480.89
750	0	20	54.50	57.81	60.78	68.02	14.87	11543	577.26
750	0	40	51.71	55.14	58.21	65.67	13.23	9866	493.48
750	0	60	48.60	52.25	55.61	63.74	10.43	7149	357.63
750	0	80	46.49	50.18	53.58	61.80	8.28	4896	244.81
750	0	100	45.58	49.62	53.25	62.05	5.66	2593	129.83
750	0	120	42.37	46.60	50.44	59.79	3.31	985	49.30
750	-120	0	44.66	48.83	52.75	62.29	3.75	1784	89.32
750	-100	0	47.71	51.86	55.74	65.16	5.14	3212	160.65
750	-80	0	48.90	52.94	56.69	65.79	6.92	4756	237.89
750	-60	0	49.23	53.16	56.80	65.64	9.97	8069	403.49
750	-40	0	51.92	55.59	58.87	66.83	12.57	10139	507.10
750	-20	0	52.55	56.06	59.23	66.93	14.30	11602	580.19
750	0	0	54.40	57.77	60.85	68.32	14.83	10622	531.34
750	20	0	57.22	60.38	63.18	70.04	12.40	6607	330.58
750	40	0	58.57	61.63	64.44	71.33	8.89	3086	154.40
750	60	0	59.41	62.56	65.45	72.55	6.52	1973	98.84
750	80	0	57.29	60.10	62.67	69.00	4.69	1015	51.02
750	100	0	53.55	56.35	58.84	64.94	3.11	469	23.65
750	120	0	55.62	58.68	61.44	68.19	1.72	145	7.84

130 bar

Z [mm]	X [mm]	Y [mm]	D 10 [µm]	D 20 [µm]	D 30 [µm]	D 32 [µm]	Vax [m/s]	Count	Data Rate [#/s]
50	0	-15	45.52	46.68	47.32	49.19	39.28	52	10.93
50	0	-12.5	44.02	44.90	45.56	47.44	44.21	207	41.75
50	0	-10	41.21	42.70	44.09	47.56	49.01	461	92.32
50	0	-7.5	37.74	40.38	42.66	48.16	61.98	430	86.15
50	0	-5	39.09	43.11	46.55	54.89	88.66	676	136.10
50	0	-2.5	37.71	41.91	48.81	66.95	94.70	314	63.18
50	0	0	33.21	36.15	38.59	44.46	95.53	103	20.75
50	0	2.5	31.87	36.09	43.46	63.74	92.23	360	72.78
50	0	5	35.05	38.23	41.66	50.04	85.70	2828	565.70
50	0	7.5	30.91	33.09	35.36	40.80	59.85	13311	2662.83
50	0	10	32.00	33.26	34.41	37.22	38.99	35005	7001.26
50	0	12.5	34.47	35.68	36.72	39.33	32.09	17185	3437.29
50	0	15	36.78	37.96	38.90	41.30	29.50	4293	858.96
50	-15	0	36.91	38.06	39.14	41.85	30.47	4563	913.03
50	-12.5	0	32.86	34.13	35.30	38.15	34.06	22522	4504.72
50	-10	0	29.92	31.29	32.58	35.70	41.53	44657	8931.68
50	-7.5	0	29.46	31.38	33.24	37.66	60.10	17314	3463.19
50	-5	0	33.61	36.64	40.29	49.27	85.73	3349	670.72
50	-2.5	0	34.08	37.44	42.72	56.26	95.78	598	120.22
50	0	0	28.15	30.72	33.09	38.82	94.40	130	26.21
50	2.5	0	32.75	36.95	41.26	52.05	97.09	77	16.02
50	5	0	38.75	42.56	46.23	55.15	97.94	159	32.26
50	7.5	0	38.58	44.35	49.14	61.02	85.93	293	58.74
50	10	0	39.26	41.97	44.34	50.05	52.44	408	83.17
50	12.5	0	43.55	44.64	45.45	47.65	44.27	483	97.06
50	15	0	43.88	44.93	45.51	47.22	39.40	148	30.22
100	0	-30	52.40	53.09	53.51	55.00	14.48	3	1.55
100	0	-25	43.16	44.63	45.89	49.06	12.07	45	10.77
100	0	-20	37.66	39.21	40.46	43.58	10.91	233	46.67
100	0	-15	35.09	36.81	38.81	43.64	14.77	841	168.50
100	0	-10	35.18	37.32	39.82	45.83	32.93	917	183.82
100	0	-5	36.87	39.70	43.62	53.25	57.90	860	173.04
100	0	0	30.49	32.59	34.89	40.43	62.90	884	177.01
100	0	5	31.11	33.18	35.06	39.55	57.84	2913	583.11
100	0	10	29.05	31.10	32.97	37.44	41.80	16001	3200.86
100	0	15	24.86	27.07	29.01	33.65	20.62	28745	5749.18
100	0	20	23.14	25.84	28.26	34.14	10.26	11207	2241.65
100	0	25	28.03	30.84	33.23	39.01	7.84	1583	317.26
100	0	30	36.20	38.02	39.42	42.86	7.89	148	30.22
100	-30	0	37.09	39.58	41.51	46.17	10.02	189	37.97
100	-25	0	27.15	30.08	32.50	38.35	8.35	2766	553.59
100	-20	0	21.72	24.36	26.73	32.49	11.10	21695	4339.27
100	-15	0	23.14	25.42	27.52	32.55	23.77	41376	8275.60
100	-10	0	28.00	30.22	32.39	37.60	47.07	16623	3324.84
100	-5	0	30.88	33.04	35.03	39.80	61.43	3210	642.47
100	0	0	30.55	32.53	34.53	39.34	62.43	840	168.48
100	5	0	34.61	37.57	40.71	48.34	63.73	308	62.44
100	10	0	39.10	42.16	45.04	51.97	56.31	320	64.82
100	15	0	35.52	37.12	38.43	41.66	24.18	1170	234.37
100	20	0	34.93	36.61	38.00	41.38	14.31	1056	211.64
100	25	0	36.24	38.15	39.79	43.79	11.60	322	64.88
100	30	0	36.41	40.09	42.64	48.78	11.16	20	4.31

Z [mm]	X [mm]	Y [mm]	D 10 [µm]	D 20 [µm]	D 30 [µm]	D 32 [µm]	Vax [m/s]	Count	Data Rate [#/s]
250	0	-60	43.66	44.35	44.83	46.33	0.68	24	3.39
250	0	-50	42.37	43.79	45.07	48.29	1.85	123	12.48
250	0	-40	39.16	40.90	42.53	46.52	3.50	1166	116.68
250	0	-30	37.18	38.97	40.57	44.48	8.73	3800	380.48
250	0	-20	37.63	39.50	41.16	45.21	17.39	7979	798.10
250	0	-10	38.07	40.09	42.08	46.89	29.67	14393	1439.56
250	0	0	36.45	38.34	40.05	44.20	40.38	24815	2481.96
250	0	10	35.02	36.96	38.72	42.97	38.30	35971	3597.15
250	0	20	31.95	34.06	35.95	40.49	27.70	42795	4279.67
250	0	30	27.55	29.92	32.11	37.39	16.22	35414	3542.01
250	0	40	25.41	27.87	30.14	35.61	8.94	17492	1749.45
250	0	50	25.46	28.16	30.56	36.34	4.37	3392	339.36
250	0	60	29.91	32.31	34.26	38.93	2.11	398	40.31
250	-60	0	29.75	32.56	34.89	40.48	2.25	383	38.79
250	-50	0	24.75	27.64	30.20	36.43	4.30	5257	526.35
250	-40	0	23.86	26.62	29.18	35.42	8.89	24735	2473.79
250	-30	0	26.94	29.46	31.76	37.30	17.29	45160	4516.37
250	-20	0	31.32	33.56	35.58	40.44	29.14	50027	5003.58
250	-10	0	34.94	37.01	39.03	43.89	38.22	37317	3731.99
250	0	0	36.60	38.49	40.21	44.38	40.77	22357	2235.78
250	10	0	38.61	40.55	42.33	46.65	38.31	14582	1458.56
250	20	0	39.01	40.97	42.71	46.94	29.42	11036	1103.74
250	30	0	35.64	37.57	39.30	43.48	16.81	8214	821.76
250	40	0	32.18	34.10	35.87	40.11	7.91	3725	372.85
250	50	0	33.29	35.07	36.64	40.44	4.03	759	75.95
250	60	0	37.89	39.89	41.58	45.69	2.38	83	8.91
500	0	-90	46.73	48.16	49.28	52.19	1.13	99	5.09
500	0	-75	47.32	49.64	51.65	56.60	3.25	491	24.58
500	0	-60	43.88	46.12	48.16	53.14	5.81	1697	84.90
500	0	-45	44.00	46.20	48.22	53.13	9.98	3636	181.96
500	0	-30	45.39	47.58	49.50	54.19	15.14	7031	351.61
500	0	-15	45.38	47.59	49.77	55.07	20.61	14405	720.49
500	0	0	45.17	47.39	49.42	54.38	24.65	29099	1455.03
500	0	15	44.25	46.50	48.59	53.66	24.71	34119	1705.99
500	0	30	43.49	45.67	47.63	52.41	22.04	25966	1298.42
500	0	45	40.87	43.33	45.58	51.02	16.25	17366	868.57
500	0	60	36.55	39.25	41.73	47.71	11.18	12062	603.20
500	0	75	33.92	36.84	39.47	45.81	7.99	7168	358.53
500	0	90	33.18	36.10	38.70	44.95	5.11	3052	152.91
500	-90	0	31.30	34.88	38.02	45.64	3.30	2130	106.61
500	-75	0	31.07	34.91	38.33	46.71	5.64	6009	300.54
500	-60	0	32.81	36.10	39.09	46.37	9.22	12041	602.32
500	-45	0	36.97	39.82	42.41	48.66	13.90	19136	956.90
500	-30	0	40.91	43.46	45.77	51.35	19.16	25888	1294.68
500	-15	0	43.57	45.92	48.03	53.16	23.15	31080	1554.04
500	0	0	44.87	47.13	49.19	54.22	24.38	26751	1337.76
500	15	0	46.22	48.37	50.31	55.06	22.55	18978	949.00
500	30	0	45.56	47.79	49.85	54.90	18.74	12168	608.47
500	45	0	41.84	44.12	46.13	51.02	12.00	5462	273.22
500	60	0	38.76	41.07	43.11	48.05	7.01	2402	120.31
500	75	0	38.76	40.78	42.63	47.12	3.76	831	41.65
500	90	0	37.82	40.09	42.04	46.76	2.27	224	11.31

Z [mm]	X [mm]	Y [mm]	D 10 [µm]	D 20 [µm]	D 30 [µm]	D 32 [µm]	Vax [m/s]	Count	Data Rate [#/s]
750	0	-120	52.33	54.69	56.79	61.98	1.86	181	9.07
750	0	-100	50.89	53.66	56.10	62.07	3.89	765	38.55
750	0	-80	50.26	52.91	55.27	61.04	5.43	1314	65.77
750	0	-60	50.27	52.98	55.47	61.53	6.99	2018	101.03
750	0	-40	52.88	55.65	58.14	64.24	8.28	2625	131.56
750	0	-20	52.27	54.79	57.03	62.54	12.23	4981	249.13
750	0	0	53.32	56.03	58.49	64.53	15.63	9182	459.17
750	0	20	54.09	56.71	59.03	64.76	16.21	10420	521.30
750	0	40	52.34	55.02	57.48	63.48	15.39	10102	505.31
750	0	60	48.74	51.61	54.17	60.41	13.04	8588	429.59
750	0	80	46.26	49.24	52.14	59.18	10.90	6518	326.23
750	0	100	42.88	46.22	49.29	56.70	7.32	3729	186.46
750	0	120	40.84	44.59	48.05	56.45	4.59	1716	85.81
750	-120	0	36.76	41.28	45.43	55.67	4.18	2121	106.09
750	-100	0	37.27	41.78	46.00	56.40	5.28	3632	181.83
750	-80	0	43.97	47.38	50.60	58.39	8.51	6941	347.12
750	-60	0	45.86	49.20	52.36	60.00	10.83	9018	450.98
750	-40	0	48.20	51.28	54.10	60.93	13.22	10740	537.05
750	-20	0	51.07	53.96	56.64	63.18	15.69	12877	643.92
750	0	0	52.95	55.70	58.14	64.11	16.71	12811	640.75
750	20	0	52.84	55.43	57.69	63.24	15.26	9487	474.42
750	40	0	51.53	54.12	56.44	62.11	10.98	4400	220.11
750	60	0	49.23	52.19	54.81	61.18	7.04	1863	93.32
750	80	0	49.14	51.68	54.01	59.69	5.52	1219	61.07
750	100	0	45.31	48.15	50.73	56.99	3.72	602	30.20
750	120	0	46.62	49.71	52.71	59.97	4.03	502	26.29

Appendix B: complete droplet size distributions

50 bar

			N_weighted				
Dclass [µm]	upper bound [µm]	lower bound [µm]	z50	z100	z250	z500	z750
1.07	1.00	1.14	3.26E+05	1.62E+05	6.01E+04	1.50E+04	2.34E+04
1.22	1.14	1.30	7.38E+04	4.97E+04	1.04E+04	5.17E+03	1.26E+04
1.39	1.30	1.49	4.55E+04	1.83E+04	7.52E+03	1.54E+03	1.10E+04
1.59	1.49	1.70	8.68E+04	3.23E+04	2.28E+04	2.36E+03	2.15E+04
1.81	1.70	1.94	1.41E+05	6.83E+04	4.00E+04	8.26E+03	1.07E+04
2.07	1.94	2.21	1.62E+05	9.99E+04	2.66E+04	8.62E+03	1.18E+04
2.37	2.21	2.53	1.67E+05	8.46E+04	3.74E+04	1.05E+04	3.33E+04
2.70	2.53	2.89	1.92E+05	1.09E+05	5.09E+04	1.91E+04	2.53E+04
3.08	2.89	3.29	3.01E+05	1.70E+05	7.01E+04	2.69E+04	3.74E+04
3.52	3.29	3.76	4.41E+05	2.49E+05	1.17E+05	3.77E+04	5.92E+04
4.02	3.76	4.29	5.12E+05	3.40E+05	1.05E+05	3.92E+04	7.05E+04
4.59	4.29	4.90	8.45E+05	5.90E+05	2.12E+05	9.57E+04	1.27E+05
5.24	4.90	5.60	9.38E+05	5.82E+05	2.59E+05	1.13E+05	2.02E+05
5.98	5.60	6.39	1.54E+06	1.08E+06	4.18E+05	2.35E+05	3.24E+05
6.83	6.39	7.29	2.17E+06	1.56E+06	6.75E+05	3.78E+05	5.02E+05
7.79	7.29	8.33	3.51E+06	2.59E+06	1.18E+06	7.56E+05	9.70E+05
8.90	8.33	9.50	5.03E+06	3.97E+06	1.76E+06	1.30E+06	1.50E+06
10.16	9.50	10.85	7.16E+06	5.70E+06	2.79E+06	2.20E+06	2.18E+06
11.59	10.85	12.39	9.86E+06	8.27E+06	4.39E+06	3.58E+06	3.33E+06
13.24	12.39	14.14	1.42E+07	1.21E+07	6.80E+06	5.92E+06	5.02E+06
15.11	14.14	16.15	1.84E+07	1.59E+07	9.67E+06	8.28E+06	6.32E+06
17.25	16.15	18.43	2.38E+07	2.05E+07	1.34E+07	1.02E+07	7.80E+06
19.69	18.43	21.04	2.82E+07	2.47E+07	1.68E+07	1.18E+07	8.83E+06
22.48	21.04	24.02	3.27E+07	2.77E+07	2.00E+07	1.23E+07	9.32E+06
25.67	24.02	27.42	3.61E+07	2.88E+07	2.17E+07	1.22E+07	9.01E+06
29.30	27.42	31.31	3.78E+07	2.90E+07	2.17E+07	1.20E+07	8.49E+06
33.45	31.31	35.74	3.68E+07	2.70E+07	2.03E+07	1.11E+07	7.92E+06
38.19	35.74	40.81	3.41E+07	2.60E+07	1.86E+07	1.06E+07	7.39E+06
43.60	40.81	46.59	2.88E+07	2.34E+07	1.63E+07	9.63E+06	6.84E+06
49.77	46.59	53.18	2.39E+07	2.03E+07	1.45E+07	9.02E+06	6.52E+06
56.82	53.18	60.72	1.77E+07	1.59E+07	1.26E+07	8.38E+06	6.19E+06
64.87	60.72	69.31	1.17E+07	1.14E+07	1.07E+07	7.39E+06	5.84E+06
74.06	69.31	79.13	6.88E+06	7.56E+06	8.80E+06	6.59E+06	5.25E+06
84.55	79.13	90.34	3.57E+06	4.54E+06	6.44E+06	5.52E+06	4.69E+06
96.52	90.34	103.13	1.67E+06	2.48E+06	3.53E+06	4.20E+06	4.00E+06
110.20	103.13	117.74	7.20E+05	1.17E+06	1.57E+06	2.79E+06	2.92E+06
125.80	117.74	134.42	3.26E+05	4.57E+05	5.92E+05	1.44E+06	1.89E+06
143.62	134.42	153.45	1.26E+05	1.68E+05	1.76E+05	5.64E+05	8.96E+05
163.96	153.45	175.19	6.25E+04	5.76E+04	5.32E+04	1.63E+05	3.26E+05
187.18	175.19	200.00	2.30E+04	3.20E+04	1.58E+04	3.98E+04	9.02E+04

80 bar

			N_weighted				
Dclass [µm]	**upper bound [µm]**	**lower bound [µm]**	**z50**	**z100**	**z250**	**z500**	**z750**
1.07	1.00	1.14	7.42E+05	3.10E+05	3.94E+04	1.42E+04	1.11E+03
1.22	1.14	1.30	1.77E+05	7.71E+04	9.40E+03	1.19E+03	0.00E+00
1.39	1.30	1.49	7.61E+04	3.48E+04	2.09E+03	0.00E+00	0.00E+00
1.59	1.49	1.70	1.60E+05	6.89E+04	1.78E+04	0.00E+00	0.00E+00
1.81	1.70	1.94	2.29E+05	1.32E+05	2.27E+04	0.00E+00	0.00E+00
2.07	1.94	2.21	3.31E+05	1.63E+05	1.38E+04	1.79E+03	0.00E+00
2.37	2.21	2.53	3.32E+05	1.54E+05	1.49E+04	1.19E+03	0.00E+00
2.70	2.53	2.89	4.07E+05	2.09E+05	1.93E+04	1.94E+03	0.00E+00
3.08	2.89	3.29	5.67E+05	2.84E+05	3.37E+04	2.38E+03	6.66E+03
3.52	3.29	3.76	8.29E+05	4.96E+05	5.87E+04	1.94E+03	0.00E+00
4.02	3.76	4.29	9.42E+05	5.20E+05	5.56E+04	4.77E+03	1.11E+03
4.59	4.29	4.90	1.75E+06	9.71E+05	9.24E+04	6.71E+03	3.33E+03
5.24	4.90	5.60	1.64E+06	9.88E+05	1.21E+05	1.49E+02	1.11E+04
5.98	5.60	6.39	2.69E+06	1.65E+06	2.18E+05	4.32E+03	1.78E+04
6.83	6.39	7.29	3.77E+06	2.66E+06	3.71E+05	1.91E+04	3.22E+04
7.79	7.29	8.33	5.75E+06	4.10E+06	7.47E+05	9.98E+03	1.78E+04
8.90	8.33	9.50	8.14E+06	6.16E+06	1.19E+06	2.65E+04	5.02E+04
10.16	9.50	10.85	1.09E+07	8.84E+06	1.90E+06	9.73E+04	1.26E+05
11.59	10.85	12.39	1.50E+07	1.27E+07	3.47E+06	2.04E+05	3.05E+05
13.24	12.39	14.14	2.08E+07	1.88E+07	5.80E+06	4.55E+05	8.07E+05
15.11	14.14	16.15	2.65E+07	2.41E+07	8.91E+06	1.05E+06	1.41E+06
17.25	16.15	18.43	3.50E+07	3.12E+07	1.35E+07	2.24E+06	2.60E+06
19.69	18.43	21.04	4.50E+07	3.79E+07	1.93E+07	4.13E+06	4.75E+06
22.48	21.04	24.02	5.70E+07	4.54E+07	2.62E+07	7.20E+06	7.06E+06
25.67	24.02	27.42	6.76E+07	5.12E+07	3.17E+07	1.11E+07	9.47E+06
29.30	27.42	31.31	7.42E+07	5.64E+07	3.77E+07	1.47E+07	1.21E+07
33.45	31.31	35.74	7.44E+07	5.91E+07	4.15E+07	1.78E+07	1.37E+07
38.19	35.74	40.81	7.01E+07	6.03E+07	4.27E+07	2.05E+07	1.51E+07
43.60	40.81	46.59	5.72E+07	5.42E+07	3.97E+07	2.15E+07	1.56E+07
49.77	46.59	53.18	4.10E+07	4.26E+07	3.59E+07	2.19E+07	1.61E+07
56.82	53.18	60.72	2.29E+07	2.71E+07	2.84E+07	2.11E+07	1.57E+07
64.87	60.72	69.31	1.11E+07	1.45E+07	1.91E+07	1.80E+07	1.41E+07
74.06	69.31	79.13	4.93E+06	6.61E+06	1.06E+07	1.36E+07	1.19E+07
84.55	79.13	90.34	2.06E+06	2.37E+06	4.31E+06	8.52E+06	8.86E+06
96.52	90.34	103.13	7.93E+05	7.96E+05	1.44E+06	4.20E+06	5.57E+06
110.20	103.13	117.74	3.59E+05	2.61E+05	4.01E+05	1.50E+06	2.66E+06
125.80	117.74	134.42	1.36E+05	1.07E+05	1.20E+05	3.75E+05	8.83E+05
143.62	134.42	153.45	7.32E+04	3.10E+04	4.04E+04	7.69E+04	2.07E+05
163.96	153.45	175.19	4.95E+04	2.02E+04	1.33E+04	2.31E+04	3.50E+04
187.18	175.19	200.00	1.36E+04	1.01E+04	3.69E+03	6.13E+03	1.12E+04

100 bar

			N_weighted				
Dclass [µm]	**upper bound [µm]**	**lower bound [µm]**	**z50**	**z100**	**z250**	**z500**	**z750**
1.07	1.00	1.14	6.13E+05	2.87E+05	8.08E+04	1.75E+04	1.14E+03
1.22	1.14	1.30	1.40E+05	9.30E+04	3.83E+03	3.08E+03	0.00E+00
1.39	1.30	1.49	9.64E+04	4.18E+04	1.72E+04	1.54E+03	0.00E+00
1.59	1.49	1.70	1.22E+05	1.05E+05	2.82E+04	3.08E+03	0.00E+00
1.81	1.70	1.94	2.07E+05	1.08E+05	2.10E+04	9.62E+02	1.14E+03
2.07	1.94	2.21	1.85E+05	2.35E+05	4.26E+04	2.31E+03	0.00E+00
2.37	2.21	2.53	1.85E+05	1.28E+05	3.83E+04	3.08E+03	0.00E+00
2.70	2.53	2.89	2.81E+05	1.89E+05	3.06E+04	8.66E+03	3.41E+03
3.08	2.89	3.29	3.87E+05	2.41E+05	5.93E+04	8.08E+03	0.00E+00
3.52	3.29	3.76	6.29E+05	4.22E+05	8.52E+04	2.31E+03	0.00E+00
4.02	3.76	4.29	7.20E+05	5.47E+05	1.59E+05	1.40E+04	5.68E+03
4.59	4.29	4.90	1.25E+06	9.12E+05	3.12E+05	3.85E+04	3.69E+03
5.24	4.90	5.60	1.30E+06	9.83E+05	3.55E+05	4.29E+04	0.00E+00
5.98	5.60	6.39	2.23E+06	1.70E+06	7.04E+05	6.31E+04	3.41E+03
6.83	6.39	7.29	3.07E+06	2.30E+06	1.06E+06	9.91E+04	9.08E+03
7.79	7.29	8.33	4.85E+06	4.31E+06	1.70E+06	1.89E+05	2.16E+04
8.90	8.33	9.50	7.16E+06	6.75E+06	2.67E+06	3.48E+05	2.38E+04
10.16	9.50	10.85	9.89E+06	1.07E+07	3.81E+06	6.32E+05	6.55E+04
11.59	10.85	12.39	1.47E+07	1.70E+07	6.46E+06	9.09E+05	8.34E+04
13.24	12.39	14.14	2.16E+07	2.72E+07	1.03E+07	1.85E+06	2.70E+05
15.11	14.14	16.15	2.96E+07	3.74E+07	1.51E+07	2.75E+06	7.19E+05
17.25	16.15	18.43	4.03E+07	5.21E+07	2.21E+07	4.40E+06	1.40E+06
19.69	18.43	21.04	5.47E+07	6.52E+07	3.00E+07	7.35E+06	2.81E+06
22.48	21.04	24.02	7.08E+07	7.77E+07	4.05E+07	1.13E+07	5.38E+06
25.67	24.02	27.42	8.83E+07	8.56E+07	5.24E+07	1.65E+07	8.64E+06
29.30	27.42	31.31	1.02E+08	9.39E+07	6.19E+07	2.28E+07	1.18E+07
33.45	31.31	35.74	1.03E+08	9.67E+07	6.91E+07	2.88E+07	1.52E+07
38.19	35.74	40.81	9.95E+07	9.53E+07	7.10E+07	3.44E+07	1.89E+07
43.60	40.81	46.59	7.82E+07	7.76E+07	6.47E+07	3.73E+07	2.12E+07
49.77	46.59	53.18	5.30E+07	5.20E+07	5.11E+07	3.69E+07	2.34E+07
56.82	53.18	60.72	2.49E+07	2.66E+07	3.44E+07	3.26E+07	2.31E+07
64.87	60.72	69.31	8.09E+06	9.41E+06	1.76E+07	2.42E+07	2.03E+07
74.06	69.31	79.13	2.44E+06	2.87E+06	6.37E+06	1.47E+07	1.57E+07
84.55	79.13	90.34	8.38E+05	9.49E+05	1.79E+06	6.62E+06	1.02E+07
96.52	90.34	103.13	3.57E+05	3.07E+05	4.54E+05	2.12E+06	5.13E+06
110.20	103.13	117.74	1.64E+05	1.37E+05	1.68E+05	5.01E+05	1.79E+06
125.80	117.74	134.42	8.13E+04	3.63E+04	6.22E+04	1.02E+05	4.31E+05
143.62	134.42	153.45	3.15E+04	1.54E+04	2.15E+04	2.59E+04	7.52E+04
163.96	153.45	175.19	7.89E+03	5.81E+03	1.45E+04	1.38E+04	5.15E+03
187.18	175.19	200.00	5.90E+03	1.55E+02	8.15E+03	6.87E+03	3.89E+03

130 bar

			N_weighted				
Dclass [µm]	**upper bound [µm]**	**lower bound [µm]**	**z50**	**z100**	**z250**	**z500**	**z750**
1.07	1.00	1.14	4.89E+05	1.72E+06	3.33E+05	1.94E+04	0.00E+00
1.22	1.14	1.30	8.74E+04	5.65E+05	1.04E+05	1.03E+04	0.00E+00
1.39	1.30	1.49	2.58E+04	2.18E+05	5.19E+04	3.42E+03	0.00E+00
1.59	1.49	1.70	1.02E+05	5.56E+05	9.32E+04	0.00E+00	8.81E+03
1.81	1.70	1.94	1.47E+05	7.27E+05	1.61E+05	6.85E+03	7.34E+03
2.07	1.94	2.21	1.71E+05	8.02E+05	2.07E+05	0.00E+00	0.00E+00
2.37	2.21	2.53	1.93E+05	1.06E+06	1.44E+05	1.06E+04	0.00E+00
2.70	2.53	2.89	1.29E+05	1.15E+06	2.49E+05	3.08E+04	0.00E+00
3.08	2.89	3.29	2.12E+05	1.65E+06	3.61E+05	5.71E+04	0.00E+00
3.52	3.29	3.76	3.55E+05	2.30E+06	5.31E+05	6.08E+04	4.41E+03
4.02	3.76	4.29	3.14E+05	3.06E+06	6.94E+05	4.37E+04	0.00E+00
4.59	4.29	4.90	5.52E+05	4.92E+06	1.31E+06	1.24E+05	4.41E+04
5.24	4.90	5.60	5.24E+05	5.66E+06	1.39E+06	1.60E+05	3.08E+04
5.98	5.60	6.39	8.17E+05	1.02E+07	2.45E+06	3.65E+05	5.29E+04
6.83	6.39	7.29	1.16E+06	1.49E+07	3.75E+06	5.05E+05	6.46E+04
7.79	7.29	8.33	1.72E+06	2.34E+07	6.45E+06	8.43E+05	1.71E+05
8.90	8.33	9.50	2.28E+06	3.31E+07	1.00E+07	1.25E+06	2.50E+05
10.16	9.50	10.85	3.33E+06	4.73E+07	1.51E+07	2.06E+06	3.76E+05
11.59	10.85	12.39	4.92E+06	6.42E+07	2.22E+07	3.07E+06	6.28E+05
13.24	12.39	14.14	8.59E+06	9.21E+07	3.37E+07	5.35E+06	1.21E+06
15.11	14.14	16.15	1.50E+07	1.11E+08	4.64E+07	7.87E+06	2.17E+06
17.25	16.15	18.43	2.57E+07	1.30E+08	6.21E+07	1.20E+07	3.63E+06
19.69	18.43	21.04	4.70E+07	1.47E+08	7.67E+07	1.71E+07	5.99E+06
22.48	21.04	24.02	7.65E+07	1.59E+08	9.57E+07	2.49E+07	9.37E+06
25.67	24.02	27.42	1.18E+08	1.68E+08	1.09E+08	3.34E+07	1.42E+07
29.30	27.42	31.31	1.58E+08	1.68E+08	1.17E+08	4.39E+07	1.98E+07
33.45	31.31	35.74	1.76E+08	1.56E+08	1.18E+08	5.35E+07	2.58E+07
38.19	35.74	40.81	1.63E+08	1.35E+08	1.09E+08	6.12E+07	3.20E+07
43.60	40.81	46.59	1.02E+08	8.64E+07	8.58E+07	6.11E+07	3.45E+07
49.77	46.59	53.18	4.46E+07	4.14E+07	5.84E+07	5.59E+07	3.65E+07
56.82	53.18	60.72	1.28E+07	1.52E+07	3.01E+07	4.27E+07	3.39E+07
64.87	60.72	69.31	4.08E+06	4.03E+06	1.14E+07	2.54E+07	2.71E+07
74.06	69.31	79.13	1.51E+06	1.26E+06	2.82E+06	1.17E+07	1.82E+07
84.55	79.13	90.34	6.88E+05	5.22E+05	5.72E+05	3.64E+06	9.48E+06
96.52	90.34	103.13	3.42E+05	2.04E+05	1.82E+05	7.54E+05	3.31E+06
110.20	103.13	117.74	1.48E+05	1.40E+05	1.01E+05	1.46E+05	9.68E+05
125.80	117.74	134.42	7.06E+04	6.77E+04	3.98E+04	5.06E+04	1.51E+05
143.62	134.42	153.45	4.46E+04	2.29E+04	1.42E+04	2.55E+04	8.42E+03
163.96	153.45	175.19	2.15E+04	5.00E+02	6.65E+03	1.36E+04	7.77E+03
187.18	175.19	200.00	8.25E+03	1.54E+04	6.39E+03	1.27E+04	8.69E+03